

PREFERENTIAL SPUTTERING

EFFECTS IN  $\text{Nb}_2\text{O}_5$

PREFERENTIAL SPUTTERING EFFECTS

IN  $\text{Nb}_2\text{O}_5$

By

DASARAO KRISHNA MURTI, M.Sc.

A Thesis

Submitted to the School of Graduate Studies

in Partial Fulfilment of the Requirements

for the Degree

Doctor of Philosophy

DOCTOR OF PHILOSOPHY (1975)  
(Materials Science)

McMASTER UNIVERSITY  
Hamilton, Ontario

TITLE: Preferential Sputtering Effects in  $\text{Nb}_2\text{O}_5$

AUTHOR: Dasarao Krishna Murti, M.Sc. (University of Waterloo)

SUPERVISOR: Professor R. Kelly

NUMBER OF PAGES: xiii, 157

## ABSTRACT

Ion bombardment has been used as a technique for the sputtering of metals for several years; very few studies have, however, been made on alloys and compounds, especially studies where the target itself was analyzed after ion bombardment. In this thesis results are presented concerning the changes in targets of  $\text{Nb}_2\text{O}_5$  and related systems due to ion bombardment. The targets used were in the form of anodic thin films and sintered pellets. Bombardments were carried out using  $\text{Kr}^+$  and  $\text{O}_2^+$  ions with energies of 2 to 35 keV and at doses varying from  $10^{13}$  to  $10^{17}$  ions/cm<sup>2</sup>. The structural changes induced by the bombardment were studied with an electron microscope and the changes in electrical conductivity were studied with a four point probe.

The results indicate that an altered layer is formed which has the stoichiometry of  $\text{NbO}$  when  $\text{Nb}_2\text{O}_5$  targets are bombarded with 35 keV ions at high doses ( $\geq 1 \times 10^{17}$  ions/cm<sup>2</sup>). A technique based on the changes in the chemical reactivity of the altered layer as compared to the substrate is used to estimate the thickness of the altered layer. That on  $\text{Nb}_2\text{O}_5$  varies from 18 nm at very low doses ( $5 \times 10^{13}$  ions/cm<sup>2</sup>) to 23 nm at high doses ( $1 \times 10^{17}$  ions/cm<sup>2</sup>). The conductivity of the altered layer formed at high doses is about  $4 \times 10^3$  S/m, an increase by a factor of  $2 \times 10^8$ . An energy threshold for conductivity changes was found using an oxygen ion beam, whereas Kr ion bombardment reveals conductivity changes at all

Oxygen loss from bombarded  $\text{Nb}_2\text{O}_5$  can be considered to have three alternative origins based on a vaporization model, an internal displacement model and a preferential sputtering model. The results favour the preferential sputtering of oxygen as the likely mechanism to explain the altered layer in the target. A modified sputtering model explains the energy threshold effect observed when an oxygen beam is used.

Several applications of the techniques and results presented here have been considered. They include, among others, dating of minerals, limitations of surface analytical techniques, and preliminary results for  $\text{Ta}_2\text{O}_5$ .

## ACKNOWLEDGEMENTS

I am indebted to Dr. R. Kelly for his continuous guidance, encouragement and friendship throughout the course of this work. I wish to express my sincere gratitude to the members of my supervisory committee, Drs. J. D. Embury, C.J.L. Lock and Professor C. M. Sargent for their interest and encouragement.

Thanks are due to Dr. P. Sigmund (University of Copenhagen) for supplying Fig. 2-3 and Dr. K. B. Winterbon (AECL, Chalk River) for supplying the data on range parameters in  $\text{Nb}_2\text{O}_5$  (Table II-1). The technical assistance of F. Smith and D. Hodgson is greatly appreciated. I wish to thank Mrs. H. Kennelly for her skill and patience in typing this thesis.

This work was supported by grants from the Defence Research Board of Canada, the National Research Council of Canada and the Geological Survey of Canada to Dr. R. Kelly. I thank the National Research Council of Canada for the award of a P.I.E.R. fellowship and McMaster University for the award of a teaching assistantship.

Finally, I am deeply grateful to my wife, Brinda, for her patience and constant support throughout the course of this work.

## TABLE OF CONTENTS

	<u>Page</u>
CHAPTER 1      INTRODUCTION	1
1.1      PARTICLE SOLID INTERACTIONS	1
1.2      APPLICATIONS OF SPUTTERING	4
1.3      MODIFICATIONS OF THE SPUTTERED SURFACE	8
1.4      WHY STUDY Nb <sub>2</sub> O <sub>5</sub> ?	12
CHAPTER 2      A REVIEW OF ION IMPACT THEORY	15
2.1      INTRODUCTION	15
2.2      ENERGY LOSS MECHANISMS	18
2.3      LSS THEORY	20
2.4      APPLICATION OF LSS THEORY	24
2.5      WSS THEORY	26
2.6      RANGE AND DAMAGE PROFILES	29
2.7      THEORY OF ROL, FLUIT AND KISTEMAKER	30
2.8      SIGMUND'S THEORY OF SPUTTERING	31
2.9      ENERGY DISSIPATION IN COMPOUND TARGETS	36
CHAPTER 3      EXPERIMENTAL TECHNIQUES	41
3.1      SAMPLE PREPARATION	41
3.1.1 Anodic Thin Films of Nb <sub>2</sub> O <sub>5</sub>	41
3.1.2 Sintered Pellets	42
3.2      ION BOMBARDMENT	43
3.3      ELECTRICAL CONDUCTIVITY MEASUREMENTS	46
3.3.1 Terminology	46
3.3.2 Measurement Techniques	47

	<u>Page</u>
3.4 ELECTRON MICROSCOPY	57
3.4.1 Introduction	57
3.4.2 Transmission Mode	58
3.4.3 Reflection Mode	61
3.4.4 Analysis of Electron Diffraction Patterns	63
CHAPTER 4 EXPERIMENTAL RESULTS: STRUCTURAL CHANGES	67
4.1 INTRODUCTION	67
4.2 STRUCTURE OF AMORPHOUS MATERIALS	68
4.3 THIN FILMS OF $\text{Nb}_2\text{O}_5$	70
4.3.1 Structure of as Prepared Films	70
4.3.2 Effect of Ion Dose	73
4.4 SINTERED $\text{Nb}_2\text{O}_5$ PELLETS	77
4.5 SUMMARY	78
CHAPTER 5 EXPERIMENTAL RESULTS: CONDUCTIVITY CHANGES	82
5.1 EFFECT OF ION DOSE	82
5.2 EFFECT OF ION ENERGY	84
5.3 ANNEALING OF CONDUCTIVITY	86
5.4 EFFECT OF ION CURRENT	88
5.5 SUMMARY AND CONCLUSIONS	91
CHAPTER 6 EXPERIMENTAL RESULTS: THICKNESS OF ALTERED LAYER	93
6.1 INTRODUCTION	93
6.2 THICKNESS OF ALTERED LAYER AT LOW TO MEDIUM DOSES	93
6.3 THICKNESS OF ALTERED LAYER AT HIGH DOSES	100



	<u>Page</u>
6.4 IMPLICATIONS OF THICKNESS OF NBO LAYER	102
6.5 SUMMARY AND CONCLUSIONS	103
CHAPTER 7 DISCUSSION OF EXPERIMENTAL RESULTS	104
7.1 INTRODUCTION	104
7.2 MECHANISMS FOR OXYGEN LOSS	105
7.2.1 Vaporization Model	105
7.2.2 Internal Displacement Model	105
7.2.3 Preferential Sputtering Model	107
7.3 SPUTTERING MODEL APPLIED TO AN OXYGEN BEAM	110
7.4 PREFERENTIAL SPUTTERING COMBINED WITH DIFFUSION	117
7.4.1 Diffusion Model	117
7.4.2 Thickness of Altered Layer	122
7.5 SUMMARY	122
CHAPTER 8 APPLICATIONS	124
8.1 CHANGES IN AND CONTROL OF CONDUCTIVITY	124
8.2 PREPARATION OF LOWER VALENCE OXIDES	124
8.3 REDUCTION OF OXIDES - MICROWAVE DISCHARGE	125
8.4 MINERALS ON THE MOON AND IN THE EARTH'S INTERIOR	126
8.5 DATING OF MINERALS	127
8.6 PREFERENTIAL SPUTTERING EFFECTS IN SURFACE ANALYSIS	131
8.7 PREFERENTIAL SPUTTERING OF CERMET FILMS	135

	<u>Page</u>
8.8 ION BOMBARDMENT EFFECTS WITH Ta <sub>2</sub> O <sub>5</sub>	135
8.8.1 Introduction	
8.8.2 Experimental Results - Conductivity Changes	136
8.8.3 Experimental Results - Structural Changes	136
8.8.4 Conclusions	138
CHAPTER 9 SUMMARY	141
APPENDIX I RANGE PARAMETERS FOR 35 keV <sup>85</sup> Kr IONS INCIDENT ON NbO <sub>2</sub>	144
APPENDIX II RANGE PARAMETERS FOR keV O <sub>2</sub> <sup>+</sup> IONS INCIDENT ON Nb <sub>2</sub> O <sub>5</sub>	148
REFERENCES	149

# LIST OF ILLUSTRATIONS

FIGURE NO.	TITLE	PAGE
1-1	The simple focusing process	5
1-2	A focused collision sequence	5
1-3	Spatial distribution of the sputtering process	10
1-4	Distribution of sputtering yield	10
2-1(a)	Definition of ion range	16
(b)	Ion range distribution	16
2-2	Theoretical nuclear and electronic stopping power curves	23
2-3	Displacement efficiencies for the system Nb-O	39
3-1	Radio frequency ion accelerator	44
3-2	Rectangularly shaped section of thin film for conductivity measurement	48
3-3	Schematic of conductivity measurement technique	49
3-4	Schematic of four point probe	51
3-5	Images for the case of the four point probes on a thin slice with a non conducting substrate	55
3-6	Ray diagram showing the bright field mode of operation	59
3-7	Ray diagram showing the diffraction mode of operation	60
4-1	Transmission electron microscopy of as prepared anodic Nb <sub>2</sub> O <sub>5</sub> films	72
4-2	Transmission electron microscopy of Nb <sub>2</sub> O <sub>5</sub> films bombarded to a dose of $5 \times 10^{15}$ ions/cm <sup>2</sup>	74

FIGURE NO.	TITLE	PAGE
4-3	Transmission electron microscopy of $\text{Nb}_2\text{O}_5$ films bombarded to a dose of $5 \times 10^{16}$ ions/cm <sup>2</sup>	75
4-4	Reflection electron diffraction patterns of sintered $\text{Nb}_2\text{O}_5$ pellets before and after bombardment	79
5-1	Effect of ion dose on the sheet conductivity of $\text{Nb}_2\text{O}_5$ pellets	83
5-2	Effect of ion energy on the sheet conductivity of $\text{Nb}_2\text{O}_5$ pellets	85
5-3	Effect of annealings on the sheet conductivity of bombarded $\text{Nb}_2\text{O}_5$ pellets	87
5-4	Effect of ion current on the sheet conductivity of $\text{Nb}_2\text{O}_5$ pellets	90
6-1	Activity versus time of exposure to fluoboric acid saturated with ammonium chloride for $\text{Nb}_2\text{O}_5$ pellets bombarded with 35 keV $^{85}\text{Kr}$ to various doses	95
6-2	Activity versus time of exposure to a solution consisting of $\text{HF}$ , $\text{NH}_4\text{Cl}$ and $\text{H}_2\text{O}$ for $\text{Nb}_2\text{O}_5$ pellets bombarded with 35 keV $^{85}\text{Kr}$ to various doses	96
6-3	Integral concentration profiles for 35 keV $^{85}\text{Kr}$ ions incident on a) $\text{Nb}_2\text{O}_5$ and b) $\text{NbO}$	98
6-4	Dissolution of altered layers formed on $\text{Nb}_2\text{O}_5$ pellets bombarded with 35 keV $\text{Kr}^+$ and $\text{O}_2^+$ ions	101
7-1	Dissolution curve for 5 keV $\text{O}_2^+$ ion bombarded with $\text{Nb}_2\text{O}_5$ pellets	113
7-2	Integral concentration profile for 10 keV $^{85}\text{Kr}$ ions incident on $\text{Nb}_2\text{O}_5$	114
7-3	Effect of ion energy on sputtering yield	116

FIGURE NO.	TITLE	PAGE
8-1	Reflection electron diffraction patterns for columbite - before and after bombardment	129
8-2	Dissolution curves for columbite bombarded with 35 keV $^{85}\text{Kr}$ ions to various doses	130
8-3	X-ray photoelectron spectra of $\text{MoO}_3$ exposed to $\text{Ar}^+$ and $\text{O}_2^+$ ions	132
8-4	Dependence of the photon yield from Al on the oxygen pressure	134
8-5	Effect of ion dose on the sheet conductivity of bombarded $\text{Ta}_2\text{O}_5$ pellets	137
8-6	Transmission electron microscopy of anodic $\text{Ta}_2\text{O}_5$ films, before and after bombardment	139

# LIST OF TABLES

TABLE NO.		PAGE
1-1	Examples of bombardment induced stoichiometry changes	13
2-1	Displacement efficiencies for the system Nb-O	40
3-1	Conductivity measurements - correction factor for finite thickness	53
3-2	Conductivity measurement - correction for finite thickness	56
3-3	Depth of penetration of electrons. Reflection electron diffraction	64
4-1	Diffraction analysis of Nb <sub>2</sub> O <sub>5</sub> films following bombardment with $5 \times 10^{16}$ ions/cm <sup>2</sup>	76
4-2	Diffraction analysis of Nb <sub>2</sub> O <sub>5</sub> pellets following bombardment with $2 \times 10^{17}$ ions/cm <sup>2</sup>	80
6-1	Altered layer thicknesses for 35 keV Kr bombardment of Nb <sub>2</sub> O <sub>5</sub> pellets	97
6-2	Comparison of $R_a/\langle x \rangle$ for various materials	99
7-1	Heats of atomization appropriate to the system Nb-O	108
7-2	Oxygen ion bombardment of Nb <sub>2</sub> O <sub>5</sub> - critical bombardment energies to cause reduction	115
II-1	Range parameters for O <sub>2</sub> <sup>+</sup> ions incident on Nb <sub>2</sub> O <sub>5</sub>	148

## CHAPTER 1

### INTRODUCTION

#### 1.1 PARTICLE SOLID INTERACTIONS

When a solid is bombarded with heavy ions, many phenomena can arise depending largely on the kinetic energy of the incident ions. At very low kinetic energies ( $\sim 5$  eV) the interaction is essentially confined to the outermost atomic layer of the target material. The incident ion may be reflected or may come into thermal equilibrium with the surface and subsequently be adsorbed or evaporated. The potential energy of the bombarding species plays an important role at these energies since it is responsible for electronic transitions which can give rise to the ejection of secondary electrons. In the case of compound materials, low energy ion bombardment can lead to the breaking or rearranging of chemical bonds. This leads to desorption, chemical reactions, and polymerization, with similar effects being induced also by bombarding with electrons or photons.

If the incident ions have a higher energy, they enter a target and gradually lose their energy through a series of collisions with the target atoms. Whenever the energy transferred to the target atoms exceeds a threshold energy of roughly  $4 \Delta H_s$  (where  $\Delta H_s$  is the heat of sublimation of the target material), the atoms involved in the collision are removed a sufficient distance from their original sites that they remain

displaced. The target atoms that recoil with a high enough energy propagate their collisions to other target atoms producing secondary displacements. Some of these recoil atoms have the possibility of getting scattered back towards the surface with sufficient energy to collide with and eject neutral target atoms from the surface over a wide range of angles and energies. This process of atomic ejection during bombardment is called "sputtering" and a sputtering yield "s" can be defined as the number of atoms sputtered per incident ion. Sputtering is a multiple collision process involving a cascade of target atoms. Ions rather than neutral atoms are used for bombardment because one can accelerate these to any desired energy with electric fields. If neutral atoms were desired, they could be formed from ions by charge exchange neutralization.

When a solid surface is bombarded with primary ions in the keV range several emission processes other than sputtering also take place. These include scattered incident ions, secondary ions, secondary electrons, and photon emission. In recent years secondary ion emission has been employed for the investigation of the chemical composition of bulk materials and thin films (1,2). This has been carried out by studying the mass, charge, composition, energy and angular distribution of the secondary ions as a function of the energy of the incident ions. Secondary electrons emitted when solid surfaces are bombarded with ions or electrons have been studied from the points of view of energy and angular distribution as well as yield. (Secondary electron yields are defined as the number of electrons emitted per incident particle.) Secondary



in the operation of the scanning electron microscope, and in a wide variety of currently popular techniques of surface analysis.

Studies have been made of photon emission (3,4) from surfaces during ion bombardment. They involve monitoring the spectral lines emitted from targets with a monochromator and photomultiplier as a detector. Kerkdijk and Thomas (5) consider three types of processes as contributing to photon emission. The incident particle may be excited as it is scattered by the surface, with photon emission occurring roughly  $10^{-8}$  s later when the particle is well away from the surface. Secondly, the spectral lines can be characteristic of the sputtered target atoms. Thirdly, the photon emission can be due to excitation which occurs within the surface itself. The spectral line intensities characteristic of the sputtered target material can be related to the sputtering yields. By measuring the line intensity as a function of the incident ion energy, especially at very low ion energies, one can determine the sputtering thresholds.

Another photon emission process due to ion bombardment is the generation of X-rays (6). When ions collide with target atoms it is believed that if there is sufficient interpenetration of the electronic shells, not only are short lived molecules formed but the atoms after separating may retain excitation. The result is X-ray emission. By careful selection of ion energy and type, various characteristic X-rays of the target atom, the incident ion or a combined molecular atom can be selectively excited and

## 1.2 APPLICATIONS OF SPUTTERING

Interest in sputtering has been nourished over the years from many different areas.

Sputtering experiments done on a monocrystalline sample lead to spot patterns on a suitably placed screen where the atoms are collected due to preferential ejection from close packed directions. This phenomenon has been attributed to focused collision sequences which propagate along close packed atomic rows (7). In this context focusing means that the atoms are sufficiently close to focus the momentum by successive collisions into the close packed directions.

Consider the collision illustrated in figure 1-1 where two atoms are represented by elastic hard spheres of radius  $R$  separated initially by a distance  $D_{hk\ell}$ . Let the first atom be given momentum along the direction  $A_1B$ , making an angle  $\theta$  with the line of centers  $A_1A_2$ . It moves along  $A_1B$  until a collision occurs when its center reaches  $B$ ; then the second atom moves in the direction  $BA_2$  at an angle  $-\theta_2$  to  $A_1A_2$ . For small angles,

$$A_1B \approx D - 2R$$

$$(D-2R) \theta_1 \approx 2R \theta_2 .$$

Silsbee defines a focusing parameter  $f$  by

$$f = \frac{\theta_2}{\theta_1} .$$

Then

$$f = \frac{D}{2R} - 1. \quad (1-1)$$

$$f > 1 \quad \theta_1 < \theta_2$$

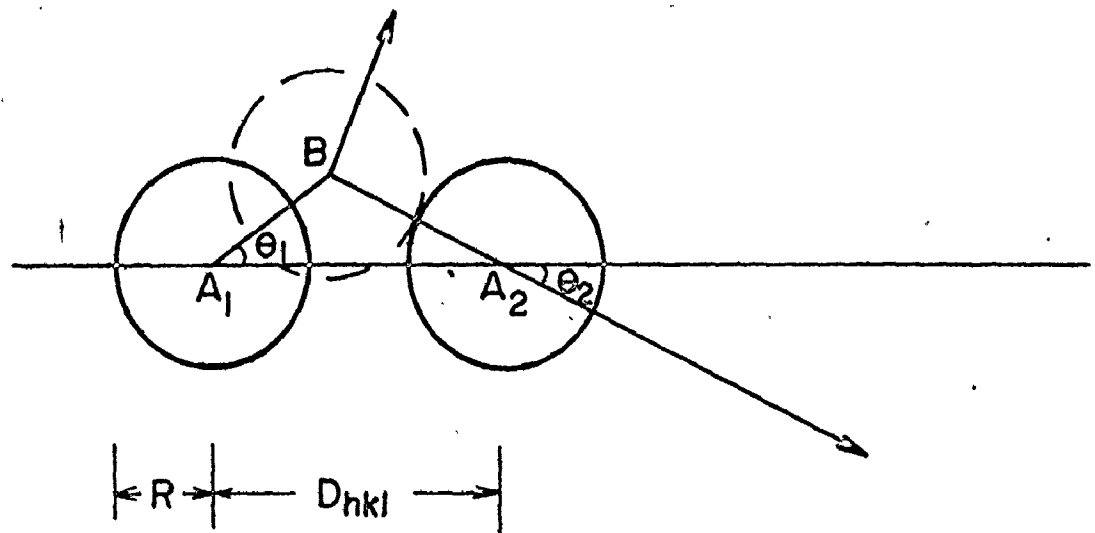


Fig. 1-1 The simple focusing process

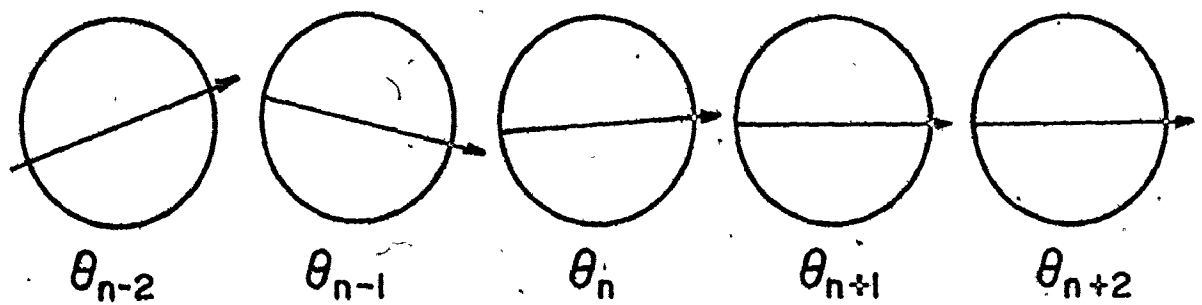


Fig. 1-2 A focused collision sequence

Consider an equally spaced row of atoms as illustrated in figure 1-2 and a sequence of collisions from atom to atom. The relation between  $\theta_n$  and  $\theta_{n-1}$  is

$$\begin{aligned}\theta_n &= f \theta_{n-1} \\ &= f^2 \theta_{n-2} \\ &= f^3 \theta_{n-3}\end{aligned}$$

and finally  $\theta_n = f^n \theta_0$ . (1-2)

If  $D > 4R$  and  $f > 1$ , then  $\theta_2$  diverges and eventually atoms will cease to collide in the line. But if  $D < 4R$  and  $f < 1$  then  $\theta_n$  converges to zero and the final result is a sequence of head-on collisions without any change of angle.

In many gas discharge applications, sputtering is considered a nuisance because it causes erosion of the electrodes, damage to active surface layers in thermionic cathodes, as well as undesired deposits which blacken walls and observation windows. Sputtering can also induce gas pressure changes through "gettering". The implication of sputtering to gas discharges is thus, that it limits the useful life of the various components and the goal was, and often still is, to find ways and means for reducing sputtering.

In thermonuclear fusion, one is concerned about possible sputtering of the container walls by the dominant components of the plasma, namely fast hydrogen ions, fast deuterium ions and fast neutrons. The sputtering yields are much larger for heavy ions so that plasmas must be extremely pure. Only small numbers of atoms sputtered from the walls can cause undesired cooling of the plasma or destruction of the first wall.

An useful application of sputtering can be found in sputter or getter ion pumps which have been developed for applications requiring oil free high vacuum. Getters are materials which remove gas by sorption. Titanium is commonly used as the gettering agent because of its high sorptive capacity for common active gases and its negligibly low vapour pressure. The inert gases are not readily captured and they are usually pumped by ionizing them and accelerating them to a cathode. With sufficient energy they become embedded while at the same time atoms are sputtered from the cathode, usually titanium, and are deposited to form a fresh gettering surface. Altogether one describes the pumping action in terms of both gettering and sputtering.

One of the most active areas based on sputtering deals with the deposition of films and coatings (8,9). An advantage of sputtering is the capability of depositing refractory metals onto various substrates and the capability of depositing compounds of these metals by the addition of reactive gases. This technique of producing doped films is known as reactive sputtering and has found common usage in the deposition of films of oxides, nitrides, etc. Sputtered films are used primarily in thin film circuitry to form resistors, capacitors, electrodes, and metallization contacts in integrated circuits. With the advent of radio frequency sputtering, it is possible to deposit films of virtually all materials including insulators.

There has been an increasing use, in the fabrication of thin

film components, of pattern generation by chemical etching of thin film geometries. This involves the development of a proper etchant for each material system and in addition suffers from limited resolution due to undercutting. Sputtering presents an alternate method of etching surfaces, by making the substrate and film the target, and bombarding with ions. Sputter etching, as the technique is known, has universal applicability and better resolution.

Ion bombardment and sputtering can be used as a technique for microthinning of surfaces for metallurgical and structural investigations. The etching of metal surfaces by ion bombardment has been extensively studied (10), both as an end in itself and as a means of revealing the grain structure.

### 1.3 MODIFICATIONS OF THE SPUTTERED SURFACE

Ion bombardment of a surface not only removes the target material but may disturb the orientation of the crystal lattice near the surface. For example, it has been observed (11) that a single crystal film of gold is progressively disoriented by ion bombardment until it is converted to a random polycrystalline film. Another feature of ion bombardment of metallic surfaces is the formation of characteristic topography (12,13). Several studies have focused on the microtopography of surfaces eroded by ion bombardment (14), which revealed interesting features in the form of hillocks, grooves, and craters. A mechanism of surface micro-roughening by ion bombardment has been recently proposed (15) based on the spatial distribution of damage and its effect on the local sputtering yields at different points on a spike or ridge and be rized as follows.

Let an ion beam bombard a solid target with a plane surface. The average number of sputtered atoms per bombarding ion, i.e. the sputtering yield, is then given by

$$S(x) = \Lambda F_D(x) \quad (1-3)$$

where  $\Lambda$  is a constant characterizing the properties of the target material and  $F_D(x)$  is the average energy deposited per unit depth at a depth  $x$ . In addition to its depth dependence,  $F_D(x)$  also depends on the target-ion mass ratio, ion energy, and angle of incidence.

For an arbitrary geometry (Fig. 1-3), the sputtering yield is given by

$$S(\vec{r}) da = \Lambda F_D(\vec{r}) da \quad (1-4)$$

where  $S(\vec{r})$  is the average number of target atoms sputtered per unit area from a surface element  $da$  at a vector distance  $\vec{r}$  from the point of impact of the bombarding ion and  $F_D(\vec{r})$  is the energy deposited per unit volume at  $\vec{r}$ . Equation (1-4) follows from equation (1-3) by means of the relation

$$F_D(x) = \iiint dy dz F_D(\vec{r}). \quad (1-5)$$

A contour plot of the average deposited energy  $F_D(\vec{r})$  calculated for equal masses of bombarding ion and target (from Winterbon et al. (16)) is shown in figure 1-4. Consider a target surface AB with an angle of incidence  $\nu$  to the ion beam. Due to the initial momentum of the ion the center of the deposited energy distribution is at a finite distance from the point of impact. The

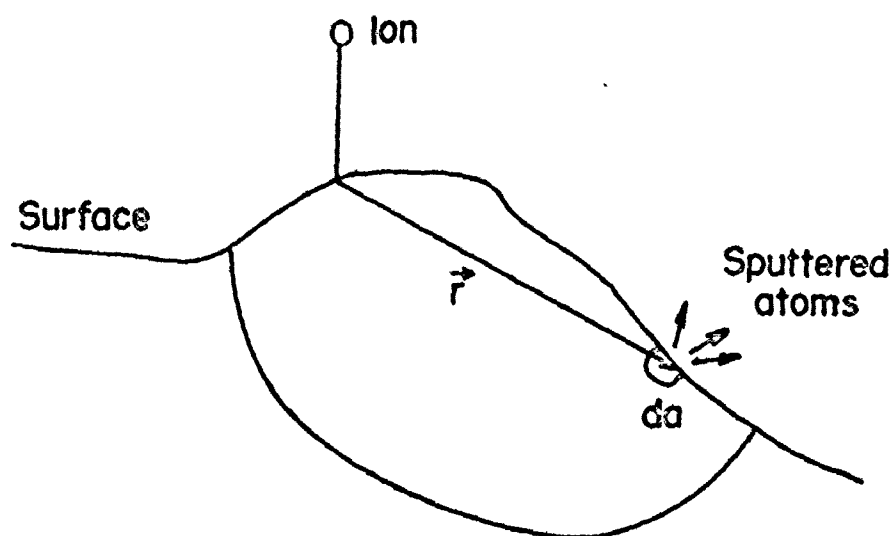


Fig. 1-3 Spatial distribution of the sputtering process. At a distance  $r$  from the point of impact of the ion,  $S(r)da$  atoms are sputtered from the area  $da$ .

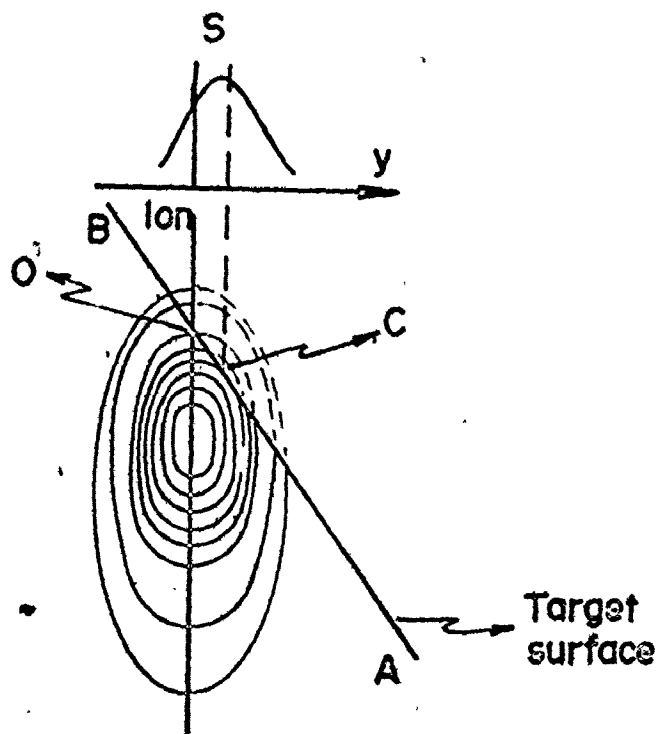


Fig. 1-4 Distribution of sputtering yield along surface for ion incident at O and contour plot of deposited energy. Target surface AB of ring yield at C.



maximum of the deposited energy occurs not at the point of impact O but at a point C and from equation (1-3), the local sputtering yield has its maximum at C. This effect will cause a significant reduction of the local sputtering yield on top of a spike or a ridge and an increase on the bottom of a crater or a groove. The spike or ridge thus remains stable with respect to continued bombardment.

Ion bombardment of semiconductors and insulators exhibiting strong covalent bonding results in different structural changes. Electron microscope studies of ion bombarded Ge (17), Si (18) and GaAs (19) have shown that radiation damage is manifest in the creation of essentially amorphous regions, which steadily increase in number as the bombardment dose builds up until eventually overlap occurs.

Very few studies have been performed on alloys and compounds, especially studies where the target itself was analyzed after ion bombardment. Gillam (20) sputtered a  $\text{Cu}_3\text{Au}$  target and inferred that initially more Cu was removed than would correspond to the 3:1 Cu:Au ratio, leaving behind a layer richer in Au than in  $\text{Cu}_3\text{Au}$ . This altered layer then progressed into the target with further sputtering. Ogar (21) subsequently showed that it is Au and not Cu which is sputtered excessively and that this is the result rather than the cause of radiation enhanced diffusion. Anderson (22) studied the sputtering of the two phase eutectic  $\text{Ag}_{0.6}\text{Cu}_{0.4}$ . By bombarding at  $285^\circ\text{C}$ , with part of the target surface masked to protect the underlying region, he observed the bombarded region

to have a pronounced reddish colour indicative of a Cu coating on the Ag to a depth of  $\sim 1 \mu\text{m}$ . Similarly, Dahlgren and McClanahan (23) sputtered two phased Ag-Ni and Ag-Co targets and found evidence of the Ag being coated with either Ni or Co. The basic result of these studies is a demonstration that ion bombardment leads to a composition change with alloys mainly in an indirect sense by causing radiation enhanced diffusion or an equivalent effect.

Recent studies of ion impact on oxides have given evidence for major changes in structure. For example, bombardment at high doses leads to the crystallization of initially amorphous  $\text{ZrO}_2$  films, to the amorphization of  $\text{Al}_2\text{O}_3$ , and to an enormously increased conductivity with corresponding stoichiometry changes in  $\text{MoO}_3$ ,  $\text{V}_2\text{O}_5$  and  $\text{TiO}_2$ . These effects are reviewed in ref. (24), and in the case of stoichiometry changes, are summarized in Table 1-1. The present work deals with the ion impact changes occurring within  $\text{Nb}_2\text{O}_5$ .

#### 1.4 WHY STUDY $\text{Nb}_2\text{O}_5$ ?

$\text{Nb}_2\text{O}_5$  has been virtually unstudied from a radiation damage point of view in spite of a number of current applications. These include

- a) The role it will play in fusion reactors as the oxide covering of the Nb structure.
- b) Its use in thin film form as a dielectric or an insulator.

In both (a) and (b) the increases in conductivity and the stoichiometry changes such as those to be described here are of obvious

Table 1-1

Examples of bombardment induced stoichiometry changes

Initial State	Structure for medium doses $\leq 1 \times 10^{16}$ ions/cm <sup>2</sup>	Stoichiometry for high doses $\leq 1 \times 10^{17}$ ions/cm <sup>2</sup>	Ref
AgBr	crystalline	Ag	25
Ag <sub>2</sub> O	crystalline	Ag	26
CuO	unknown	Cu <sub>2</sub> O and/or Cu	27
CdI <sub>2</sub>	unknown	Cd	31
MoO <sub>3</sub>	amorphous	MoO <sub>2</sub>	28
MoS <sub>2</sub>	amorphous	Mo	29
Nb <sub>2</sub> O <sub>5</sub>	amorphous	NbO	This thesis
NiO	crystalline	Ni	30
PbI <sub>2</sub>	unknown	Pb	31(a)
PdO	unknown	Pd	30
Ta <sub>2</sub> O <sub>5</sub>	amorphous	amorphous	This thesis
TiO <sub>2</sub>	amorphous	Ti <sub>2</sub> O <sub>3</sub>	32
U <sub>3</sub> O <sub>8</sub>	amorphous	UO <sub>2</sub>	27
V <sub>2</sub> O <sub>5</sub>	amorphous	V <sub>2</sub> O <sub>3</sub>	28

concern.

- c) The same changes in electrical properties which probably compromise the use of  $\text{Nb}_2\text{O}_5$  as a dielectric suggest the fabrication of devices of a different nature in which the conductivity plays a direct role.
- d)  $\text{Nb}_2\text{O}_5$  is also important in a geological context. Although the pure oxide apparently does not occur, the mixed oxide columbite ( $\text{FeO}$ ,  $\text{MnO}$ ) ( $\text{Nb}_2\text{O}_5$ ,  $\text{Ta}_2\text{O}_5$ ) is, owing to the slight uranium content, of potential interest for fission track dating. Studies on damage in  $\text{Nb}_2\text{O}_5$  can provide a basis for understanding track formation in columbite.

More important than the above four points is, however, a fifth:

- e) None of the materials listed in Table 1-1 has been studied with sufficient detail to enable a mechanism for bombardment induced stoichiometry changes to be developed. We will in the present work rectify this situation and come out with a fairly comprehensive experimental and theoretical description. We will, for example show that the new phase develops as a new kind of defect, a zone of changed stoichiometry and that the lost oxygen is sputtered rather than precipitated. A model based on diffusion with trapping accounts for many of the details.

## CHAPTER 2

### A REVIEW OF ION IMPACT THEORY

#### 2.1 INTRODUCTION

An energetic ion entering a target will undergo collisions with the nuclei and electrons of the target, lose its energy, and finally come to rest. The total distance that the ion travels in coming to rest is called its total range, denoted by  $R$ , and the projection of this distance onto the direction of incidence is called the projected range, denoted by  $R_p$  as shown in Fig. 2-1(a). Since the number of collisions and the energy transferred in each collision are random variables, all ions of a given type and initial energy will not have the same values of  $R$  and  $R_p$ . Rather, the ions will form a range distribution, which can be characterized in terms of means  $\langle R \rangle$  or  $\langle R_p \rangle$ , standard deviations  $\langle \Delta R \rangle$  or  $\langle \Delta R_p \rangle$ , and higher moments of the distribution function  $\langle R^m \rangle$  or  $\langle R_p^m \rangle$ . The projected range distribution of all ions can be illustrated as in Fig. 2-1(b), with the following characteristics.

The most probable projected range  $R_{mp}$ , is the peak in the differential range profile. The median range  $R_m$  is the range within which 50% of all the ions have been stopped. The mean projected range,  $\langle R_p \rangle$ , is, as already discussed, the average penetration depth as projected along the normal to the target surface. The mean projected standard deviation  $\langle \Delta R_p \rangle$  is the width of the

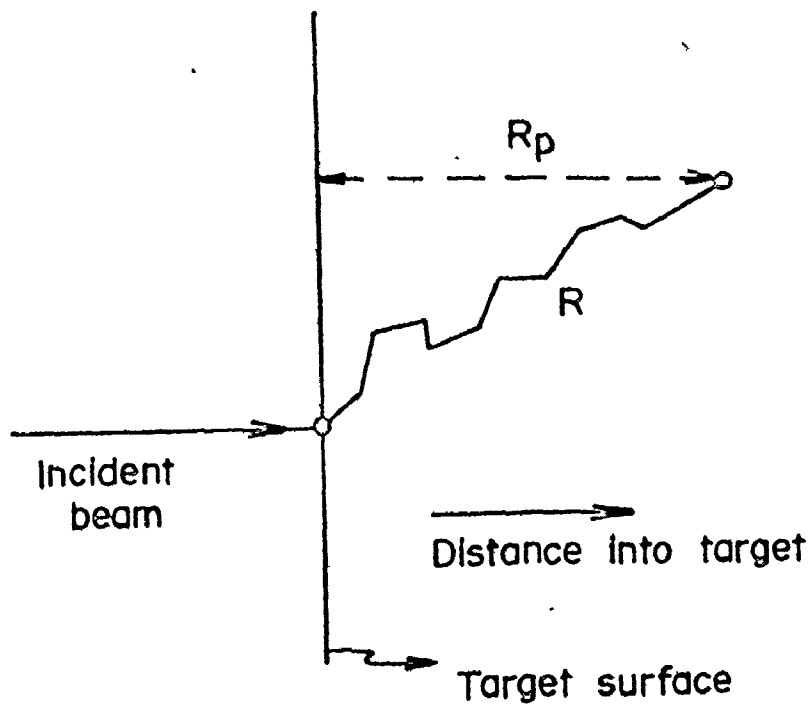


Fig. 2-1(a) Definition of an ion range in terms of  $R_p$ , the projected range

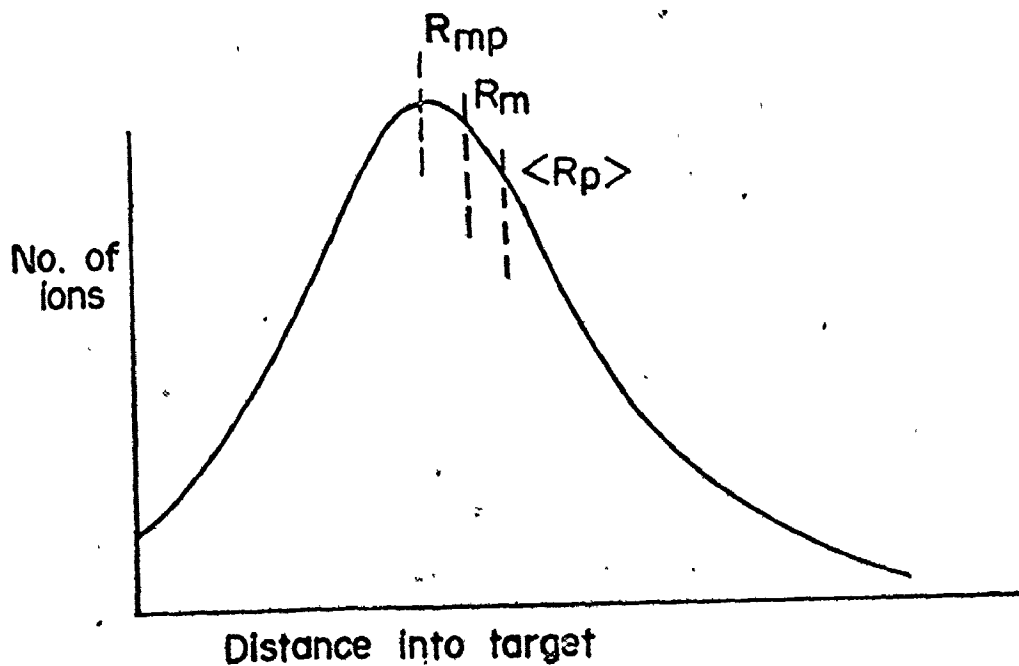


Fig. 2-1(b) An ion range distribution characterized by  $R_{mp}$  (the most probable range),  $\langle R_p \rangle$  (the mean range), and  $R_m$  (the median range).

distribution centered around the mean projected range  $\langle R_p \rangle$  and can be represented as

$$\langle \Delta R_p \rangle = (\langle (R_p - \langle R_p \rangle)^2 \rangle)^{1/2} \quad (2-1)$$

Eq. 2-1 is valid whether or not the distribution is Gaussian.

So far we have considered random collision processes which can be attributed to random or amorphous targets. In amorphous substances the range profiles closely resemble a Gaussian distribution, so that  $R_{mp}$ ,  $R_m$  and  $\langle R_p \rangle$  are nearly equivalent and any departure from Gaussian behaviour manifests itself mainly as a skewness to the right.

Until about 1960 it was assumed that the regular structure of the crystal lattice was not significant in atomic stopping. In studies of the sputtering of single crystal copper, Rol et al. (33) and Almén and Bruce (34) reported low sputtering ratios whenever the ion beam was incident along a low index crystal direction. This was explained on the basis that low index planes present large open avenues for the incident ions and at the same time fewer atoms are exposed to the bombarding particles. At about the same time, Davies et al. (35) found that range profiles exhibit a marked skewness in the form of a deeply penetrating tail when polycrystalline Al samples were used. A little later, Robinson and Oen (36) observed, in a computer calculation of the trajectories of low energy copper ions in a simulated copper lattice, occasional exceptionally long trajectories which apparently resulted from steering by a succession of glancing collisions with

atomic rows. Clear experimental evidence in support of this phenomenon of "ion channeling", as it came to be called, was provided by the work of Nelson and Thompson (37), Lutz and Sizmann (38) and Piercy et al. (39).

So far we have considered the ion distribution during its passage through a solid. A closely related phenomenon is concerned with the spatial extension of the radiation damage induced by the incident ion. Since radiation damage is a consequence mainly of the deposition of energy in the target, the damage distribution is normally equated to that of deposited energy. Just as the ions do not have the same range due to randomness in the collisions and energy transfer, so also the deposited energy will form a distribution which is characterized by

- (1) a mean projected damage range  $\langle R_p^d \rangle$ ,
- (2) a mean projected standard deviation  $\langle \Delta R_p^d \rangle$ , and
- (3) higher moments of the distribution function.

In general, the ion and damage ranges can be calculated from the theories of Lindhard et al. (40), "LSS", and of Winterbon, Sigmund and Sanders (16), "WSS".

## 2.2 ENERGY LOSS MECHANISMS

A starting point in the calculation of ion ranges is the consideration of the two types of energy loss of ions in solids:

- (1) Nuclear stopping,  $\left(\frac{dE}{dx}\right)_n$ , due to elastic interactions between the screened nuclear charges of the ion and the target atoms.



(2) Electronic stopping,  $\left(\frac{dE}{dx}\right)_e$ , due to inelastic collisions between the ion and target electrons.

The total energy loss per unit path length of a moving ion can then be approximated as made up additively of two parts, namely:

$$\frac{dE}{dx} = \left(\frac{dE}{dx}\right)_n + \left(\frac{dE}{dx}\right)_e \quad (2-2)$$

$$\equiv -N[S_n(E) + S_e(E)] \quad (2-3)$$

where  $S_n(E)$  = stopping cross section for energy loss in nuclear collisions

$S_e(E)$  = stopping cross section for energy loss in electronic collisions

$N$  = number of atoms per unit volume in the target.

The quantity  $S_n(E)$  is related to  $d\sigma$ , the differential scattering cross section, by

$$S_n(E) = \int_T^{\Lambda E} T d\sigma \quad (2-4)$$

where  $T$  = Transferred energy ( $\check{T} \leq T \leq \Lambda E$ )

$$\Lambda = \frac{4M_1M_2}{(M_1+M_2)^2}$$

$E$  = Energy of incident ion

$\check{T}$  = Threshold transferred energy for damage

$M_1, M_2$  = Mass of incident ion and target atom respectively.

The quantity  $\check{T}$  is in general badly defined and only relations in

The electronic energy loss  $(\frac{dE}{dx})_e$  is considered to be proportional to ion velocity so that we have

$$(\frac{dE}{dx})_e = -KE^{1/2} \quad (2-5)$$

Knowing the total energy loss, the mean total range of the ion in the target can be written as:

$$\begin{aligned} \langle R \rangle &= \int \frac{dE}{(\frac{dE}{dx})} \\ &= \int \frac{dE}{\left[ (\frac{dE}{dx})_n + (\frac{dE}{dx})_e \right]} \end{aligned} \quad (2-6)$$

### 2.3 LSS THEORY

A treatise on range concepts and heavy ion ranges in random targets has been published by Lindhard, Scharff and Schiøtt (40) and due to its widespread use has come to be known as the LSS theory.

By using a differential scattering cross section based on a Thomas-Fermi potential between the atoms, LSS have derived a universal relationship for the nuclear stopping  $(d\epsilon/d\rho)_n$  in terms of dimensionless energy and length parameters  $\epsilon$  and  $\rho$ . These are defined, in c.g.s. units as:

$$\epsilon = E \left( \frac{a}{e^2} \right) \frac{M_2}{(M_1 + M_2) Z_1 Z_2} \quad (2-7a)$$

$$\rho = R \pi a^2 N \frac{M_1 M_2}{(M_1 + M_2)^2} \quad (2-7b)$$

where 
$$a = \frac{0.8853 a_0}{(z_1^{2/3} + z_2^{2/3})^{1/2}}$$

$$a_0 = \text{Bohr radius (0.0529 nm)}$$

$z_1, z_2$  = atomic numbers of incident ion and target atom respectively.

The nuclear stopping,  $(\frac{d\epsilon}{dp})_n$ , is obtained from numerical solutions of the Thomas-Fermi equation and is tabulated in references (41) and (42). An analytic function which is a good fit to the tabulated points has been used by Winterbon (43) to compute range-energy data for keV ions in amorphous materials.

$$\begin{aligned} s_n(\epsilon) &= - \left( \frac{d\epsilon}{dp} \right)_n \\ &= \frac{9}{8\epsilon} \{ [\log_e (x+r)] - \left( \frac{x}{r} \right) \} \end{aligned} \quad (2-8)$$

where 
$$x = (2\lambda_m \epsilon^{4/3})^{1/3}$$

$$r = (1 + x^2)^{1/2}$$

and  $\lambda_m$  is defined in sect. 2.5.

LSS also used the Thomas-Fermi potential to obtain the contribution due to electronic stopping. The result was a velocity proportional electronic stopping power  $(\frac{d\epsilon}{dp})_e$  given by

$$\left( \frac{d\epsilon}{dp} \right)_e = -k\epsilon^{1/2} \quad (2-9)$$

where

$$k = \xi_e \frac{0.0793 z_1^{1/2} z_2^{1/2} (M_1 + M_2)^{3/2}}{(z_1^{2/3} + z_2^{2/3})^{3/4} M_1^{3/2} M_2^{1/2}}$$

$$\xi_e \sim z_1^{1/6}$$

The electronic stopping calculations do not result in a universal  $(\frac{d\epsilon}{d\rho})_e$  curve, but rather a set of curves each characterized by a particular value of  $k$ , depending on the ion-target combinations.

Theoretical nuclear and electronic stopping power curves, based on the Thomas-Fermi potential and expressed in terms of the reduced parameters  $\epsilon$  and  $\rho$ , are depicted in Figure (2-2) with the following points evident.

- (1) Nuclear stopping is the more important process at low energies, reaching a maximum value at around  $\epsilon = \epsilon_1 = 0.35$  and then falling off.
- (2) Electronic stopping increases linearly with velocity (i.e.  $\epsilon^{1/2}$ ) over a wide range and becomes the dominant process for energies greater than  $\epsilon = \epsilon_2 \sim 3$ .
- (3) At very high energies,  $\epsilon > \epsilon_3$ , the electronic stopping power passes through a maximum and subsequently falls off. This high region is the so called Bethe formula region, where the ion velocity exceeds that of the orbital electrons. This region is far beyond the range of interest in most ion bombardment studies.

To obtain a range energy relationship from the LSS values for  $(\frac{d\epsilon}{d\rho})_n$  and  $(\frac{d\epsilon}{d\rho})_e$  the two terms are taken as being independent and therefore additive:

$$(\frac{d\epsilon}{d\rho})_{\text{total}} = (\frac{d\epsilon}{d\rho})_n + (\frac{d\epsilon}{d\rho})_e \quad (2-10)$$

$$\langle \rho \rangle = \int_0^\epsilon \frac{d\epsilon}{[ (\frac{d\epsilon}{d\rho})_n + (\frac{d\epsilon}{d\rho})_e ]} \quad (2-11)$$

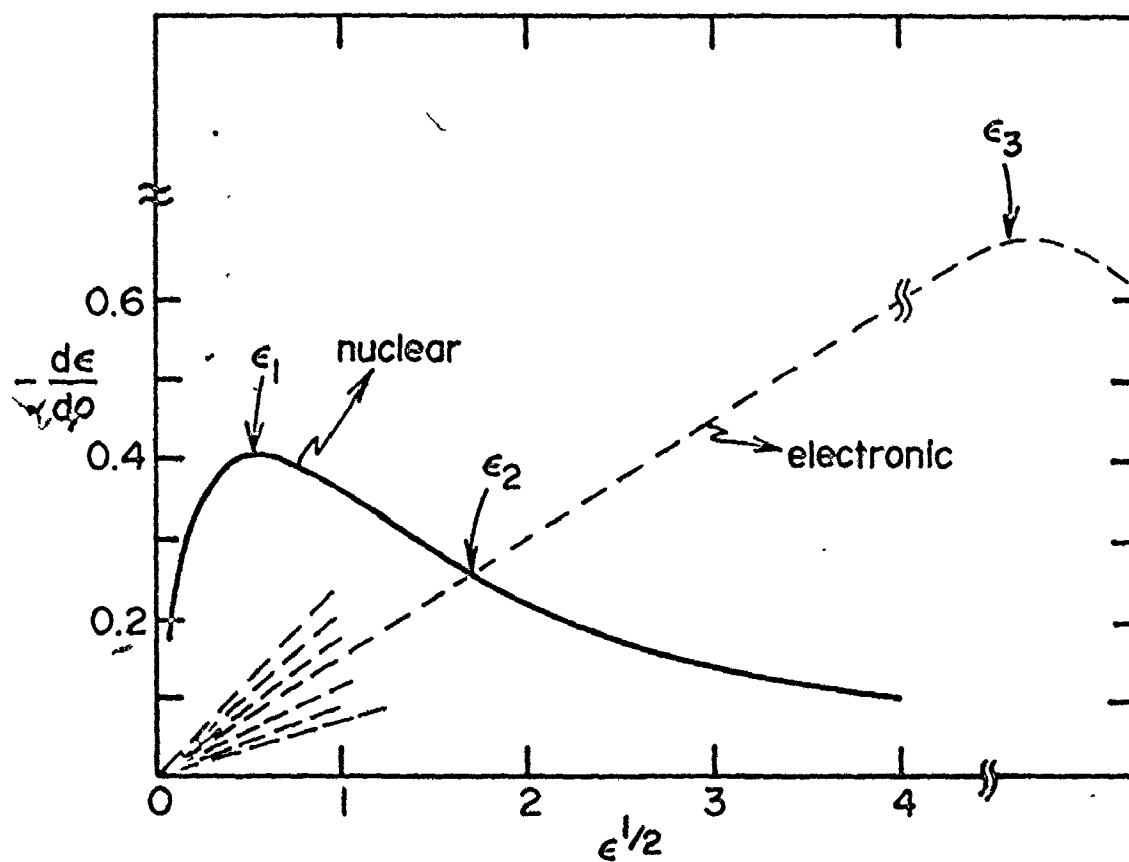


Fig. 2-2 Theoretical nuclear and electronic stopping power curves (based on LSS theory).

Values of  $\epsilon$ ,  $k$ , and  $\langle \rho \rangle$  (the latter for a Thomas-Fermi potential) have been tabulated extensively by Winterbon (43).

#### 2.4 APPLICATIONS OF LSS THEORY

The range of an ion calculated as in equation (2-11) is the total distance  $R$  that the ion travels before coming to rest. The quantity of interest experimentally is the mean projected range  $\langle R_p \rangle$ . Several authors, including Schiøtt (41), consider the probability density functions,  $p(R_p, E)$  and  $q(R_{\perp}, E)$ , for the respective cases of the particle stopping within  $dR_p$  of  $R_p$  and within  $dR_{\perp}$  of  $R_{\perp}$ . Since the function  $p(R_p, E)$  represents the probability that the particle has a projected range between  $R_p$  and  $R_p + dR_p$  we can write

$$\int_0^{\infty} p(R_p, E) dR_p = 1$$

$$\langle R_p^m \rangle = \int_0^{\infty} p(R_p, E) R_p^m dR_p$$

where  $m$  is the order of the moment.

By considering how the probabilities change after an ion penetrates a small thickness  $\delta R_p$ , LSS arrived at the following integro differential equations

$$\frac{\partial}{\partial R_p} \{p(R_p, E)\} = N \int d\sigma \{p(R_p, E-T, \cos\phi) - p(R_p, E)\} \quad (2-12)$$

$$\frac{\partial}{\partial R_{\perp}} \{q(R_{\perp}, E)\} = N \int d\sigma \{q(R_{\perp}, E-T, \cos\phi) - q(R_{\perp}, E)\}, \quad (2-13)$$

where  $\phi$  is the scattering angle in laboratory coordinates and  $T$  is the energy transferred in a collision. Eqs. (2-11) and (2-13) neglect electronic stopping, though can be readily extended to include it.

Further details about the solution of these equations have been described elsewhere (41) and will not be given here. Extensive calculations based on eq. (2-12), as modified to include electronic stopping, to yield projected range statistics in a wide range of semiconductors have been published by Johnson and Gibbons (44).

Integro differential equations for range distributions have been derived and solved by Sigmund and Sanders (45) using a different notation for the distribution functions. The function  $f(\bar{r}, \bar{v})$  is defined as the probability density of an ion with initial velocity  $\bar{v}$  to come to rest at a vector distance  $\bar{r}$  from its starting point  $\bar{r} = 0$ . The distribution function obeys the following transport equation:

$$\frac{\partial}{\partial r} \{f(\bar{r}, \bar{v})\} = N \int d\sigma \{f(\bar{r}, \bar{v}) - f(\bar{r}, \bar{v}')\}, \quad (2-14)$$

where  $d\sigma$  is the cross section for scattering from velocity  $\bar{v}$  to velocity  $(\bar{v}', d\bar{v}')$ .

It turns out that the equations governing the spatial distribution of deposited energy are similar to those describing the distribution of ion ranges. This is contained in the theory of Winterbon, Sigmund and Sanders (WSS) which is treated in the next section.

## 2.5 WSS THEORY

(Winterbon, Sigmund and Sanders Theory)

Integral equations for range and damage distributions have been derived and solved by several authors (40, 41, 45, 46, 47). The most exhaustive study was performed by WSS (16) and can be summarized as follows.

It was assumed that:

- 1) the medium is random and infinite (as with LSS),
- 2) the collisions are elastic (LSS allowed for inelastic events),
- 3) the differential scattering cross section can be represented by

$$d\sigma(E, T) = \frac{C dT}{E^m T^{1+m}}, \quad (2-15)$$

where  $m = 0, 1/3, 1/2 \text{ or } 1$

$$C = \frac{\pi}{2} \lambda_m a^2 \left(\frac{M_1}{M_2}\right)^m \left(\frac{2Z_1 Z_2 e^2}{a}\right)^{2m}$$

$$\lambda_0 = 24; \quad \lambda_{1/3} = 1.309;$$

$$\lambda_{1/2} = 0.327; \quad \lambda_1 = 0.5.$$

Equation (2-15) with  $m = 1/3, 1/2 \text{ or } 1$  represents the cross section for a power potential,

$$V(r) = \frac{A}{r^{1/m}} \left(\frac{1}{3} \leq m \leq 1\right), \quad (2-16)$$

with fairly good accuracy (16) but can also be used with  $m = 0$

to describe scattering by a Born-Mayer Potential (51). In general

$m = 0$  is valid for very low energies, being an alternative to the Born-Mayer Potential;

$m = \frac{1}{3}$  is valid for moderately low energies ( $\epsilon \leq 0.2$ );



$m = \frac{1}{2}$  is valid for almost the whole range of keV energies as in the present study ( $0.08 \leq \epsilon \leq 2$ );

$m = 1$  is valid for high energies ( $\epsilon \geq 10$ ) though is not too useful as the neglect of electronic stopping is then the most serious.

WSS defined probability distribution functions for ion and damage distributions which are the same as that in eq. 2-14 and are equivalent to that in eq. 2-12:

$f(\bar{r}, \bar{v}) d^3\bar{r}$  = probability for a projectile starting with a velocity  $\bar{v}$  at the origin ( $\bar{r} = 0$ ) to come to rest in the volume element  $(\bar{r}, d^3\bar{r})$ .

$f_D(\bar{r}, \bar{v}) d^3\bar{r}$  = energy deposited in nuclear motion by the projectile and recoil atoms in the volume element  $(\bar{r}, d^3\bar{r})$  at the end of the slowing down process.

Normalizing conditions require that

$$\begin{aligned} \int f(\bar{r}, \bar{v}) d^3\bar{r} &= 1 \\ \int f_D(\bar{r}, \bar{v}) d^3\bar{r} &= v(E), \end{aligned}$$

where  $v(E)$  is the amount of energy spent in nuclear motion immediately after slowing down.  $f(\bar{r}, \bar{v})$  obeys equation 2-14, while for  $f_D(\bar{r}, \bar{v})$  we have the following transport equation:

$$\frac{\partial}{\partial r} \{f_D(\bar{r}, \bar{v})\} = N \int d\sigma \{f_D(\bar{r}, \bar{v}) - f_D(\bar{r}, \bar{v}') - f_D(\bar{r}, \bar{v}'')\} \quad (2-17)$$

$d\sigma = d\sigma(\bar{v}, \bar{v}')$  is the cross section for scattering from velocity  $\bar{v}$  to velocity  $\bar{v}'$ ,  $d\bar{v}'$

$d\sigma = d\sigma(\bar{v}, \bar{v}'')$  is the cross section for starting a recoil atom  $\bar{v}''$

The next step is to calculate the spatial averages over the distribution functions and finally to insert these into an Edgeworth expansion (48). It converges best when the distribution under consideration is similar to a Gaussian, which is the case for the amorphous targets with  $M_2 > M_1$ . To approximate a distribution function by the Edgeworth expansion, one proceeds as follows.

Let the probability function of interest be  $C(x)$ .

Introduce  $\mu_n$  and  $\xi$ :

$$\begin{aligned}\mu_n &\equiv \langle \Delta x^n \rangle = \langle (x - \langle x \rangle)^n \rangle \\ \xi &\equiv \frac{(x - \langle x \rangle)}{\mu_2^{1/2}}\end{aligned}\quad (2-18)$$

Then  $C(x)$  can be represented as

$$C(x) = C(\xi) = \frac{1}{(2\pi\mu_2)^{1/2}} \exp(-\xi^2/2) g(\xi) \quad (2-19)$$

where

$$\begin{aligned}g(\xi) = & 1 - \left(\frac{1}{6}\right) \frac{\mu_3}{\mu_2^{3/2}} (3\xi - \xi^3) \\ & + \left(\frac{1}{24}\right) \left(\frac{\mu_4}{\mu_2^2} - 3\right) (3 - 6\xi^2 + \xi^4) \\ & - \left(\frac{1}{72}\right) \left(\frac{\mu_3^2}{\mu_2^3}\right) (15 - 45\xi^2 + 15\xi^4 - \xi^6) .\end{aligned}$$

This result can be proven by forming various moments, for example

$$\langle x \rangle = \int x C(x) dx ,$$

and carrying out the required integration. If only the first term of  $g(\xi)$  is taken into account one has a simple Gaussian with a width

$\mu_2^{1/2}$  centered around  $x = \langle x \rangle$ .

## 2.6 RANGE AND DAMAGE PROFILES

Using either LSS or WSS theory together with an Edgeworth expansion, range and damage profiles can be constructed. They are strictly speaking differential profiles, so we will therefore write  $C^{\text{diff}}(x)$  instead of  $C(x)$ .

Experimentally one normally observes not  $C^{\text{diff}}(x)$  but rather the integral profile, i.e. the integral concentration  $C^{\text{int}}(x)$ . A very useful technique consists of stripping away known thicknesses from a bombarded specimen and measuring the amount of material which remains or the amount which is removed. In many cases it is convenient to use radioactive ions for bombardment and the integral range distributions then indicate the fractional radioactivity remaining in the specimen as a function of the thickness of material removed. The analytic form of  $C^{\text{int}}(x)$  is readily obtained when  $C^{\text{diff}}(x)$  is expressed as an Edgeworth expansion:

$$\begin{aligned} C^{\text{int}}(x) &= \int_x^\infty C^{\text{diff}}(x) dx \\ &= \int_x^\infty \frac{1}{(2\pi\mu_2)^{1/2}} \exp\left[-\frac{(x-\langle x \rangle)^2}{2\mu_2}\right] dx \\ &= \text{erfc}\left[\frac{x-\langle x \rangle}{(2\mu_2)^{1/2}}\right] h(\xi), \end{aligned} \quad (2-20)$$

where  $h(\xi)$  is a correction term (49) which reduces to unity for a Gaussian distribution.

Hence for a Gaussian distribution

$$C^{\text{int}}(x) = \frac{1}{2} \operatorname{erfc}\left[\frac{(x-\langle x \rangle)}{(2\mu_2)^{1/2}}\right] \quad (2-21)$$

where  $\frac{1}{2}$  serves as an approximate normalization.

## 2.7 THEORY OF ROL, FLUIT AND KISTEMAKER

It was proposed by Rol, Fluit and Kistemaker (50) that it is those collisions of the ion which take place near the target surface which are primarily responsible for sputtering. The sputtering yield is therefore proportional to the average energy dissipated by the incident ion in the first few atomic layers by elastic scattering events. Particles set in motion deep under the surface will have very little chance to reach the surface and escape. The probability that an ion will have a collision near the surface is inversely proportional to  $\lambda$ , the mean free path for elastic collisions.

Since the energy transferred in the first collision is proportional to

$$\frac{M_1 M_2}{(M_1 + M_2)^2} E \quad (2-22)$$

the sputtering yield  $S$  can be expressed as

$$S = \frac{K}{\lambda} \frac{M_1 M_2 E}{(M_1 + M_2)^2} \quad (2-23)$$

where  $K$  is a constant depending on the target.

The mean free path  $\lambda$  is given as usual in terms of the target atomic density  $N$  and the total scattering cross section  $\sigma$

$$\lambda = \frac{1}{N\sigma} \quad (2-24)$$

Rol et al. have assumed the hard sphere approximation to be a valid description of the scattering process, in which  $\sigma = \pi \rho_o^2$  where  $\rho_o$  is the distance of closest approach:

$$\lambda = \frac{1}{N\pi\rho_o^2} \quad (2-25)$$

Attractive as it is, this theory must be regarded today as obsolete. This is mainly because of the empirical factor K.

## 2.8 SIGMUND'S THEORY OF SPUTTERING

The sputtering of a target by energetic ions was assumed by Sigmund (51,52) to result from cascades of atomic collisions.. The sputtering yield was then calculated under the assumption of random slowing down in an infinite medium. The theory as developed can be summarized as follows.

Let an incident ion slow down from an initial energy E at  $t = 0$ . The number of atoms set in motion in the resulting cascade is described by the distribution function  $F(E, E_o, t)$  defined in the following way.

$\int_0^E F(E, E_o, t) dE_o$  is the average number of atoms moving with energy  $(E_o, dE_o)$  at time t in a collision cascade started at  $t = 0$  by an ion with an initial energy E. The function  $F(E, E_o, t)$  satisfies the transport equation

$$-\frac{1}{v} \frac{\partial}{\partial t} F(E, E_o, t) = N \int d\sigma \{ F(E, E_o, t) - F(E-T, E_o, t) - F(T, E_o, t) \}, \quad (2-26)$$

similar to the equations for the range and damage distributions (sect. 2.5). A possible derivation of this equation will now be

wh have previously

are both self contained and reasonably brief.

Let a moving atom travel a path length segment  $\Delta r$ . If  $\Delta r$  is small enough the atom will not come to rest but may undergo a collision specified by a cross section  $d\sigma$ , the probability for which is given by

$$dP = N \Delta r d\sigma .$$

By taking into account the probability for a collision involving a transferred energy  $T$  and the complementary probability for not making a collision, we have

$$\begin{aligned} F(E, E_0, t) = N \Delta r \int d\sigma \{ F(E-T, E_0, t-\Delta t) + F(T, E_0, t-\Delta t) \} \\ + (1-N \Delta r \int d\sigma) \{ F(E, E_0, t-\Delta t) \} \end{aligned} \quad (2-27)$$

$$\frac{F(E, E_0, t-\Delta t) - F(E, E_0, t)}{\Delta r} = N \int d\sigma \{ F(E, E_0, t-\Delta t) - F(E-T, E_0, t-\Delta t) - F(T, E_0, t-\Delta t) \}$$

But  $\Delta r = v \Delta t$  and therefore

$$-\frac{1}{v} \frac{\partial}{\partial t} F(E, E_0, t) = N \int d\sigma \{ F(E, E_0, t) - F(E-T, E_0, t) - F(T, E_0, t) \} .$$

The distribution in energy of all slowing down atoms averaged over all time, due to bombardment of  $\phi$  ions/cm<sup>2</sup>, is given by

$$G(E, E_0) dE_0 = \phi dE_0 \int_0^{\infty} dt F(E, E_0, t) . \quad (2-28)$$

Note that the function  $G(E, E_0) dE_0$  applies to the whole target, i.e. all  $x$ .

In the calculation of the distribution functions, a cross

obvious choice from the mathematical point of view is the power cross section with  $m=0$ , recently proposed as an approximation to the Born-Mayer potential. This cross section as discussed in sect. 2-5 has the form

$$d\sigma = C_0 \frac{dT}{T} \quad (2-29)$$

and makes possible the following asymptotic solution for  $G(E, E_0)$ :

$$G(E, E_0) dE_0 = \frac{6\phi}{\pi^2} \frac{v(E)}{v_0 N C_0} \frac{dE_0}{E_0^2} \quad (2-30)$$

where  $v(E)$  is the energy deposited in nuclear collisions and  $v_0$  is the velocity of target atoms having an energy  $E_0$ . The details of the asymptotic solution are given by Robinson (53).

As a next step towards the determination of the sputtering yield, the average number of atoms moving in a layer  $(x, dx)$  into the solid angle  $(\Omega, d\Omega)$  and with energy  $(E_0, dE_0)$  is calculated based on the following assumptions:

- i) The angular distribution of moving atoms is isotropic in the limit  $E_0 \ll E$ .
- ii) The distribution in energy and direction of moving atoms is independent of depth.

The deposited energy  $v(E)$  can then be replaced by the depth distribution of deposited energy

$$v(E) = \int C_d^{\text{diff}}(x, E) dx$$

where  $C_d^{\text{diff}}(x, E)$  is the amount of energy deposited in a layer  $(x, dx)$  by an ion of energy  $E$  starting at  $x = 0$ .

The average number of atoms moving in the layer  $(x, dx)$  into the solid angle  $(\Omega, d\Omega)$  with energy  $(E_0, dE_0)$  is given by

$$G(E, E_0, x, \Omega) dE_0 dx d\Omega = \frac{6\phi}{\pi^2} \frac{C_d^{\text{diff}}(x, E) dE_0 d\Omega dx}{E_0^2 v_0 N C_0 4\pi} \quad (2-31)$$

This function, unlike  $G(E, E_0) dE_0$ , applies only in the layer  $(x, dx)$ .

The flux out through the surface  $x = 0$  is then given by multiplying with  $v_0 \cos \theta_0$ , the velocity component along the normal to the surface

$$H(E, E_0, \Omega) dE_0 d\Omega = \frac{6\phi}{\pi^2} \frac{C_d^{\text{diff}}(0, E) \cos \theta_0 d\Omega dE_0}{E_0^2 N C_0 4\pi} \quad (2-32)$$

This expression would give the distribution of sputtered atoms as specified by energy and direction if no surface binding forces were present. Note in particular the characteristic  $E_0^{-2}$  energy dependence and the  $\cos \theta_0$  dependence on the direction of the sputtered atoms.

The final step is to consider a surface binding energy  $E_b$ , so that the condition for sputtering is that the energy corresponding to the velocity component normal to the surface is greater than  $E_b$

$$E_0 \cos^2 \theta_0 \geq E_b$$

The total number of atoms sputtered per incident ion, normally called the sputtering yield  $S$ , is then given by

$$S = \frac{\iint H(E, E_0, \Omega) dE_0 d\Omega}{\phi} \quad (2-33)$$

where the limits of  $E_0$  are  $E_b / \cos^2 \theta_0$  to  $E$  and the limits of  $d\Omega$

ult is



$$S = \frac{3}{4\pi^2} \frac{C_d^{\text{diff}}(0, E)}{N C_o E_b} \quad (2-34)$$

Since the function  $C_d^{\text{diff}}(x, E)$  has the dimensions of an energy per depth we can write

$$\begin{aligned} C_d^{\text{diff}}(0, E) &= -\alpha \left( \frac{dE}{dx} \right)_n \\ &= \alpha N S_n(E) \end{aligned} \quad (2-35)$$

where  $\alpha$  is a dimensionless quantity depending only on  $m$ ,  $M_1$  and  $M_2$  and  $S_n(E)$  is the nuclear stopping cross section.  $S$  now takes the form

$$S = \frac{3}{4\pi^2} \frac{\alpha S_n(E)}{C_o E_b}$$

The constant  $C_o$  follows from

$$C = \frac{\pi}{2} \lambda_m a^2 \left( \frac{M_1}{M_2} \right)^m \left( \frac{2Z_1 Z_2 e^2}{a} \right)^{2m},$$

with  $m = 0$  resulting in

$$C_o = \frac{\pi}{2} \lambda_o a^2.$$

The constants  $\lambda_o$  and  $a$  are chosen to fit the power law cross sections of eq. (2-29) to the theoretical cross section for a Born-

Mayer potential. Sigmund's (51) results are:

$$\lambda_o = 24$$

$$a = 0.0219 \text{ nm.}$$

The sputtering yield,  $S$ , with the constants evaluated is given by

$$S = 0.042 \frac{\alpha S_n(E)}{E_b} \quad (2-36)$$

The evaluation of the sputtering yield for a given ion-target combination is greatly facilitated when  $S_n(E)$  is expressed in terms of  $s_n(\epsilon)$ , the reduced nuclear stopping cross section, which is a universal function tabulated by Lindhard et al. (42).

The sputtering yield  $S$  can be written as

$$S = 0.703 \frac{\alpha M_2 \hat{\rho}}{E_b \hat{\epsilon}} s_n(\epsilon), \quad (2-37)$$

where  $M_2$  is the atomic weight of the target,  $\hat{\rho}$  the dimensionless length unit for  $1 \mu\text{g}/\text{cm}^2$  of target material and  $\hat{\epsilon}$  the value of  $\epsilon$  for  $E = 1 \text{ keV}$ .  $\hat{\rho}$  and  $\hat{\epsilon}$  are tabulated by Winterbon (43) for many ion-target combinations.

## 2.9 ENERGY DISSIPATION IN COMPOUND TARGETS

Recently, Andersen and Sigmund (54) have studied theoretically the sharing of energy among the constituents of a polyatomic medium in random atomic collision cascades initiated by heavy ion impact. If the energy is distributed non stoichiometrically, preferential displacement of one particular atomic species may result and composition changes may occur. The changes could be either in the interior, due to internal rearrangement or near the surface, due to preferential sputtering.

Consider a random medium with  $N_j = \alpha_j N$  atoms of type  $j$  (atomic number  $Z_j$ , atomic mass  $M_j$ ) per unit volume where  $\alpha_j$  ( $\sum \alpha_j = 1$ ) is the atom fraction of  $j$  atoms. Let an atom of type  $i$  with initial energy  $E$  slow down in the medium. Following Sigmund's theory as outlined in sect. 2.8, similar distribution functions are used to describe the moving atoms in the cascade.

$F_{ij}(E, E_0, t)$  is defined as the average number of  $j$  atoms moving with energy  $(E_0, dE_0)$  at time  $t$  in a collision cascade initiated at  $t=0$  by an  $i$  atom with initial energy  $E$ .

The distribution in energy of all slowing down  $j$  atoms averaged over all time due to bombardment of  $\phi$  ions/cm<sup>2</sup> is given by

$$G_{ij}(E, E_0) dE_0 = \phi dE_0 \int_0^{\infty} dt F_{ij}(E, E_0, t) .$$

The distribution functions obey the following integral equations:

$$\sum_K \alpha_K \int d\sigma_{iK} \{F_{ij} - F'_{ij} - F''_{Kj}\} = \alpha_j \frac{d\sigma_{ij}(E, E_0)}{dE_0} \quad (2-38)$$

$$\sum_K \alpha_K \int d\sigma_{iK} \{G_{ij} - G'_{ij} - G''_{Kj}\} = \frac{\phi}{Nv_0} \delta_{ij} \delta(E - E_0) \quad (2-39)$$

where  $F'_{ij} = F_{ij}(E - T, E_0)$

$F''_{ij} = F_{ij}(T, E_0)$

$v_0$  = velocity of a  $j$ -atom with energy  $E_0$ ,

$G'_{ij}$  and  $G''_{ij}$  are defined similarly as  $F'_{ij}$  and  $F''_{ij}$ .

$\delta_{ij} = 1$  for  $i = j$

$= 0$  for  $i \neq j$

$\delta(E - E_0)$  = Dirac's delta function

$= \infty$  for  $E = E_0$

$= 0$  for  $E \neq E_0$ .

As before a differential scattering cross section of the

law

$$d\sigma_{ij}(E, T) = C_{ij} E^{-m_i} T^{-1-m_i} dT,$$

is used in the solution of the integral equations.

When calculating the distribution functions the cross sections that are applicable at low particle  $E_0$  are used. Andersen and Sigmund have used two values of  $m$  namely 0.055 and 0.333 and studied the implication of the equations for binary compounds. Both choices, namely  $m_1 \neq m_2$  and  $m_1 = m_2$  have been considered. In the case of  $m_1 \neq m_2$ ,  $m = 0.333$  has been used for the lighter element and  $m = 0.055$  for the heavier element.

The theory of Andersen and Sigmund leads to the calculation of the average number  $N_i$  of displaced  $i$ -atoms given by

$$N_i = \frac{E}{E_{di}} \alpha_i K_i, \quad (2-40)$$

where  $E_{di}$  is the displacement threshold energy for atoms of type  $i$  and  $K_i$  is the displacement efficiency.

The significant parameter is  $K_i$ , which is not necessarily 0.5 as often assumed. Andersen and Sigmund (55) deduced the displacement efficiencies for the systems W-O, Nb-O and Ti-O. The results for the system Nb-O are illustrated in figure 2-3 and tabulated in Table 2-1. It can be noted that, for stoichiometry  $Nb_2O_5$ , one has

$$K_O > K_{Nb}.$$

This suggests that bombardment of  $Nb_2O_5$  might lead to internal displacement of oxygen and one of the objects of what follows will be to test this idea.

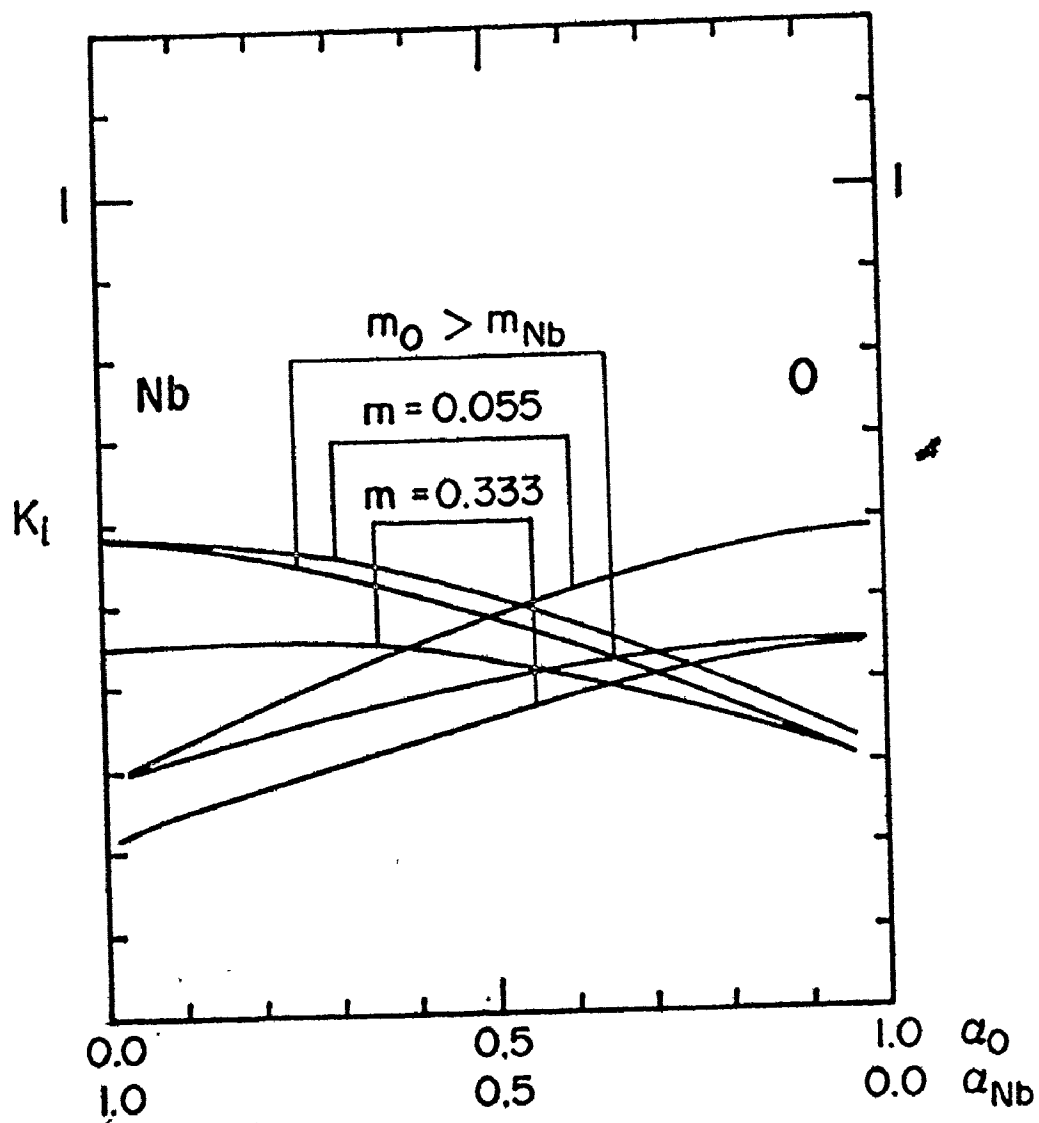


Fig. 2-3 Displacement efficiencies for the system Nb-O (after Sigmund (55)).

Table 2-1

Displacement efficiencies for the system Nb-O

	$m_O > m_{Nb}$		$m = 0.055$		$m = 0.333$	
	$K_{Nb}$	$K_O$	$K_{Nb}$	$K_O$	$K_{Nb}$	$K_O$
$Nb_2O_5$	0.40	0.43	0.43	0.54	0.38	0.42
$NbO_2$	0.43	0.43	0.45	0.52	0.39	0.40
$NbO$	0.48	0.40	0.51	0.48	0.43	0.36

## CHAPTER 3

### EXPERIMENTAL TECHNIQUES

#### 3.1 SAMPLE PREPARATION

##### 3.1.1 Anodic Thin Films of $\text{Nb}_2\text{O}_5$

Polycrystalline Nb specimens, with dimensions of  $20 \times 20 \times 0.1$  mm and with a purity of 99.98% were used to form anodic oxide films. The specimens were chemically polished in a solution made up of  $60 \text{ cm}^3$  hydrofluoric acid,  $100 \text{ cm}^3$  nitric acid and  $60 \text{ cm}^3$  acetic acid. Anodic oxide films were formed in an aqueous solution of 0.25% KF at room temperature using a platinum cathode. It has been reported by Pawel and Campbell (56) that, in order to be able to strip large areas of anodic oxide film, it is desirable to anodize the specimens in a solution containing a small amount of fluoride ion. A preanodizing treatment was given which consisted of the successive formation and dissolution of several anodic layers. The anodic oxidations were carried out at a preset current density of  $5 \text{ mA/cm}^2$  and a preset potential of 20 V. The weight increase of an anodized specimen as determined by using a microbalance is due primarily to the oxygen pickup. This increase yields the film thickness provided one makes assumptions regarding the film density. For the case of  $\text{Nb}_2\text{O}_5$ , the film density was taken as  $4.74 \text{ g/cm}^3$  (57). If  $w$  is the weight increase ( $\mu\text{g}$ ) for a total area of  $A$  ( $\text{cm}^2$ ), then the thickness of  $\text{Nb}_2\text{O}_5$  film ( $t$ )

can be determined by

$$t = \frac{W}{A} \times \frac{10}{4.74} \text{ nm.} \quad (3-1)$$

In the present study the typical film thickness was about 60 nm.

Specimens for transmission electron microscopy were prepared by coating the surface of the anodized specimen with a 2% solution of parlodion in amyl acetate. The solution was allowed to dry and the resulting film peeled off removing with it the underlying oxide film. Small pieces of the film were supported on 200 mesh microscope grids and the parlodion was dissolved by several washings with amyl acetate. Anodic films of  $\text{Nb}_2\text{O}_5$  supported on such grids were used as the targets for ion bombardment and subsequent observation in the electron microscope.

### 3.1.2 Sintered Pellets

Sintered  $\text{Nb}_2\text{O}_5$  pellets (10 mm in diameter, 5 mm in height) were prepared by pressing powdered  $\text{Nb}_2\text{O}_5$  (supplied by Alfa Inorganics, Beverly, Mass.) in a circular die. The pellets were then placed in a Pt boat and sintered for 24 h in air at 1300°C and furnace cooled to room temperature. Subsequently, the pellets were polished to produce the necessary smooth surface for four point probe electrical conductivity measurements (58,59) and refired at 1300°C for 4 h. It has been established by several studies on the defect structure of  $\text{Nb}_2\text{O}_5$  (60,61,62) that sintering in air at temperatures between 1300°C and 1350°C results in  $\alpha\text{-Nb}_2\text{O}_5$ , the stable form of  $\text{Nb}_2\text{O}_5$  with a monoclinic structure.

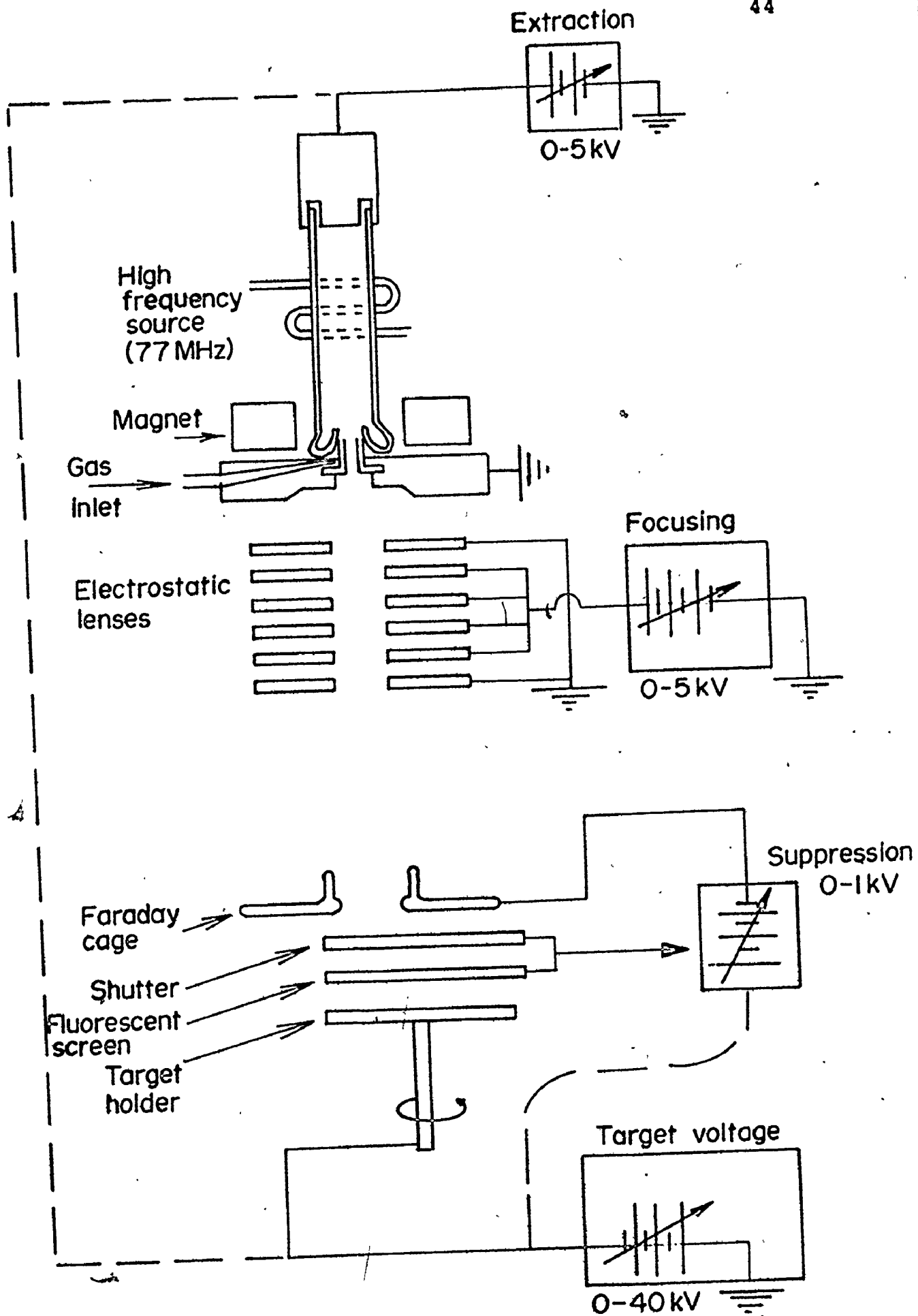


### 3.2 ION BOMBARDMENT

Only a very brief description of the ion accelerator will be presented in this section as more details have been given elsewhere (63). The ion accelerator, designed with a radio frequency (77 MHz) ion source, could be operated at energies varying from 2 to 40 keV and at currents varying from 2 to 50  $\mu$ A. The ion accelerator has no mass separation. This is to some extent compensated by the use of heavy ions, since the impurities would be of low mass and would create less damage. The accelerator set-up is illustrated schematically in Fig. 3.1.

A plasma is formed by a gas discharge within a glass envelope containing the gas to be ionized by means of an oscillator which is coupled to the discharge through a coil placed outside the envelope. In addition, a magnetic coil provides an axial magnetic field which is used to intensify the discharge by converting linear electron paths into helical paths and thereby increasing the efficiency of ionization. A positive ion beam is extracted from this plasma through a small canal (1.5 mm in diameter, 14 mm long) by application of a positive voltage in the range 2000-5000 V. to the top of the glass envelope.

A series of focusing electrodes is used to shape and focus the ion beams. The arrangement is similar to an electrostatic unipotential or Einzel lens. The Einzel lens is characterized by two electrodes at equal potential symmetrically arranged about a central electrode (or a set of electrodes) at a different potential. The target is connected to the negative terminal of a



high voltage power supply with a variable output voltage of 0 to 40 kV.

When an ion beam hits a target surface, secondary electrons are produced and the contribution of these secondary electrons to the total ion current should be suppressed in order to get a true ion current. Suppression is accomplished by surrounding the target with electrodes connected to a variable power supply at negative voltage. If the ion current is monitored as a function of the suppression voltage, the region where the ion current is independent of this voltage can be determined. In the present set-up a typical value was -800 V. To convert the ion current density to ion dose the following conversion factor is used\*:

$$\begin{aligned} 1 \mu\text{A-min} &= 3.7 \times 10^{14} \text{ ions} \\ 1 \mu\text{A-min/cm}^2 &= 3.7 \times 10^{14} \text{ ions/cm}^2. \end{aligned} \quad (3-2)$$

The uniformity of the ion beam can be tested by bombarding anodized Ta specimens, and noting the colour changes. That is, due to sputtering, the thickness of the anodic oxide decreases and hence the colour changes. A uniform colouration of the surface after bombardment is a good indication of a uniform beam

---


$$\begin{aligned} * 1 \mu\text{A-min} &= 60 \times 10^{-6} \frac{\text{coulombs}}{\text{sec}} \text{ sec} \\ &= \frac{6 \times 10^{-5}}{1.6 \times 10^{-19}} \frac{\text{coulombs}}{\text{coulombs}} \text{ electrons} \\ &= 3.7 \times 10^{14} \text{ ions.} \end{aligned}$$

to within 5%.

The errors involved in the determination of the ion dose can be rather large. Errors in beam size can contribute an error of at least 10%. The greatest error, however, is introduced by beam instabilities and discharge fluctuations especially during long irradiations (about 1 h). In conjunction with beam size and inhomogeneity the uncertainty in the total dose is typically of the order of 25% or more.

### 3.3 ELECTRICAL CONDUCTIVITY MEASUREMENTS

#### 3.3.1 Terminology

##### Resistivity

The resistivity ( $\rho$ ) of a material is defined by the expression

$$R = \frac{\rho l}{A}, \quad (3-3)$$

where  $R$  is the resistance of a specimen,  $l$  is its length and  $A$  its cross sectional area. Resistivity has until now been expressed in "ohm centimeters", denoted by  $\Omega \cdot \text{cm}$ , though will in the near future probably be given in "ohm.meters".

##### Conductivity

The conductivity ( $\sigma$ ) of a material is the reciprocal of resistivity

$$\sigma = \frac{1}{\rho}$$

and is denoted at present by  $\Omega^{-1} \text{cm}^{-1}$ . We will anticipate future usage in this matter and use the notation S/m, where S stands for Siemens.

### Sheet Resistivity

Consider a rectangularly shaped section of a thin film or layer of thickness  $w$  and having the dimensions of length  $\ell$  and width  $b$ . This is illustrated in Fig. 3.2. The resistance of the film  $R$  from (1) to (2) is given by

$$R = \frac{\rho}{w} \frac{\ell}{b} = R_s \left( \frac{\ell}{b} \right) \quad (3-4)$$

where  $R_s$  is called the sheet resistivity. The ratio  $\frac{\ell}{b}$  is called the number of squares. The sheet resistivity thus has the dimensions of "ohms per square", denoted by  $\Omega/\square$ .

The resistivity of the film is finally given by

$$\rho = R_s \cdot w \quad (3-5)$$

provided  $w$  can be estimated. If  $w$  is indeterminable, then the measurements are expressed in terms of  $R_s$ .

### Sheet Conductivity

Sheet conductivity ( $\sigma_s$ ) is the reciprocal of sheet resistivity ( $R_s$ )

$$\sigma_s = \frac{1}{R_s}$$

and has dimensions of "Siemens square", denoted by  $S.\square$ .

#### 3.3.2 Measurement Techniques

The sheet conductivities of the pellet specimens were measured using a four point probe\* technique (58,59), the experimental arrangement for which is shown schematically in Figure 3-3.

---

\* A. M. Fell Ltd., New Haven, Sussex, England.

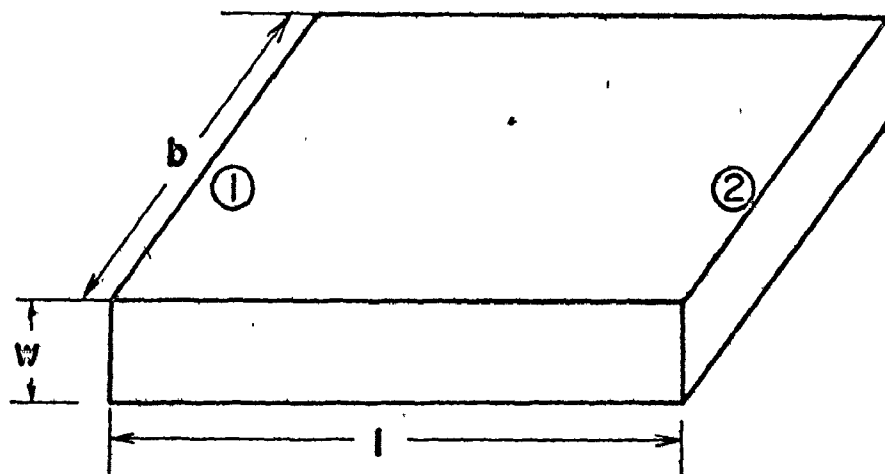


Fig. 3-2 Rectangularly shaped section of a thin film of thickness  $w$  and having the dimensions of length  $l$  and width  $b$ .

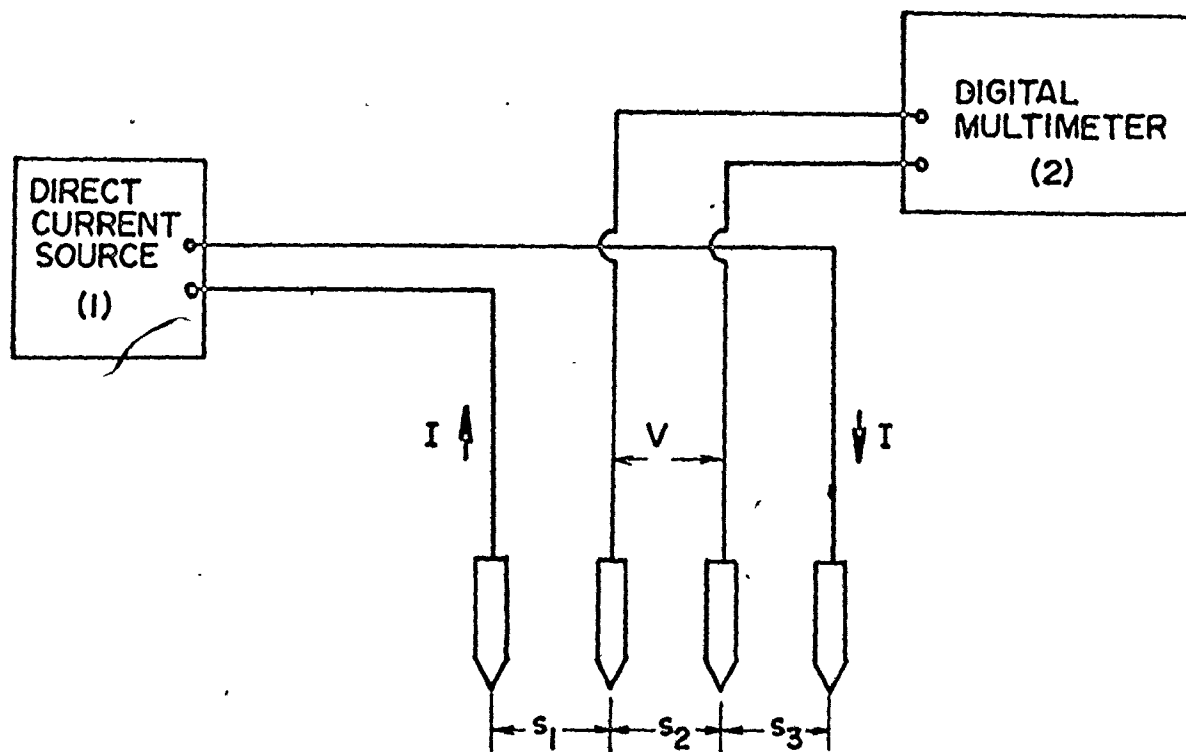


Fig. 3-3 Schematic of conductivity measurement technique.  $S_1$ ,  $S_2$ ,  $S_3$  are the inter probe spacings. (The experimental set up used in this work has  $S_1 = S_2 = S_3 = S = 1 \text{ mm}$ ).

- (1) Direct current source. Keithley Model 225.  
D.C. current:  $10^{-7} \text{ A}$  full range to  $10^{-1} \text{ A}$   
in seven decade ranges with 3 digit readout.  
Accuracy:  $\pm 0.5\%$  of reading;  $\pm 0.05\%$  of full  
range.
- (2) Digital multimeter. Keithley Model 160  
with a range of  $\pm 1 \mu\text{V}$  per digit to  $\pm 1000 \text{ V}$   
full scale.  
Accuracy:  $\pm 0.1\%$  of reading,  $\pm 1$  digit on  
all ranges.

The method consists of placing four probes that make contact along a line on the surface of the material. Current is passed through the outer pair of probes and the floating potential is measured across the inner pair.

Valdes (58) considers several specimen geometries in calculating the sheet resistivities of a sample. Two specific cases will be considered here as being appropriate to this study.

Case 1. Semi infinite volume of material

Consider a semi infinite volume of material as in Fig. 3.4. The conductivity  $\sigma$  is given by ohm's law, namely

$$J = \sigma E, \quad (3-6)$$

where  $J$  = the current density ( $A/cm^2$ ) and

$E$  = the electric field ( $V/cm$ ).

Consider a hemispherical surface of radius  $r$  centered on one of the current probes:

$$\text{Area} = 2\pi r^2$$

$$J = \frac{I}{2\pi r^2} \quad (3-7)$$

Let  $Q$  be the charge associated with a current probe due to current  $I$  so that the electric field at a distance  $r$  is given by

$$E = \frac{Q}{4\pi\epsilon_0 r^2}.$$

Hence we have

$$\sigma = \frac{J}{E} = \frac{2\epsilon_0 I}{Q} \quad (3-8)$$

The potential at a distance  $r$  due to a point charge  $Q$  is given by



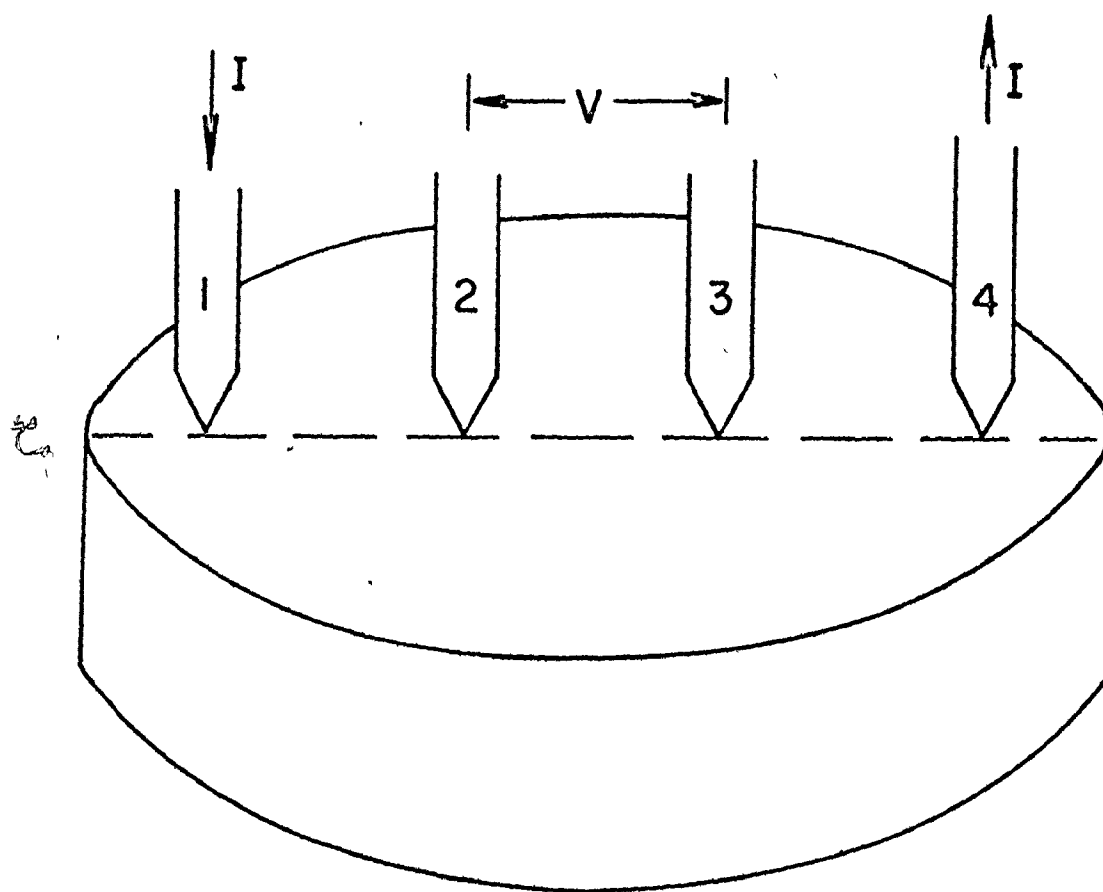


Fig. 3-4 Schematic of four point probe on a large sample (semi infinite volume of material, Case 1.)

$$V_f = \frac{Q}{4\pi\epsilon_0 r} ,$$

so that substituting the value of  $Q$  from eqn (3-8) we have

$$V_f = \frac{I}{2\pi\sigma} \frac{1}{r} \quad (3-9)$$

as the potential at a distance  $r$  from a probe carrying a current  $I$ .

The distances of interest here are the positions of the inner pair of probes across which the potential difference is measured. The potential at probe 2 due to current  $+I$  at Probe 1 and current  $-I$  at probe 4 is given, according to eq. (3.9), by

$$V_{f_2} = \frac{I}{2\pi\sigma} \left[ \frac{1}{s_1} - \frac{1}{s_2+s_3} \right].$$

The potential at probe 3 due to current  $+I$  at probe 1 and current  $-I$  at probe 4 is given by

$$V_{f_3} = \frac{I}{2\pi\sigma} \left[ \frac{1}{s_1+s_2} - \frac{1}{s_3} \right].$$

The potential difference between probes 2 and 3 is given by

$$V = V_{f_2} - V_{f_3}$$

which, for equal probe spacings, reduces to

$$V = \frac{I}{2\pi\sigma S} . \quad (3-10)$$

The conductivity of the material is thus given by

$$\sigma = \left( \frac{1}{2\pi S} \right) \left( \frac{I}{V} \right) . \quad (3-11)$$

The theory developed so far is applicable to a semi-infinite volume of material. For a sample with a finite thickness  $w$  a correction factor  $f(\frac{w}{S})$  can be introduced. The method of ob-

taining this factor is considered in the following section. Final results are tabulated by Uhlir (64) and reproduced here in Table 3.1.

The conductivity of a sample with a finite thickness  $w$  is given by

$$\sigma(w) = \frac{1}{2\pi S} \left(\frac{I}{V}\right) f\left(\frac{w}{S}\right). \quad (3-12)$$

Table 3-1

Conductivity measurement -  
Correction factor for finite thickness

$\frac{w}{S}$	$f\left(\frac{w}{S}\right)$
0.5	2.780
1.0	1.504
2.0	1.094
2.5	1.051
3.3	1.023
5.0	1.007
10.0	1.001

In the work reported here the pellets used were about 5 mm thick and with a probe spacing ( $S$ ) of 1 mm the conductivity of the specimen follows as

$$\sigma = \frac{1}{2\pi S} \left(\frac{I}{V}\right) (1.007).$$

This shows that eq. (3-11) can be used with an error of only 0.7%.

Case 2 A very thin layer  $w$  on a non-conducting substrate ( $w \ll S$ )

As will be evident from the experimental results on the conductivity changes in  $\text{Nb}_2\text{O}_5$  (Chap. 5) case 2 is valid for specimens for which the conductivity has been changed due to the

formation of an altered surface layer.

The solution is obtained by considering an infinite series of images along lines normal to the thin layer and passing through the current sources, as shown in Fig. 3-5. As before, the potential difference across the inner pair of probes is evaluated and a relationship for the conductivity is deduced. Following the treatment of Valdes (58) we have

$$\sigma = \frac{1}{2\pi S} \left(\frac{I}{V}\right) f\left(\frac{W}{S}\right)$$

where  $f\left(\frac{W}{S}\right)$  is given by

$$f\left(\frac{W}{S}\right) = 1 + 4 \frac{S}{W} \sum_{n=1}^{\infty} \left\{ \frac{1}{\sqrt{\left(\frac{S}{W}\right)^2 + (2n)^2}} - \frac{1}{\sqrt{2\left(\frac{S}{W}\right)^2 + (2n)^2}} \right\}. \quad (3-13)$$

The function  $f\left(\frac{W}{S}\right)$  is tabulated in Table 3-2 for small values of  $\frac{W}{S}$ . For  $\frac{W}{S}$  smaller than 0.5,  $f\left(\frac{W}{S}\right)$  is seen to be well represented by the limiting expression for an infinitely thin layer,

$$f\left(\frac{W}{S}\right) = \frac{2S}{W} \ln 2. \quad (3-14)$$

We thus get

$$\sigma = \frac{I}{\pi} \frac{\ln 2}{W}$$

$$\sigma_s = \sigma w = \frac{I \ln 2}{\pi V}. \quad (3-15)$$

In conclusion the sheet conductivity of a thin slice can be easily determined with a four point probe, by measuring the voltage  $v$  developed across the inner pair of probes due to a current

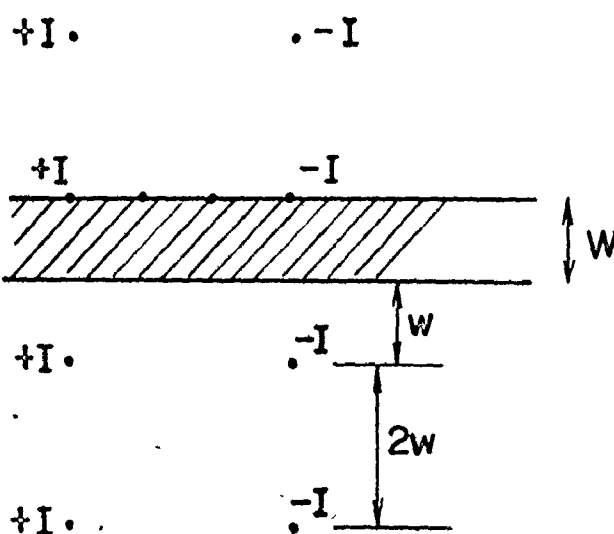


Fig. 3-5 Images for the case of the four point probes on a thin slice with a non-conducting substrate.

Table 3-2

Conductivity measurement -  
Correction factor for finite thickness

$\frac{w}{S}$	$f(\frac{w}{S})$ $\frac{2S}{w} \ln 2$	$\frac{2S}{w} \ln 2$
$<<0.1$		
0.100	13.863	13.86
0.141	9.704	9.83
0.200	6.931	6.93
0.333	4.159	4.16
0.500	2.780	2.77
1.000	1.504	1.39
1.414	1.223	0.98
2.000	1.094	0.69

I through the outer pair of probes. Conversion of the conductivity from sheet to bulk form is not necessarily as simple.

### 3.4 ELECTRON MICROSCOPY

#### 3.4.1 Introduction

The structural changes in thin films and pellets of  $\text{Nb}_2\text{O}_5$  induced by ion bombardment were studied with a Phillips EM-300 electron microscope. The observations on thin films and pellets were carried out in the transmission and reflection modes respectively. Detailed treatments of the theories and techniques in electron microscopy can be found in the books by Hirsch et al. (65), Heidenreich (66), Murr (67), Thomas (68) and Bunshah (69). A brief summary is provided here.

The instrument has a double condenser lens system in which the first condenser forms a demagnified image of the electron spot emerging from the gun. The second condenser lens transfers this spot to the specimen space where it focuses the spot either on, above or below the specimen depending on the requirements. The second condenser is used as the main control of intensity and size of the illuminated area. Maximum intensity is achieved when the spot is focused on the specimen while lower intensities are obtained by defocusing the second condenser. The final magnification of the image in the microscope is attained with the objective, intermediate and projector lenses. In general, the objective and projector lenses are operated at fixed focal lengths. The change in magnification is achieved by changing the current through the intermediate lenses.

### 3.4.2 Transmission Mode

A beam of electrons is incident on a thin specimen and a focused diffraction pattern is formed in the back focal plane of the objective lens. An aperture is located in the back focal plane which allows the final image to be formed with either the undiffracted beam resulting in a bright field image or one of the diffracted beams resulting in a dark field image. The contrast in a bright field image arises as a result of the depletion of electrons from the undeviated beam in areas which are diffracting strongly. In a dark field image, those areas of the specimen which are diffracting electrons into the beam used for image formation will appear bright. In the normal imaging or magnification mode of operation (Figure 3-6), the intermediate and projector lenses which follow the objective lens, are focused to transfer the first image formed by the objective lens on to the viewing screen at a high magnification. In the diffraction mode of operation (Figure 3-7), the intermediate lens is weakened to increase the focal length so that it is focused on the back focal plane of the objective lens rather than the first image plane. Agar (70) has outlined the procedure for obtaining a diffraction pattern from a selected area of the specimen. The selected area of the specimen is accurately focused in the plane of the aperture by focusing the aperture on the screen with the diffraction lens and then focusing the image on the screen with the objective lens.



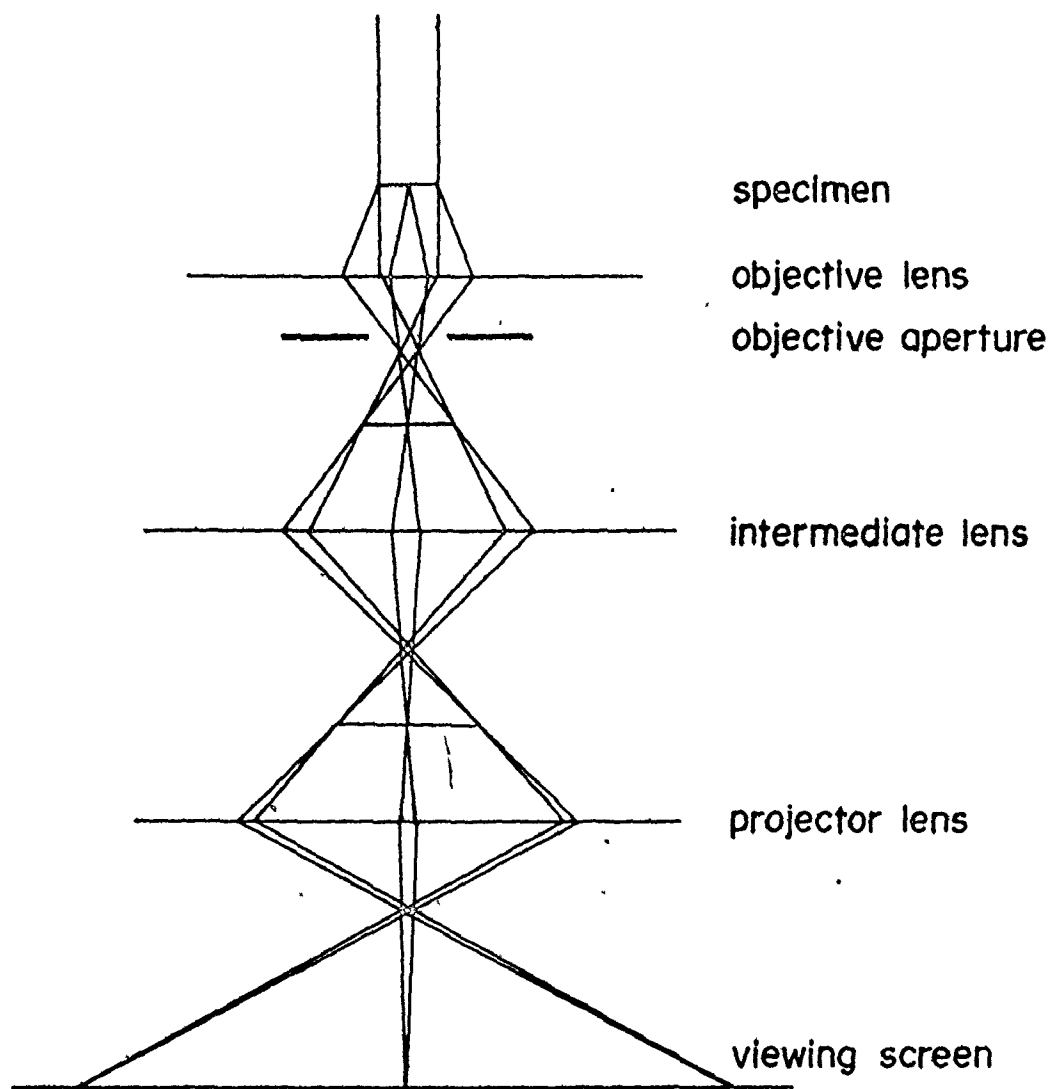


Fig. 3-6 Ray diagram showing the bright field mode of operation in the electron microscope.

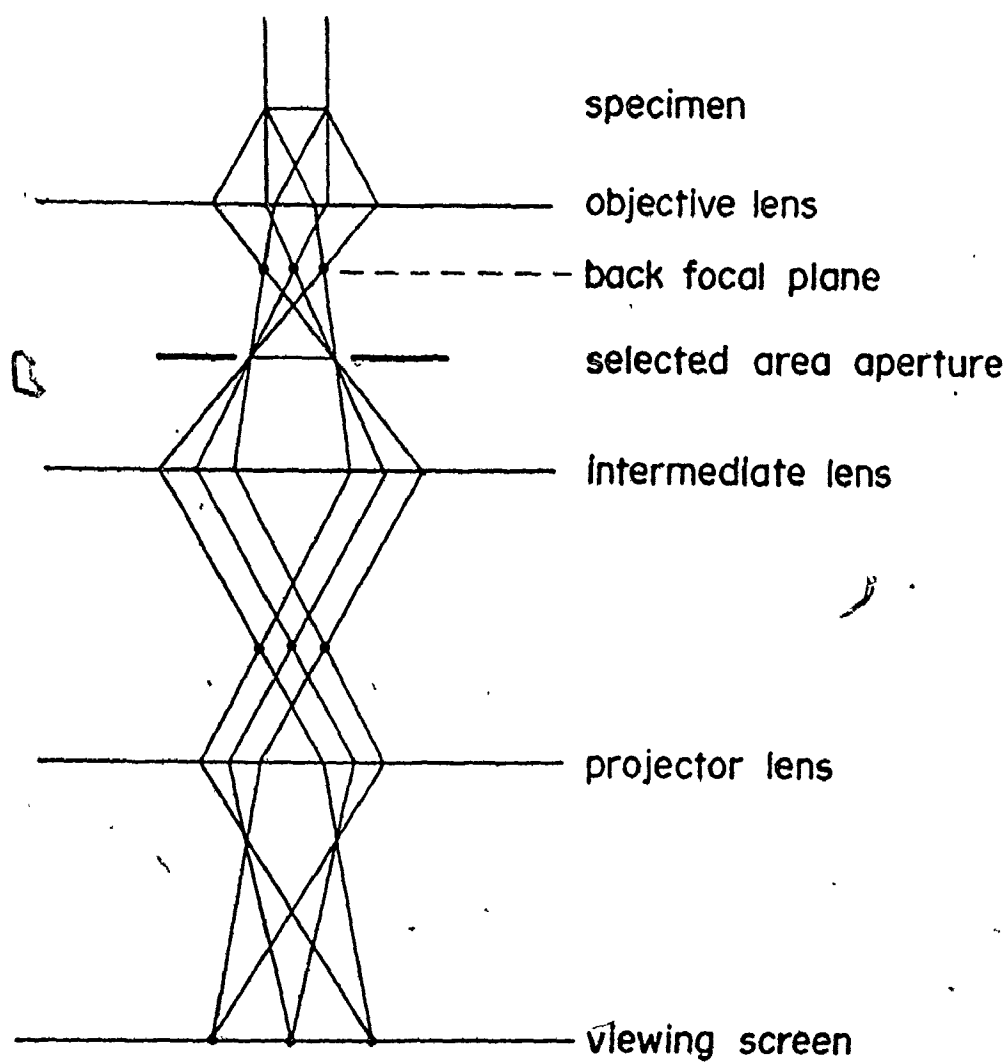


Fig. 3-7. Ray diagram showing the diffraction mode of operation in the electron microscope.

Dark field images from electrons which have been scattered by a specimen can be obtained by having the primary beam intercepted and some part of the scattered beam accepted by the objective lens aperture. In order to minimize the optical errors due to defects in the objective lens, the tilted gun technique is used where a particular reflection can be made to pass along the optic axis.

#### 3.4.3 Reflection Mode

When the microscope is operated with the appropriate attachments in the reflection mode, a diffraction pattern can be formed from the surface of a thick specimen. This technique is suited for obtaining the diffraction patterns from surfaces of specimens too thick to be used in the transmission mode, as in the case of  $\text{Nb}_2\text{O}_5$  pellets (5 mm thick) used in this study. This technique eliminates the need for extreme thinning of the specimens as is often required for examination in the transmission mode. The surface of the specimen is adjusted to be parallel to the beam and small adjustments are made in the angle of incidence until a sharp shadow line appears on the screen. Further adjustments are then made in the angle of incidence to bring the shadow line as close as possible to the undeviated beam in order not to lose small angle reflections. The surface of the specimen is then moved past the beam until a diffraction pattern is obtained.

An additional phenomena sometimes observed is due to the refraction of electrons. This is a consequence of the difference in wave length when the electron with a wave length  $\lambda$

enters a crystal with a mean inner potential  $V_0$ . The wave length inside the crystal  $\lambda'$  is slightly less than that in vacuum,  $\lambda$ . The Bragg condition inside the crystal is then

$$2d \sin \theta' = \lambda' \approx \lambda \left(1 + \frac{V_0}{2V_a}\right)^{-1}, \quad (3-16)$$

where  $\theta'$  is the Bragg angle inside the crystal and  $V_a$  is the accelerating potential. For electrons roughly normal to the entrance and exit surfaces, the effects of refraction are negligible. In reflection diffraction, the effects of refraction are manifest by small displacements or distortions of the diffraction spots. The amount of the displacements depends on the glancing angle and surface irregularities resulting in a broadening of all the displaced diffraction spots or rings.

In interpreting the results of electron diffraction by the reflection method it is desirable to know roughly the depth to which electrons can penetrate while retaining their power to form an interference pattern. This depends on the state of the surface as well as the material under study for a given accelerating voltage. Cochrane (71) estimated this depth for known thicknesses of Ni electrodeposited on copper substrates. It appears that using an accelerating voltage of 30 kV, the minimum thickness to yield a detectable diffraction pattern is about 1.0 nm, a 20 nm layer diffracts strongly and a 40 nm layer obliterates the effect of the substrate.

To obtain information applicable to the present study

of Nb. The specimens were examined in the reflection electron diffraction mode and the results are shown in Table 3-3. With 80 kV electrons, a layer of  $\text{Nb}_2\text{O}_5$  having a thickness of 25 nm obliterates the effect of the substrate.

#### 3.4.4 Analysis of Electron Diffraction Patterns

If we consider an electron diffraction camera with no lenses after the specimen, the position of a diffraction spot (for planes of spacing  $d$ ) on the photographic plate is given by

$$R = \frac{\lambda L}{d}, \quad (3-17)$$

where  $R$  is the distance from the central spot,  $\lambda$  is the electron wavelength, and  $L$  is the distance of the specimen from the plate. This is an approximate relationship based on the assumption of small scattering angles and follows from the reflecting sphere construction. Although the same expression is used with electron microscopes,  $L$  then represents an equivalent length which depends upon the lens magnifications. It is usual to refer to  $\lambda L$  as the camera constant of the microscope. The value of  $\lambda L$  has to be determined for each standard set of lens settings used and for each electron energy used.

To calibrate the camera constant  $\lambda L$  it is necessary to obtain a diffraction pattern from a standard substance such as gold and measure the diameter of the rings. To minimize the errors, the standard substance is placed in some adjacent region alongside the specimen of interest. The identity of the specimen can be either confirmed or determined as the case may be with the following procedure:

Table 3-3

Depth of penetration of electrons.  
Reflection electron diffraction  
using 80 kV electron beam

Thickness of anodic Nb <sub>2</sub> O <sub>5</sub> films (nm)	Nature of pattern
5	polycrystalline rings (Nb)
10	polycrystalline rings (Nb)
15	polycrystalline rings (Nb)
20	polycrystalline rings (Nb)
25	diffuse halos
40	diffuse halos

- 1) The diameters of the rings are measured.
- 2) These distances are converted into interplanar ( $d$ ) spacings using the camera constant  $\lambda L$ .
- 3) The arrangement of diffraction rings may indicate a certain recognizable crystal structure.
- 4) The set of  $d$  spacings obtained from the pattern are compared with those reported in the ASTM cards for the substances which are expected.

When using X-ray data in connection with electron diffraction patterns, it must be noted that the structure factor  $F$  is different for X-rays and electrons. Thus lines appearing in the X-ray pattern may not appear in the electron diffraction pattern and vice versa, due to the intensities being different.

The following factors contribute to the errors in the analysis of the diffraction patterns:

- 1) Fluctuations in the voltage supply.
- 2) Faulty lens settings.
- 3) Changes in specimen height.
- 4) Errors of measurement of ring diameters.
- 5) Refraction effects.

The instruments are designed to have voltage stabilization ratios of  $10^5:1$ , which reduces the fluctuations to a minimum. Phillips (72) states that variations in  $\lambda L$  of about 3% can arise from variations in objective lens current of about 1.5%. Changes

in specimen height can be minimized by having the standard and the specimen alongside on the same holder. The measurement of the diameters or radii of the diffraction rings is greatly facilitated by a comparator with a typical reproducibility of  $\pm 0.005$  cm, resulting in an uncertainty in calculated  $d$  values ranging from  $\pm 0.2$  to  $\pm 0.7\%$ . The major source of error usually is due to faulty lens settings. Taking the various sources of error into account an error up to about  $4\%$  can be expected in the determination of the  $d$  spacings.



## CHAPTER 4

### EXPERIMENTAL RESULTS: STRUCTURAL CHANGES

#### 4.1 INTRODUCTION

Electron microscope studies of ion bombarded Ge (17), Si (18) and GaAs (19) have shown that radiation damage is manifest in the creation of essentially amorphous regions with diameters of  $\sim 5$  nm. It is thought that these regions result from the disorder contained in the displacement cascade or cascades caused by each ion. As the bombardment dose builds up, the disordered zones steadily increase in number until eventually overlap occurs. At this stage the bombarded zones will have to all intents and purposes degenerated into a continuous amorphous layer. The depth below the surface at which overlap first occurs will depend on the spatial distribution of damage which can be calculated using the WSS theory (section 2.5). Overlap occurs at the peak of the distribution and will gradually spread to either side as the integrated dose builds up.

During bombardment of Si that part of the surface on which the ions impinge undergoes visible colour changes as the dose builds up (73). The particular colour depends on the ion species, the energy and the dose, with the colour finally saturating as a characteristic "milky white" appearance. The "milky" effect is made clearly visible by bombarding through a grid so as to provide a series of demarcation lines.

Recent studies of ion impact on oxides have given evidence for major structural changes. For example, bombardment at high doses leads to the crystallization of initially amorphous  $\text{ZrO}_2$  films, to the amorphization of  $\text{Al}_2\text{O}_3$  and to an increased conductivity with corresponding structural changes in  $\text{MoO}_3$ ,  $\text{V}_2\text{O}_5$  and  $\text{TiO}_2$ . These effects are reviewed in ref. (24). The present work deals with the ion bombardment of  $\text{Nb}_2\text{O}_5$  with a view to obtaining sufficient information to deduce a definite mechanism for whatever changes occur. The structural changes due to ion impact will be characterized with the techniques of electron microscopy, as it utilizes specimens having thicknesses comparable to the damage mean range for keV ions in oxides (typically about 10 nm to 100 nm). Low energy electron diffraction (LEED) sees only the outer surface and would thus be particularly vulnerable, amongst other things, to reactions with ambient oxygen; for example, it would fail to detect oxygen loss in those instances where the bombarded specimen was exposed to air and had its outer few atom layers restored to the initial stoichiometry. Also, LEED would overemphasize effects confined to the true outer surface. X-ray diffraction responds to a depth which is large with respect to the damage mean range and within which the damage would be a negligible component.

#### 4.2 STRUCTURE OF AMORPHOUS MATERIALS

The electron and X-ray diffraction patterns from an amorphous material consists of a number of very diffuse rings or halos, since the lack of significant structural periodicity

prevents the constructive reinforcement of scattered beams required to produce sharp diffraction spots. Stated in other terms, the diffuseness of the diffraction pattern implies a lack of long range structural periodicity while considerable short range order may or may not exist. The materials that are termed amorphous may have one of a variety of possible atomic arrangements. There are two limiting cases of such structures (74,75,76) which exhibit qualitatively similar diffraction patterns:

- (1) The continuous, random model, in which the postulated structure implies no crystal-like order beyond nearest neighbors. Even the nearest neighbor bonding is presumed to be somewhat distorted with respect to that occurring in the crystalline state.
- (2) The microcrystalline model, in which the postulated structure consists of crystallites of very small sizes.

Recently, Leung and Wright (76) presented an argument in support of the concept of a truly amorphous phase devoid of crystalline order as distinct from a microcrystalline array. This argument is based not only on experimental structure results but also on computer simulated models. They have constructed several models using a computer in which a starting nucleus of four atoms at the corners of a tetrahedron is allowed to grow by randomly generating sites round the nucleus in such a way that a new atom is placed in contact with three others already in the nucleus. The resulting growth is completely disordered with no evidence of any crystalline material.

The conventional technique of recording electron diffraction patterns by exposing photographic plates to the scattered beam has a disadvantage in that the plate records inelastically, as well as elastically, scattered electrons making it necessary to correct for the inelastic background. A few investigators (76 to 79) have utilized the direct recording of electron diffraction intensity from which the inelastically scattered electrons have been rejected by an electrostatic filter. The scattered electron beams are deflected to and fro across a very small aperture by a pair of magnetic coils situated beneath the specimen. Electrons entering the aperture pass through an electrostatic filter which rejects electrons that have lost more than a few volts in energy and the transmitted electrons are collected by a Faraday cup. As a result, only the elastically scattered electron intensity as a function of the scattering angle is recorded. Such studies in conjunction with the high resolution dark field techniques claim to better elucidate the structure of amorphous materials.

In the present study the diffraction patterns were recorded in the conventional way, i.e. without an electrostatic filter. The diffuse patterns are attributed to an amorphous material without further distinctions about the particular structural model.

#### 4.3 THIN FILMS OF Nb<sub>2</sub>O<sub>5</sub>

##### 4.3.1 Structure of as Prepared Films

The characteristics of anodically formed oxide films on the so-

nature of the films as they exist in intimate contact with the substrate metal. Vermilyea (80) used reflection electron diffraction to study the structure of anodic films on Ta and reported that only diffuse rings characteristic of an amorphous substance appeared in the patterns. Examination of the stripped films by transmission electron microscopy to characterize the films both as prepared and as subjected to thermal treatment has been carried out by several investigators (82 to 86). Lakhiani and Schreier (86) state that electron diffraction studies of anodic oxide films of Nb formed at various voltages at 25°C have shown that the oxide surface remains amorphous .

Thin sheets of Nb with a purity of 99.98% and with dimensions of 20×20×0.1 mm were anodized at 20 V and 5 mA/cm<sup>2</sup> in an electrolyte solution of 0.25% KF. The oxide thickness (X) formed at a voltage V is given by (87):

$$X = 2.90 + 2.96 \times V \quad \text{nm.} \quad (4-1)$$

Typical film thickness was 60 nm. The anodized sheets were then covered with parlodion, allowed to dry, and the resulting films peeled off removing with them the oxide films. The films were supported on 200 mesh microscope grids and the parlodion was dissolved by several washings with amyl acetate. The results obtained on examination of the films in the electron microscope are shown in Figure 4-1. The electron diffraction pattern consists of diffuse rings and as in previous studies is attributed to an amorphous material. For dark field microscopy

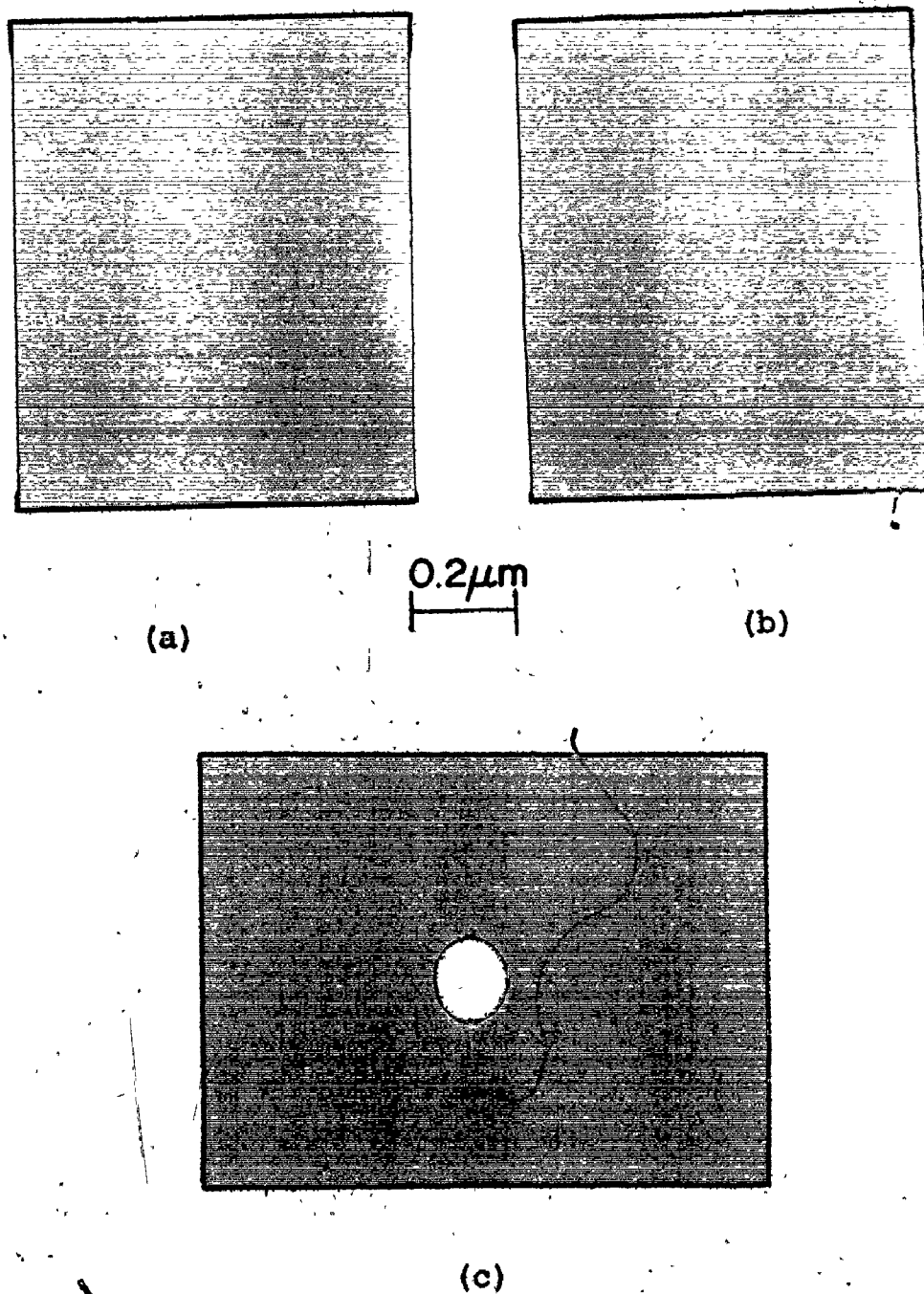
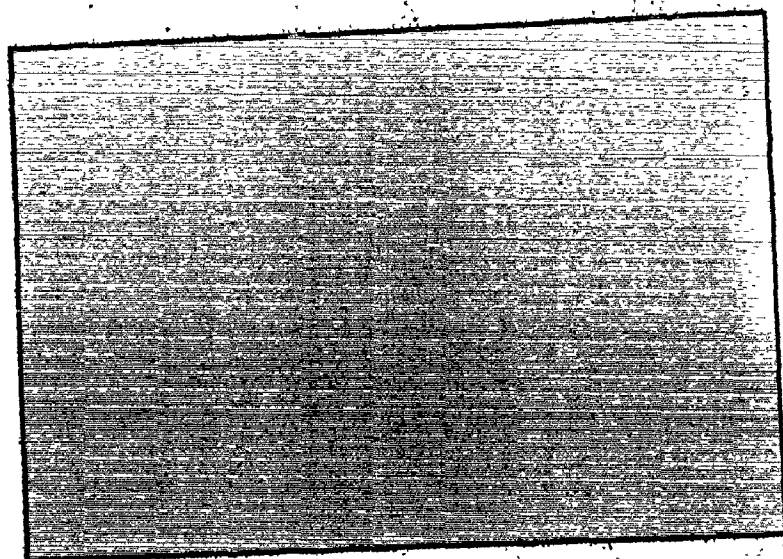


Figure 4-1. Transmission electron microscopy of as prepared anodic  $\text{Nb}_2\text{O}_5$  films: (a) bright field view, (b) dark field view, (c) diffraction pattern.

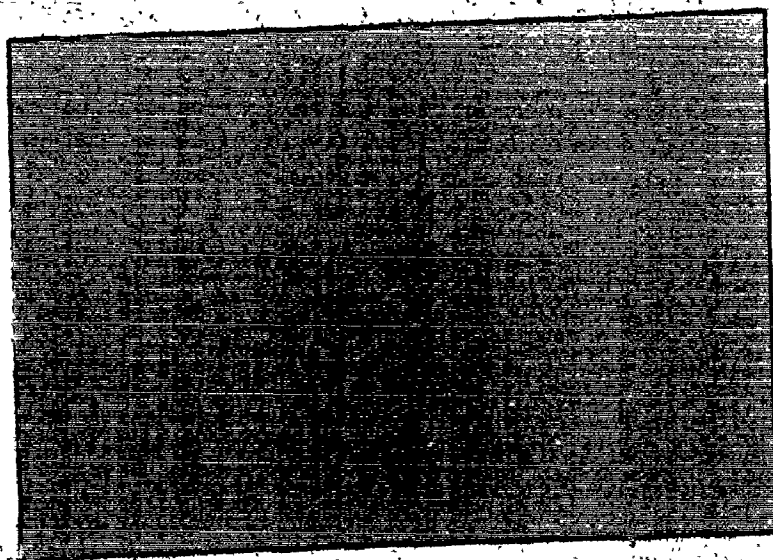
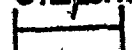
the electron beam was tilted until the strongest of the diffuse rings passed through the objective aperture on the electron optical axis of the microscope. The resulting dark field micrograph shown in Figure 4-1(b) does not reveal bright spots indicative of crystalline regions.

#### 4.3.2 Effect of Ion Dose

Thin films of  $\text{Nb}_2\text{O}_5$  supported on microscopic grids were bombarded with 35 keV  $\text{O}_2^+$  ions at currents of  $5 \mu\text{A}/\text{cm}^2$ . Bombardments were carried out at various doses ranging from  $5 \times 10^{14}$  ions/ $\text{cm}^2$  to  $1 \times 10^{17}$  ions/ $\text{cm}^2$ . After bombardment the films were examined in the electron microscope operating in the transmission mode. At doses of about  $5 \times 10^{15}$  ions/ $\text{cm}^2$ , the first observable crystallized regions were seen in the form of small regions having diameters of 5 to 15 nm. An area containing these regions in bright field is shown in Figure 4-2(a). This can be compared with a high resolution dark field view obtained from the strongest diffuse ring of the diffraction pattern. If the small regions observed in the bright field technique were crystallites, and if they were oriented so that they would diffract into the examined segment of the diffuse ring, then they would appear as small black specks on the dark field negative or white specks on the positive prints. This is observed, as shown in Figure 4.2(b). With increasing dose the crystallized regions increased in number and finally at a dose of  $5 \times 10^{16}$  ions/ $\text{cm}^2$  resulted in complete crystallization as shown in Figure 4-3. The corresponding electron diffraction pattern, Figure 4.3(c), consisted of polycrystalline to be that of  $\text{NbO}$  as indicated in



(a)

0.2  $\mu$ m  


(b)

Figure 4-2. Transmission electron microscopy of  $\text{Nb}_2\text{O}_5$  films which have been bombarded with 35 keV  $\text{O}_2^+$  to a dose of  $5 \times 10^{15}$  ions/cm<sup>2</sup>.



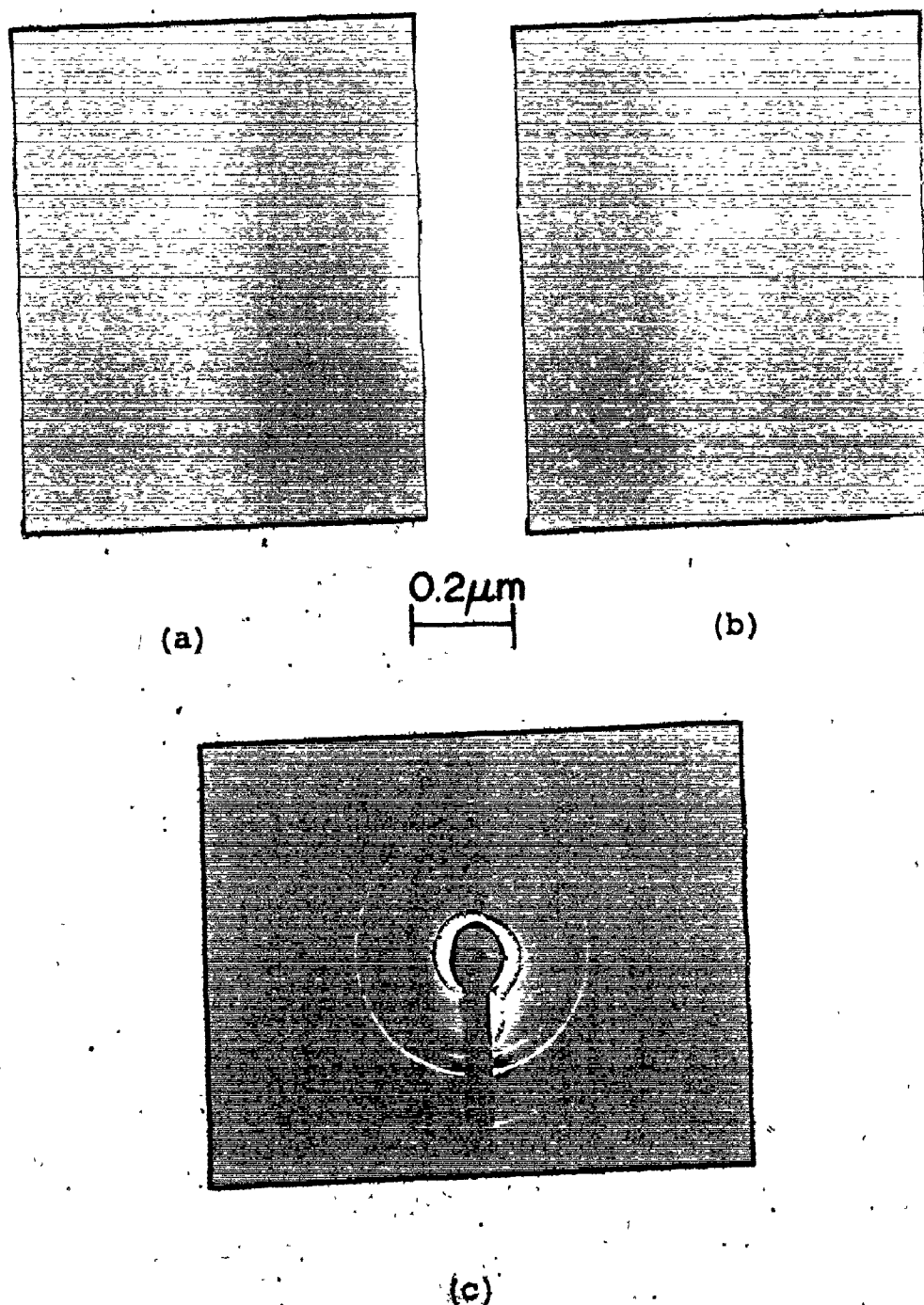


Figure 4-3. Transmission electron microscopy of  $\text{Nb}_2\text{O}_5$  films which have been bombarded with 35 keV  $\text{O}_2^+$  to a dose of  $5 \times 10^{16}$  ions/cm<sup>2</sup>: (a) bright field view, (b) dark field view and (c) diffraction pattern.

Table 4-1

Diffraction analysis of  $\text{Nb}_2\text{O}_5$  films following bombardment with  $5 \times 10^{16}$  ions/cm<sup>2</sup> of 35 keV oxygen

Bombarded $\text{Nb}_2\text{O}_5$	NbO ASTM 15-535
$d(\text{\AA})$	$d(\text{\AA})$
	4.16
	2.95
2.44	2.42
2.12	2.10
1.80	1.87
	1.71
1.48	1.48
	1.40
	1.33
1.28	1.27
1.22	1.21
	1.17
	1.12
1.06	1.05
	1.02
	0.99
0.96	0.97
0.94	0.94

A crystallized region of changed stoichiometry is basically a new type of defect and has apparently never been described before. It must therefore rank with the dislocation loop, the amorphous zone (17) and the crystalline zone (88) as a fundamental entity in the theory of radiation damage. It is with high likelihood not peculiar to  $\text{Nb}_2\text{O}_5$  alone, in view of the increasing evidence that most transition metal oxides and perhaps other compounds as well (halides, sulfides) undergo major stoichiometry changes when bombarded.

#### 4.4 SINTERED $\text{Nb}_2\text{O}_5$ PELLETS

In a further group of experiments, sintered  $\text{Nb}_2\text{O}_5$  pellets were bombarded with 35 keV oxygen ions at a current of  $6 \mu\text{A}/\text{cm}^2$  to various doses ranging from  $3 \times 10^{14}$  ions/ $\text{cm}^2$  to  $3 \times 10^{17}$  ions/ $\text{cm}^2$ . In a trivial sense such experiments with pellets serve to determine if the ion bombardment effects in thin films can also be initiated in the bulk (the effects of beam heating are reduced in the bulk). More important, however, the use of pellets facilitates the monitoring of conductivity changes induced by ion bombardment as discussed in Chapter 5.

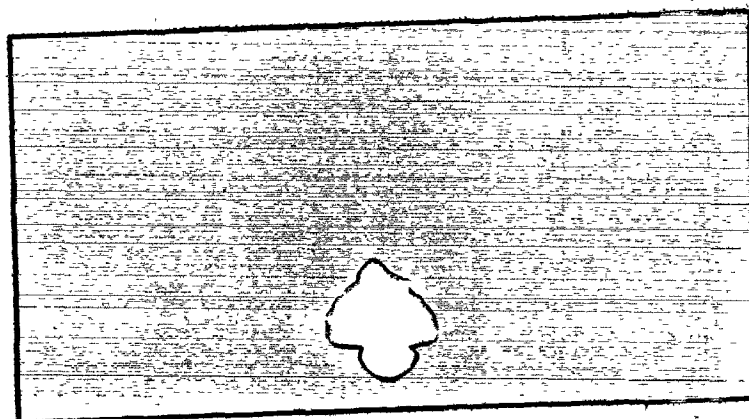
On visual examination the bombarded pellets showed gradual colour changes ranging from white at very low doses to black at the highest doses. Darkening was complete at a dose of about  $3 \times 10^{17}$  ions/ $\text{cm}^2$ . The bombarded pellets were examined using the reflection electron diffraction technique and exhibited

- (i) The crystalline pattern of the as prepared pellets, Figure 4-4(a), was gradually replaced by diffuse halos, Figure 4-4(b), up to  $5 \times 10^{15}$  ions/cm<sup>2</sup>.
- (ii) Increasing the dose further resulted in a ring pattern as shown in Figure 4-4(c) at a dose of  $2 \times 10^{17}$  ions/cm<sup>2</sup>. An analysis of the diffraction pattern leads to the altered layer being identified as NbO as indicated in Table 4-2.

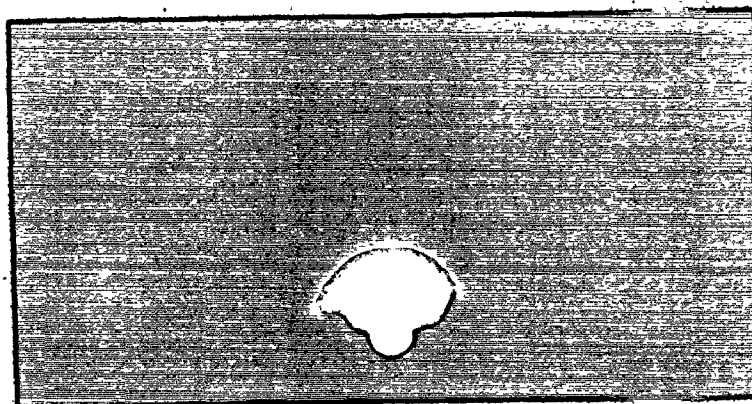
#### 4.5 SUMMARY

The structural changes induced by ion bombardment have been studied using electron microscopy. It has been shown that ion bombardment of Nb<sub>2</sub>O<sub>5</sub> leads initially to an altered layer which is amorphous at low doses and finally has the stoichiometry NbO at high doses. This has been observed in thin films using the transmission mode and in sintered pellets using the reflection mode.

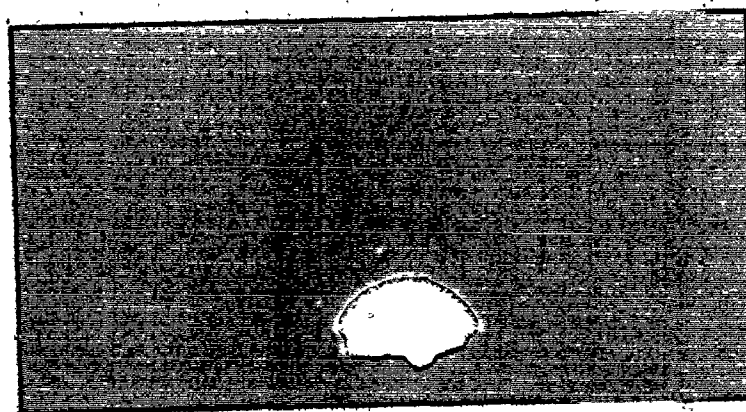
A comparison with other studies indicates that ion bombardment of Si and Ge leads to the formation of amorphous regions with dimensions of  $\sim 5$  nm which finally impinge to form an amorphous layer. Bombardment of MoO<sub>3</sub>, V<sub>2</sub>O<sub>5</sub> and TiO<sub>2</sub> is known to lead to an initial amorphization followed by the formation of lower oxides. These studies were confined to pellets, however, and were unable to establish the details of the formation of the lower oxides. The present study using thin films of Nb<sub>2</sub>O<sub>5</sub> indicates for the first time that the oxygen loss occurs by virtue of the formation of crystalline regions of NbO having dimensions similar to the amorphous regions found with Si and Ge and the crystalline regions



(a)



(b)



(c)

Figure 4-4. Reflection electron diffraction patterns taken of sintered  $\text{Nb}_2\text{O}_5$  pellets under the following conditions: (a) before bombardment, (b) after bombardment with  $4 \times 10^{15}$  ions/cm<sup>2</sup> of 35 keV  $\text{O}_2^+$ , (c) after bombardment with  $2 \times 10^{17}$  ions/cm<sup>2</sup> of 35 keV  $\text{O}_2^+$ .

Table 4-2

Diffraction analysis of  $\text{Nb}_2\text{O}_5$  pellets following bombardment with  $2 \times 10^{17}$  ions/cm<sup>2</sup> of 35 keV oxygen

Bombarded $\text{Nb}_2\text{O}_5$	NbO ASTM 15-535
$d(\text{\AA})$	$d(\text{\AA})$
	4.16
	2.95
2.40	2.42
2.07	2.10
1.84	1.87
1.72	1.71
1.48	1.48
	1.40
	1.33
1.26	1.27
1.22	1.21
	1.17
1.11	1.12
1.04	1.05
	1.02
0.98	0.99
	0.97
0.95	0.94

formed with  $\text{ZrO}_2$ . We regard the present results, however, as demonstrating the existence of a basically new type of defect. With increasing dose the regions of lower stoichiometry increase in number until complete impingement, thence crystallization occurs by about  $5 \times 10^{16}$  ions/cm<sup>2</sup>. These results with  $\text{Nb}_2\text{O}_5$  are evidently not due to beam heating of thin films, as the basic feature (the formation of  $\text{NbO}$ ) occurs also with pellets.

The electrical properties of transition metal oxides reveal interesting features. In particular, ~~high valence oxides~~ like  $\text{V}_2\text{O}_5$ ,  $\text{Nb}_2\text{O}_5$  and  $\text{WO}_3$  are insulating while nonstoichiometric as well as low-valence oxides exhibit semiconducting or metallic properties. Hence, another approach to studying the bombardment induced changes in  $\text{Nb}_2\text{O}_5$  is by monitoring the electrical conductivity due to bombardment. This is discussed in Chapter 5, to follow.

## CHAPTER 5

### EXPERIMENTAL RESULTS: CONDUCTIVITY CHANGES

#### 5.1 EFFECT OF ION DOSE

$\text{Nb}_2\text{O}_5$  pellets which were bombarded with 35 keV oxygen ions showed a gradual colour change from white to black with darkening complete at a dose of about  $3 \times 10^{17}$  ions/cm<sup>2</sup>. Similarly, pellets bombarded with 35 keV Kr ions also exhibited darkening of the surface which was complete at about  $1 \times 10^{17}$  ions/cm<sup>2</sup> and thus at a rather lower dose. This type of colour change has previously been observed for  $\text{V}_2\text{O}_5$  and  $\text{MoO}_3$  (28) and subsequently for  $\text{TiO}_2$  (32).

In addition to colour changes bombarded pellets showed increases in sheet conductivity with increasing ion dose. This is illustrated in Figure 5-1. The conductivity measurements were obtained with a four point probe (Sect. 3.3.2). Values of current (I) and voltage (V) were transformed to bulk ( $\sigma$ ) or sheet ( $\sigma_s$ ) conductivity by using the following expressions:

$$\sigma = \frac{I}{2\pi SV} \quad (\text{semi-infinite medium}) \quad (5-1)$$

$$\sigma_s = \sigma w = \left(\frac{I}{\pi V}\right) \ln 2 \quad (\text{layer of thickness } w). \quad (5-2)$$

Each separate value of the sheet conductivity represents an average of 24 measurements, which include 4 values of the probe current, both polarities, and 3 positions on the sample. The



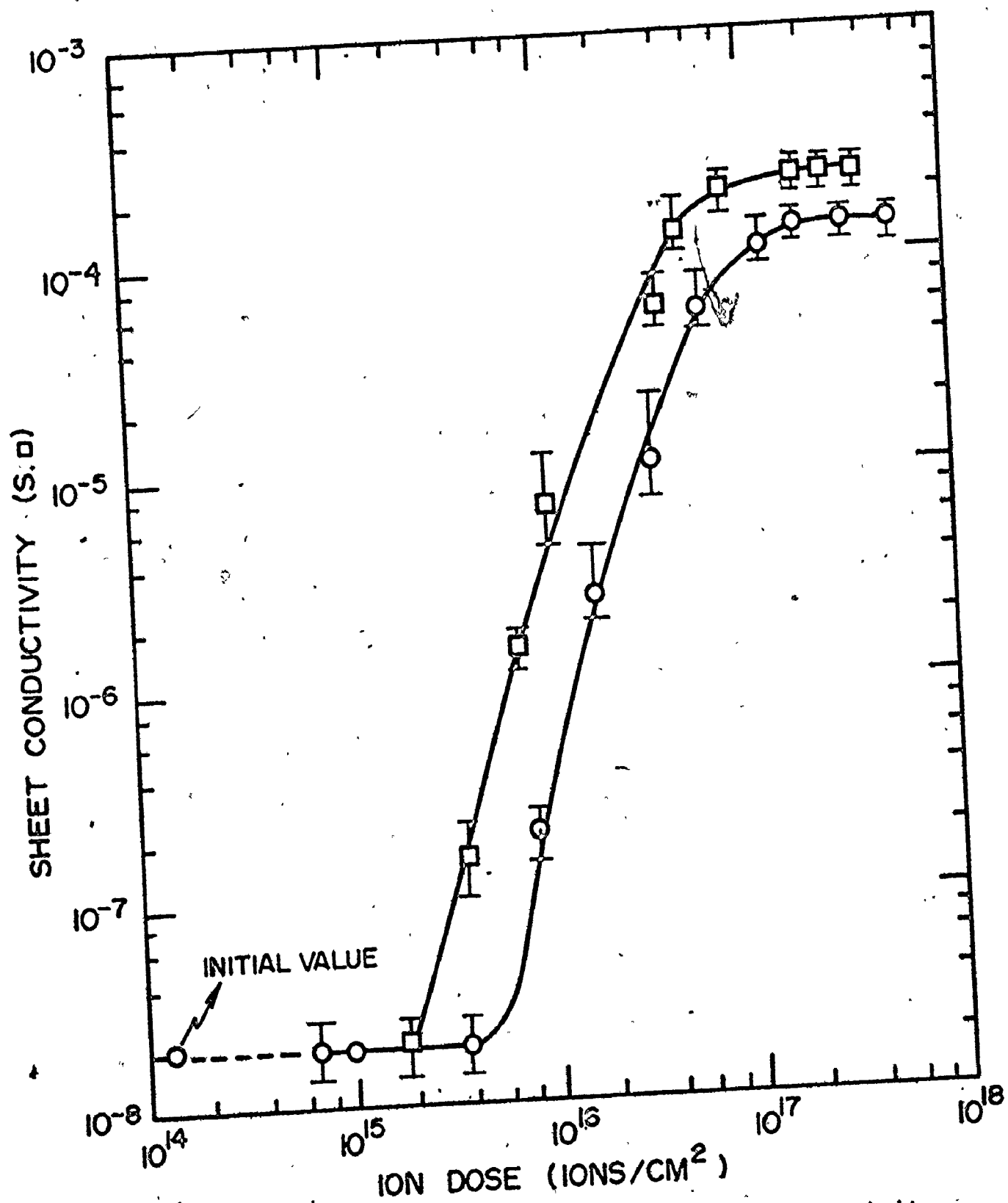


Fig. 5-1 Effect of ion dose on the sheet conductivity of  $\text{Nb}_2\text{O}_5$  pellets bombarded with 35 keV  $\text{Kr}^+$  ( $\square$ ) and  $\text{O}_2^+$  ( $\circ$ ) ions.

error bars represent extremes.

In the region of low ion dose ( $\leq 2 \times 10^{15}$  ions/cm<sup>2</sup>) the conductivity is comparable to that for unbombarded Nb<sub>2</sub>O<sub>5</sub>. The indicated values of  $\sigma_s$  ( $2 \times 10^{-8}$  S.□) as deduced with eqn. (5-2) are then more correctly expressed as bulk conductivities ( $1.5 \times 10^{-7}$  S/cm using eqn. 5-1). Beyond a threshold dose of about  $4 \times 10^{15}$  ions/cm<sup>2</sup>, however,  $\sigma_s$  increases rapidly and can then be regarded as a true sheet conductivity. The increase in  $\sigma_s$  attains a saturation level of  $1 \times 10^{-4}$  S.□ for incident O<sub>2</sub><sup>+</sup> and  $2 \times 10^{-4}$  S.□ for incident Kr<sup>+</sup>. The doses for half saturation are  $8 \times 10^{16}$  ions/cm<sup>2</sup> for O<sub>2</sub><sup>+</sup> oxygen and  $4 \times 10^{16}$  ions/cm<sup>2</sup> for Kr<sup>+</sup>.

## 5.2 EFFECT OF ION ENERGY

The results presented in Sect. 5.1 indicate that oxygen is almost as effective as Kr for inducing conductivity changes when the ion energy is 35 keV. To obtain more details about the bombardment induced changes in Nb<sub>2</sub>O<sub>5</sub>, pellets were bombarded with Kr and oxygen ions of various energies at a constant dose of  $2 \times 10^{17}$  ions/cm<sup>2</sup>. The resulting sheet conductivity changes are illustrated in Figure 5-2 with the following points evident.

- a) At high energies (30 keV or greater) both Kr and oxygen bombardment lead towards a saturation of sheet conductivity. This suggests a correlation (though not a very good one) with the nuclear stopping power, which, in the Thomas-Fermi approximation, maximizes for  $\epsilon = 0.35$ , (Section 2.3), i.e. 87 keV for Kr<sup>+</sup> and 14 keV for O<sub>2</sub><sup>+</sup> ("ε" is Lindhard's reduced energy parameter

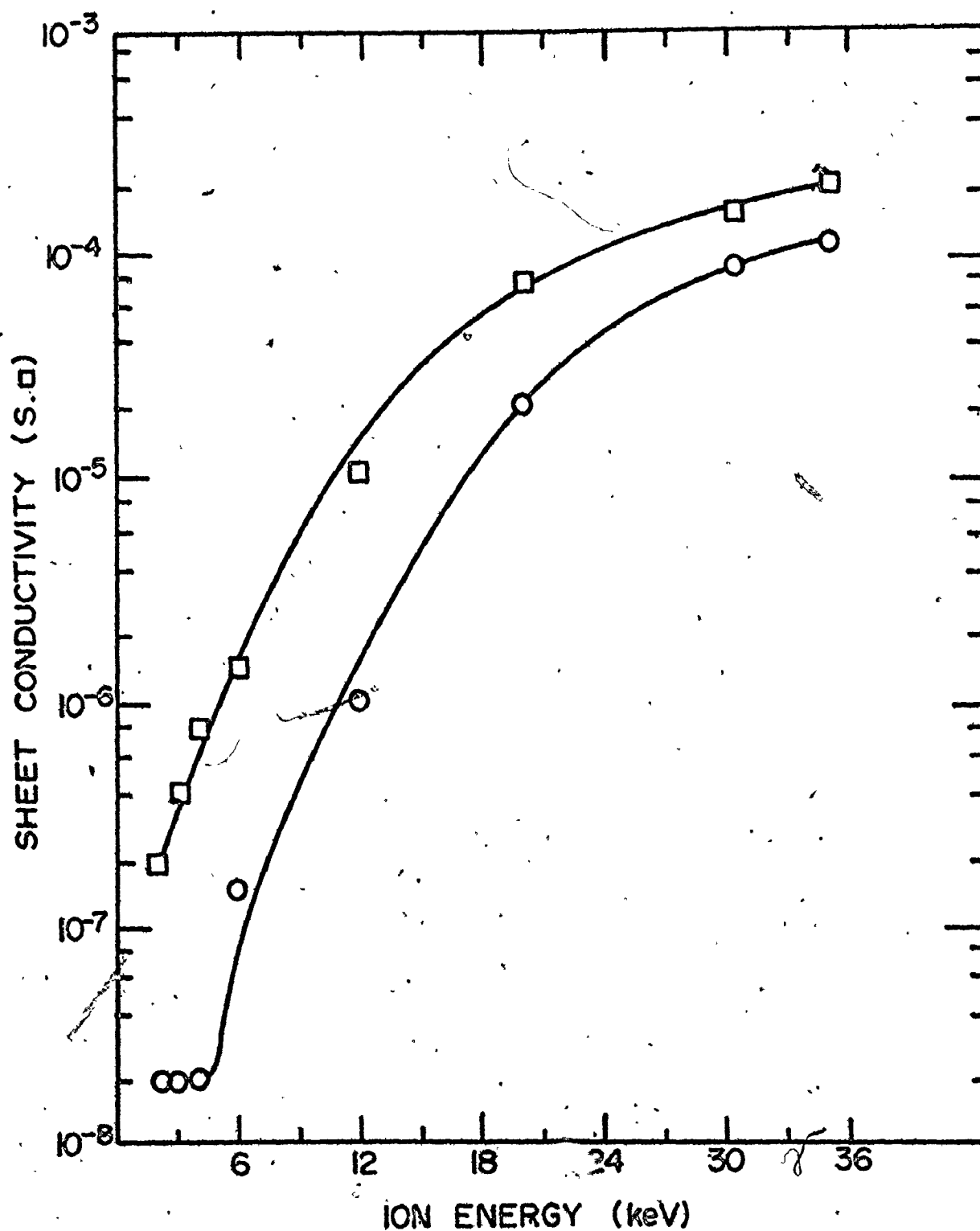


Fig. 5-2 Effect of ion energy on the sheet conductivity of Nb<sub>2</sub>O<sub>5</sub> pellets bombarded with Kr<sup>+</sup> (□) and O<sub>2</sub><sup>+</sup> (○) ions.

- (b) Oxygen bombardment shows well defined threshold effects at about 5 keV whereas Kr bombardment reveals sheet conductivity changes even at energies as low as 2 keV. The nature of the Kr curve is such that a threshold is unlikely at lower energies.

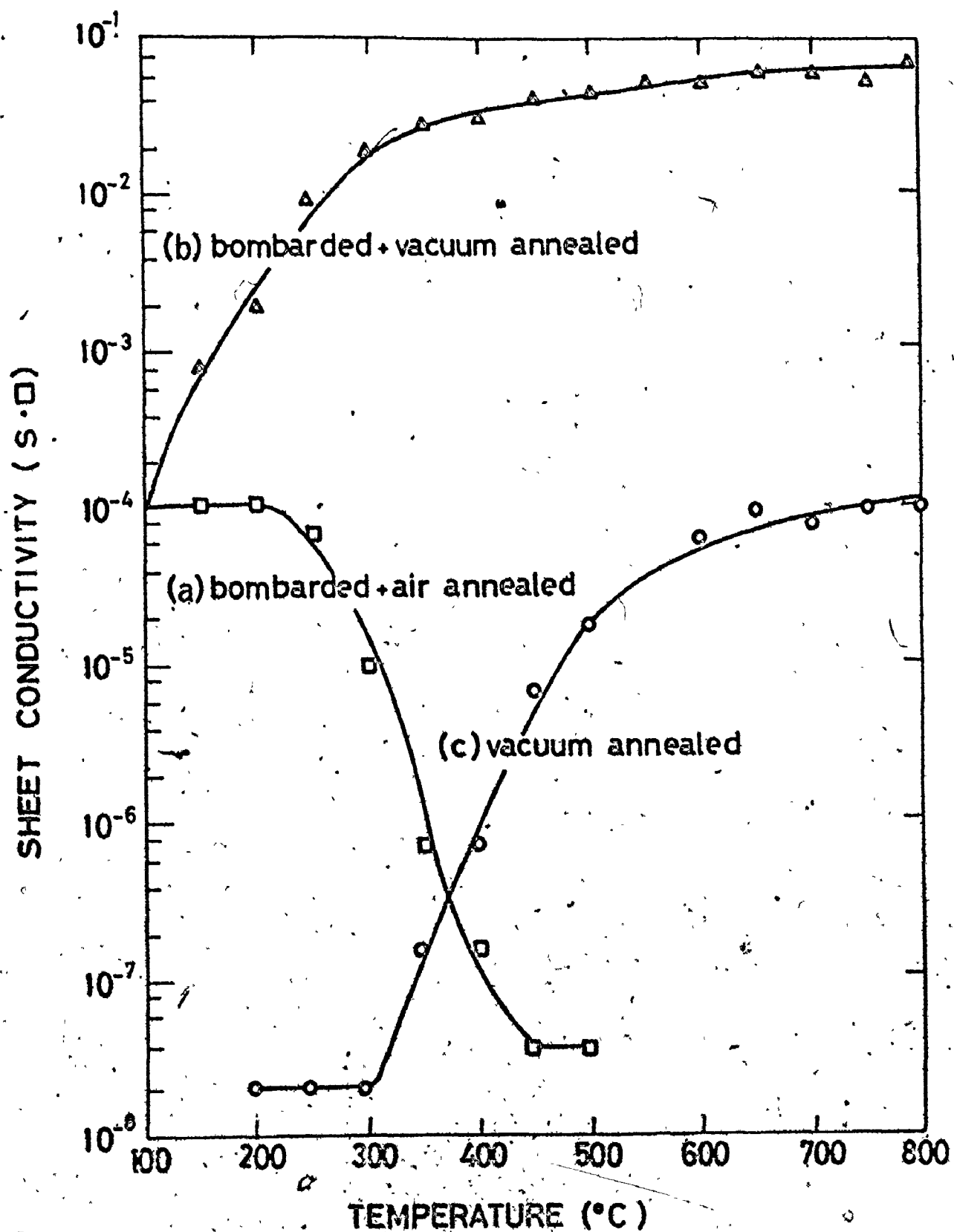
An energy threshold for sheet conductivity changes as caused by an oxygen beam can be explained on the basis of the distribution of oxygen due to such a bombardment and correlated with the sputtering coefficient (a variation in energy is equivalent to a variation in sputtering coefficient). Details of such a model are presented in Chapter 7, section 7.3.

### 5.3 ANNEALING OF CONDUCTIVITY

Pellets of  $\text{Nb}_2\text{O}_5$  bombarded with 35 keV oxygen to a dose in the saturation region ( $2 \times 10^{17}$  ions/cm<sup>2</sup>) were annealed isochronally by heating in steps of 50°C for 30 min in air. After each increment, the sheet conductivity was measured with the four point probe. The resulting behaviour is illustrated in Figure 5-3, curve (a), with the following characteristics.

- 1) Up to 200°C there is no change either in the sheet conductivity or in the colour of the pellets. This implies that the surface layer is stable up to this temperature.
- 2) Above 200°C there is a rapid decrease in sheet conductivity such that by about 450°C the conductivity has almost returned to the value expected for  $\text{Nb}_2\text{O}_5$ . The colouration of the pellet changes through various shades of grey becoming, finally,

Fig. 5-3 Effect of air (a) and vacuum (b) annealings on the sheet conductivity of bombarded  $\text{Nb}_2\text{O}_5$  pellets. The pellets were bombarded with 35 keV  $\text{O}_2^+$  ions to a dose of  $2 \times 10^{17}$  ions/cm<sup>2</sup>. Also shown is the effect of vacuum annealing on unbombarded pellets of  $\text{Nb}_2\text{O}_5$ .



Annealing behaviour was also studied by heating bombarded pellets ( $2 \times 10^{17}$  ions/cm<sup>2</sup> of 35 keV O<sub>2</sub><sup>+</sup>) in vacuum ( $\sim 1 \times 10^{-4}$  Pa) in steps of 50°C from 100°C to 800°C. As before, the sheet conductivity was measured after each increment and the results are depicted by curve (b) of Figure 5-3. The sheet conductivity increased by a factor of 600 and the pellets retained their black colouration. Examination of the surface in the reflection electron diffraction mode revealed diffraction patterns which could be identified as due to NbO. This is regarded as a particularly important result; it was sought, for example, in previous work on TiO<sub>2</sub> but the relevant experiments failed (91).

Finally the conductivity changes due to heating an unbombarded pellet in vacuum were determined (curve (c) of Figure 5-3). The increase in conductivity to  $10^{-3}$  S.□ is probably due to a slight loss of oxygen since non stoichiometric Nb<sub>2</sub>O<sub>5</sub> is an n-type semiconductor due to the formation of oxygen vacancies (60,61,62, 89,90).

Bombarded pellets showed no change in conductivity when stored in air at room temperature for about 600 days, similar to TiO<sub>2</sub> (91). The bombardment induced conductivity increase as observed in the present study is thus of a permanent nature as compared to transient changes found by Griffiths (92) for Al<sub>2</sub>O<sub>3</sub> and MgO.

#### 5.4 EFFECT OF ION CURRENT

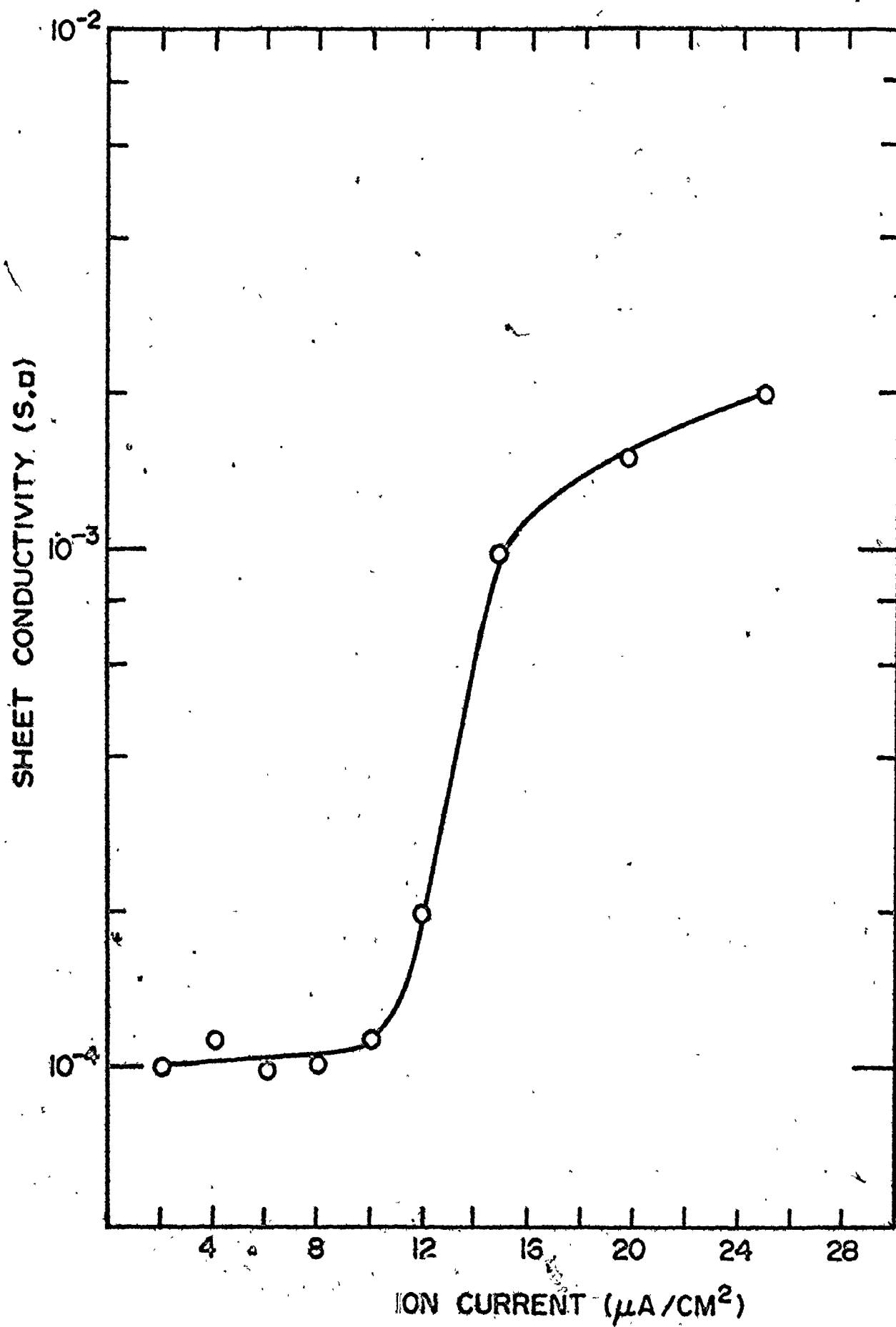
Nb<sub>2</sub>O<sub>5</sub> pellets were bombarded with 35 keV oxygen at various ion currents ranging from 2 to 25  $\mu$ A/cm<sup>2</sup>. The bombardment

$2 \times 10^{17}$  ions/cm<sup>2</sup> in each case. The effect of ion current density on the sheet conductivity is illustrated in Figure 5-4, with the following points evident:

- a) In the low current density region ( $< 10 \mu\text{A}/\text{cm}^2$ ) the conductivity is a constant, independent of the current.
- b) In the medium current density region (10 to  $15 \mu\text{A}/\text{cm}^2$ ) there is a sharp increase in conductivity due probably to beam heating.
- c) In the high current density region ( $> 15 \mu\text{A}/\text{cm}^2$ ) there may possibly be an approach to saturation.

These results show that the conductivity induced in  $\text{Nb}_2\text{O}_5$  by ion bombardment is independent of current for sufficiently low current densities. This will be shown to play a fundamental role in deducing a mechanism for the conductivity increase and stoichiometry changes (Chapter 7). If high current densities are considered to result in heating of the target, then these results can be correlated with the results of the annealing of conductivity. For example, with an ion current density of  $25 \mu\text{A}/\text{cm}^2$ , the sheet conductivity of the altered layer is  $2 \times 10^{-3} \text{ S.}\square$  which is similar to that obtained by heating to  $200^\circ\text{C}$  in vacuum (curve (b) of Figure 5-3). Similar results have been obtained with  $\text{TiO}_2$  (91) in which the conductivity changes due to ion current density could be correlated with changes induced by explicit changes in the target temperature during bombardment.





## 5.5 SUMMARY AND CONCLUSIONS

The impact of both  $Kr^+$  and  $O_2^+$  ions at 35 keV and high doses on  $Nb_2O_5$  leads to an increase in the sheet conductivity by a factor of  $5 \times 10^3$ . This correlates fully with the concurrent formation of a surface layer of NbO (Chapter 4), since NbO is known to exhibit metallic conductivity (93,94,95). At this point one could consider the preferential sputtering of oxygen as a possible mechanism to explain the oxygen loss leading to the conductivity and stoichiometric changes. Since the sputtering coefficient is dependent on the nuclear stopping power, therefore on the ion energy, the conductivity changes could be investigated further by varying the ion energy. The results indicate the existence of an energy threshold for conductivity changes when caused by an oxygen beam. A model based on sputter equilibrium, with additional features describing the oxygen concentration in units which indicate the stoichiometry (Chapter 7, section 7.3), predicts a conductivity increase for oxygen bombardment only when the sputtering coefficient is greater than a critical value.

The next group of experiments was carried out to determine the stability of the induced conductivity exposed to different conditions. Bombarded pellets showed no change in conductivity when stored in air at room temperature for about 600 days, similar to  $TiO_2$  (91). On heating in air, the conductivity is stable up to 200°C but with further heating decreases to the initial un-bombarded value at about 450°C. Air exposure of NbO layers may be to result in reoxidation to  $Nb_2O_5$  provided the tempera-

ture is sufficiently high. On heating bombarded pellets in vacuum the conductivity increases by a factor of about 600, probably due to the annealing of crystal imperfections. On heating unbombarded  $\text{Nb}_2\text{O}_5$  pellets in vacuum the conductivity increases, probably due to a slight loss of oxygen, consistent with non stoichiometric  $\text{Nb}_2\text{O}_5$  being an n-type semiconductor (88,89,90). The role of the beam current in inducing conductivity changes was studied and the results indicate that the conductivity is independent of current for 2 to  $10 \mu\text{A}/\text{cm}^2$ , i.e. at currents low enough that there is no beam heating, but increases by a factor of 20 for higher currents. By considering that high currents lead to beam heating, the observed increase in conductivity by a factor of 20 can be understood in terms of a temperature increase of  $200^\circ\text{C}$  (curve (b), Figure 5-3).

The results based on the structural examination and conductivity measurements on bombarded  $\text{Nb}_2\text{O}_5$  pellets indicate the formation of an altered surface layer of  $\text{NbO}$ . The question of the thickness of such an altered layer has been left unanswered. An answer can be sought by studying the dissolution behaviour of the altered layer and this is treated in the following chapter.

## CHAPTER 6

### EXPERIMENTAL RESULTS: THICKNESS OF ALTERED LAYER

#### 6.1 INTRODUCTION

Incident ions with an energy in the keV region produce as a result of collisions with lattice atoms various types of damage in the surface layer of the solid. The surface layer which is disordered or otherwise altered by ion bombardment in turn exhibits certain changes in the physical and chemical properties. One of the general properties of the solid which seems to be thus modified is the chemical reactivity, for example the rate of dissolution. Dissolution experiments performed with a radioactive ion labelled target are often valuable in estimating the depth of alteration induced by ion bombardment (96,97).

Ion bombardment of  $\text{Nb}_2\text{O}_5$  has been shown in Chapters 4 and 5 to lead initially to an amorphous phase and finally to  $\text{NbO}$  on the surface and the thickness of the altered layer needs to be estimated. If a suitable solvent is chosen which dissolves the altered layer at a much faster rate than the substrate, the overall dissolution of the specimen will effectively stop when the substrate is reached.

#### 6.2 THICKNESS OF ALTERED LAYER AT LOW TO MEDIUM DOSES.

$\text{Nb}_2\text{O}_5$  pellets were bombarded with 35 keV  $^{85}\text{Kr}$  (radioactive) to various doses. The amount of radioactivity in the pellets was

then measured, using a GM counting system, as a function of the time of exposure to various solvents. The retained activity was expressed as a fraction of the activity of the bombarded pellet before exposure to the solvent.

The fractional retained activity as a function of the time of exposure to fluoboric acid saturated with ammonium chloride is illustrated in Figure 6-1. It can be seen that the dissolution is slow and does not result in a sharp discontinuity. The results obtained using a solvent, the so called P-etch for  $\text{SiO}_2$  (98), which has a composition of

15 cm<sup>3</sup> 48% hydrofluoric acid  
 10 cm<sup>3</sup> 70% nitric acid  
 50 cm<sup>3</sup> water

are depicted in Figure 6-2. The dissolution of the bombarded pellets in this case can be safely assumed to exhibit an enhanced solubility of the altered surface with a sharp discontinuity.

By matching the activities at the discontinuities in the dissolution curves of Figure 6-2 with the corresponding activities in an integral ion distribution, it becomes possible to estimate the depths of the altered surface as a function of the dose. The integral concentration profile for 35 keV  $^{85}\text{Kr}$  ions incident on  $\text{Nb}_2\text{O}_5$  has been deduced from the Gaussian approximation to the distribution function (Section 2.6):

$$C^{\text{int}}(x) = \frac{1}{2} \operatorname{erfc} \left[ \frac{(x - \langle x \rangle)}{(2\mu_2)^{1/2}} \right] \quad (6-1)$$

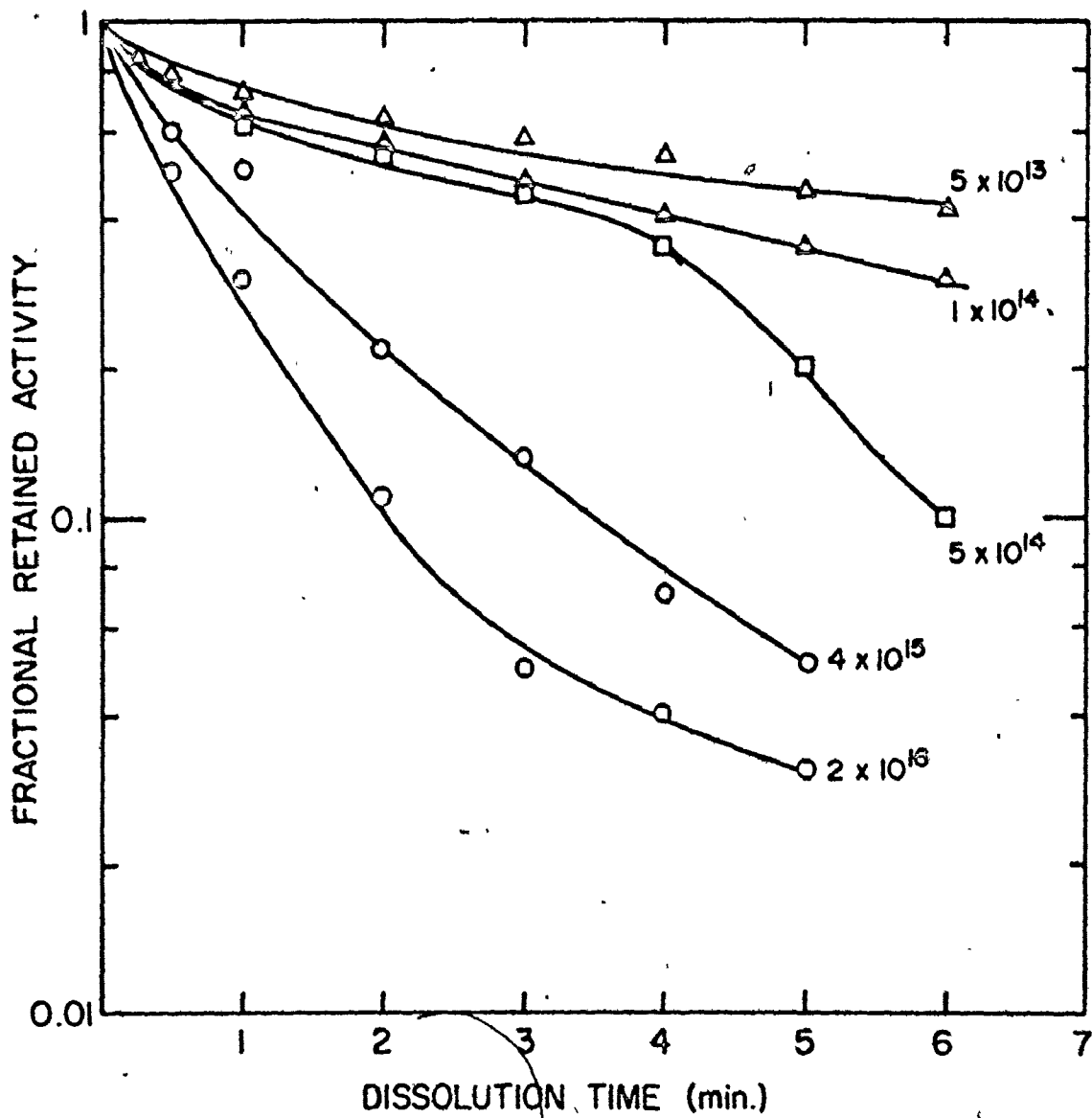


Fig. 6-1 Activity vs time of exposure to fluoboric acid saturated with ammonium chloride for  $\text{Nb}_2\text{O}_5$  pellets bombarded with 35 keV  $^{85}\text{Kr}$  to various doses (ions/cm<sup>2</sup>).

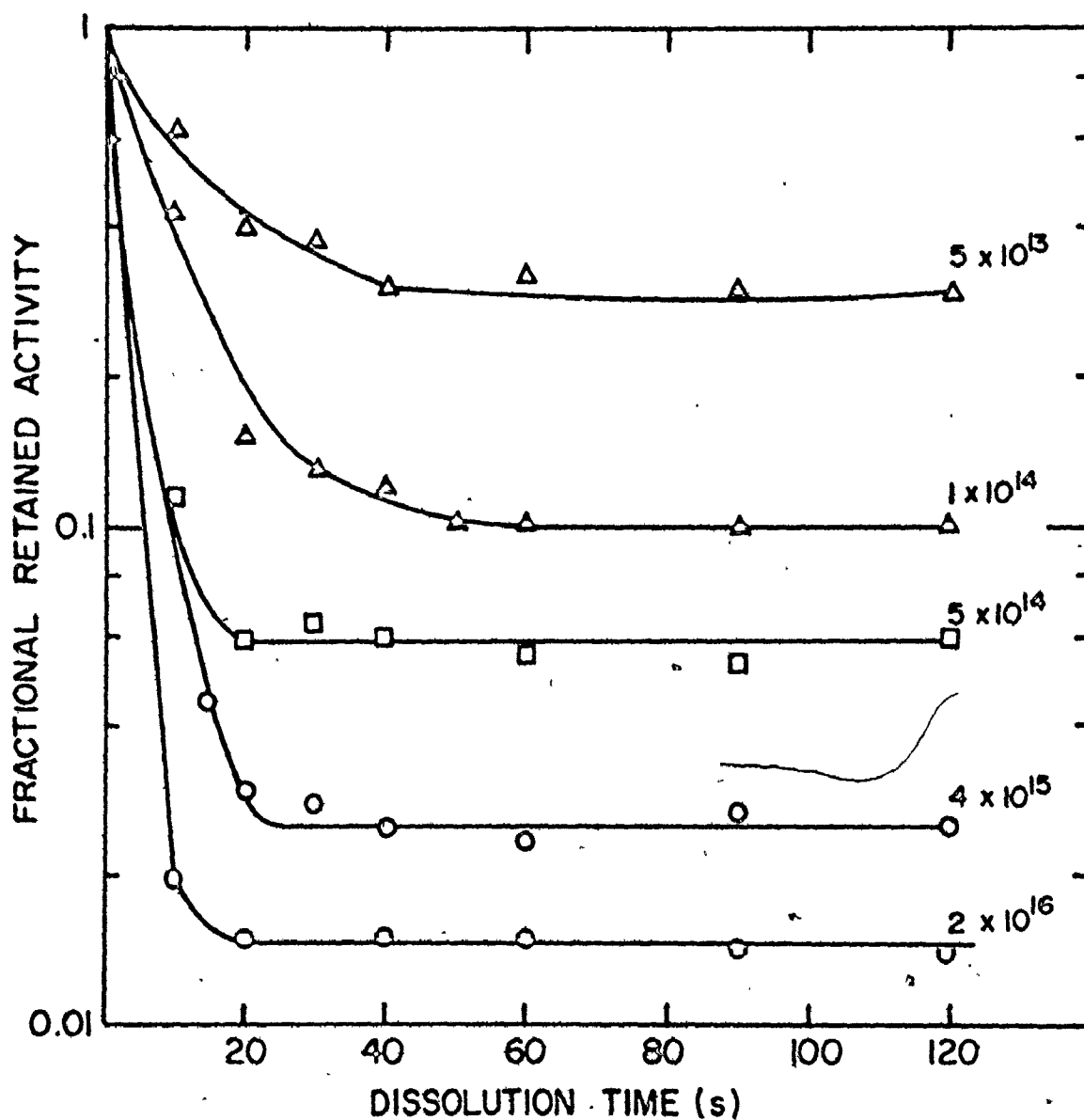


Fig. 6-2. Activity vs time of exposure to a solution consisting of  $\text{HF}$ ,  $\text{HNO}_3$  and  $\text{H}_2\text{O}$  for  $\text{Nb}_2\text{O}_5$  pellets bombarded with 35 keV  $^{85}\text{Kr}$  to various doses ( $\text{ions/cm}^2$ ).

Further evaluation was carried out using the numerical values  $\langle x \rangle = 7.25 \text{ } \mu\text{g}/\text{cm}^2$  and  $\mu_2^{1/2} = 2.85 \text{ } \mu\text{g}/\text{cm}^2$  (99) and taking the density of  $\text{Nb}_2\text{O}_5$  to be  $4.74 \text{ g}/\text{cm}^3$  (57). Equation (6-1) is shown graphically in Figure 6-3a while the depths of the altered layers as a function of ion dose are summarized in Table 6-1. We note that the ratio  $R_a/\langle x \rangle$  lies in the region 1.2 to 1.8.

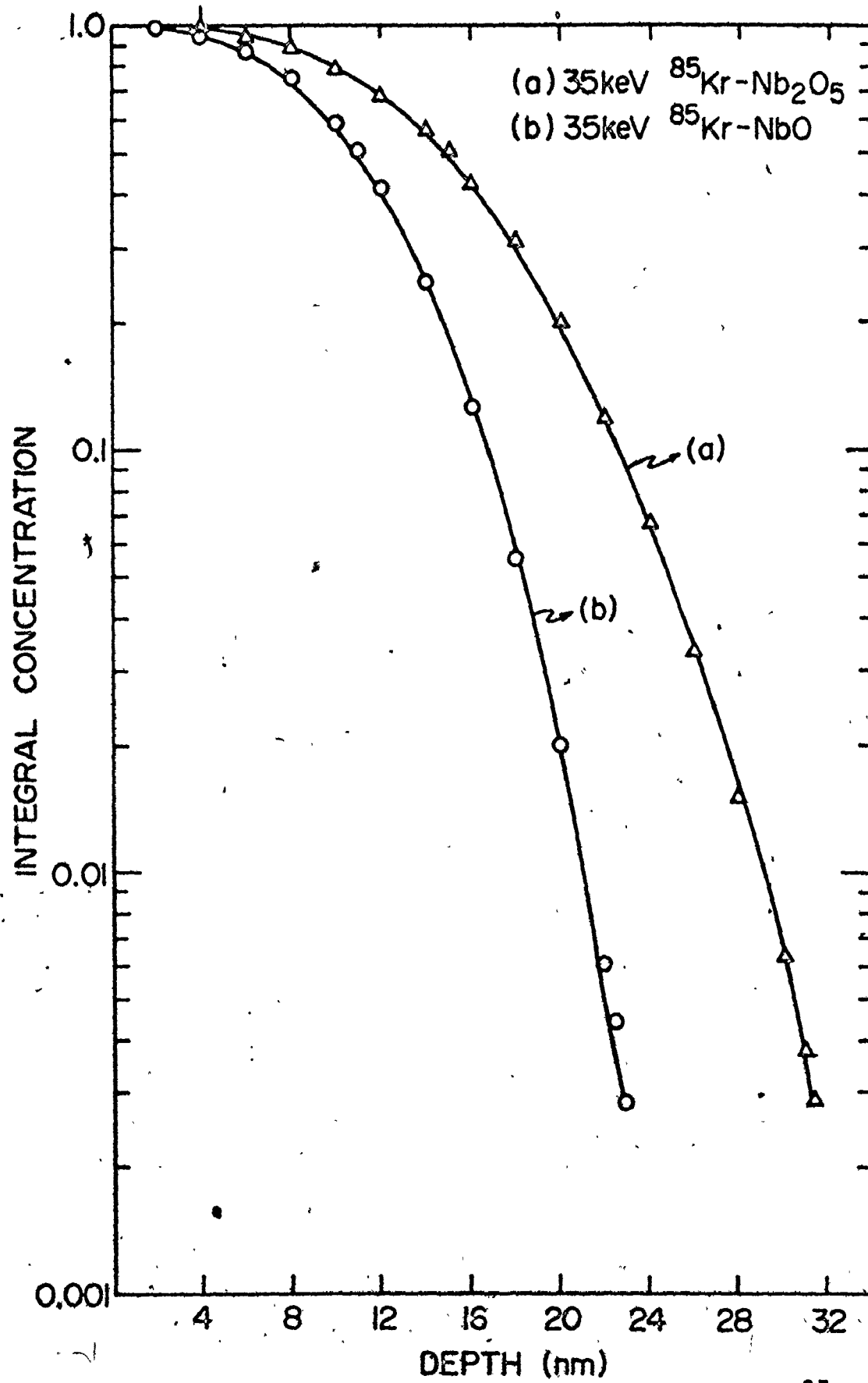
Table 6-1

Altered layer thicknesses for 35 keV Kr bombardment of  $\text{Nb}_2\text{O}_5$  pellets

Dose ions/ $\text{cm}^2$	Fractional retained activity at discontinuity	$R_a$ nm	$R_a/\langle x \rangle$
$5 \times 10^{13}$	0.3	18.0	1.2
$1 \times 10^{14}$	0.1	22.5	1.5
$5 \times 10^{14}$	0.06	24.4	1.6
$4 \times 10^{15}$	0.025	27.0	1.8
$2 \times 10^{16}$	0.015	28.0	1.8

From the results of the structural changes in  $\text{Nb}_2\text{O}_5$  pellets induced by ion bombardment (section 4.4) it follows that the altered layer refers to an amorphous layer. The results of Table 6-1 indicate the depths of amorphization as a function of ion dose. The amorphous layer thickness varies from 1.2 to 1.8 times the mean projected range (15 nm). The amorphous layer thickness formed in Si due to 40 keV P ion bombardment has been estimated by et al. (18) using thickness interference fringes and





Dissolution techniques have been used before to determine the amorphous layer thicknesses formed by ion bombardment of  $\text{WO}_3$  (97),  $\text{Al}_2\text{O}_3$  (96) and Si (49). The results are summarized in Table 6-2. It can be noted that the amorphous layer thickness is about twice the mean projected range.

Table 6-2

Comparison of  $R_a/\langle x \rangle$  for various materials

Material	Ion energy keV	Ion dose ions/cm <sup>2</sup>	$R_a/\langle x \rangle$	Reference
$\text{Nb}_2\text{O}_5$	35	$10^{13}$ to $10^{16}$	1.2 to 1.8	This thesis
$\text{WO}_3$	35	$10^{14}$ to $10^{15}$	1.9 to 2.5	97
$\text{Al}_2\text{O}_3$	18	$10^{14}$	2.2	96
Si	40	$10^{14}$ to $10^{15}$	1.5 to 2.2	49

### 6.3 THICKNESS OF ALTERED LAYER AT HIGH DOSES

The question of the thickness of the altered layer formed at high doses still remains. An answer can be sought in dissolution experiments where changes in conductivity or colour are monitored.  $\text{Nb}_2\text{O}_5$  pellets were bombarded with 35 keV  $\text{Kr}^+$  and  $\text{O}_2^+$  ions to a dose in the saturation region ( $\sim 2 \times 10^{17}$  ions/cm<sup>2</sup>) and labelled with 35 keV  $^{85}\text{Kr}$  ions (at a dose of  $1 \times 10^{15}$  ions/cm<sup>2</sup>). The pellets were exposed to the same mixture of hydrofluoric acid, nitric acid and water as was discussed in sect. 6.2 and the conductivity of the surface monitored as a function of the time of exposure. In addition, the fractional retained activity was measured in each case. The results are depicted in Figure 6-4. The conductivity of the pellet attains a value nearly equal to that of an unbombarded specimen after an exposure to the solvent for 20 s and with a fractional retained activity of about 0.003. Taking this to correspond to the dissolution of the altered layer formed by bombardment at high doses and converting the activity to a depth scale, the thickness of the NbO layer can be determined. The integral concentration profile for 35 keV  $^{85}\text{Kr}$  ions incident on NbO, deduced using the parameters  $\langle x \rangle = 11$  nm and  $\mu_2^{1/2} = 4.4$  nm (Appendix I), is depicted in Figure 6-3b. It can be seen that a fractional retained activity of 0.003 corresponds to a depth of 23 nm. Hence the thickness of the NbO layer formed by high dose ion bombardment is 23 nm.

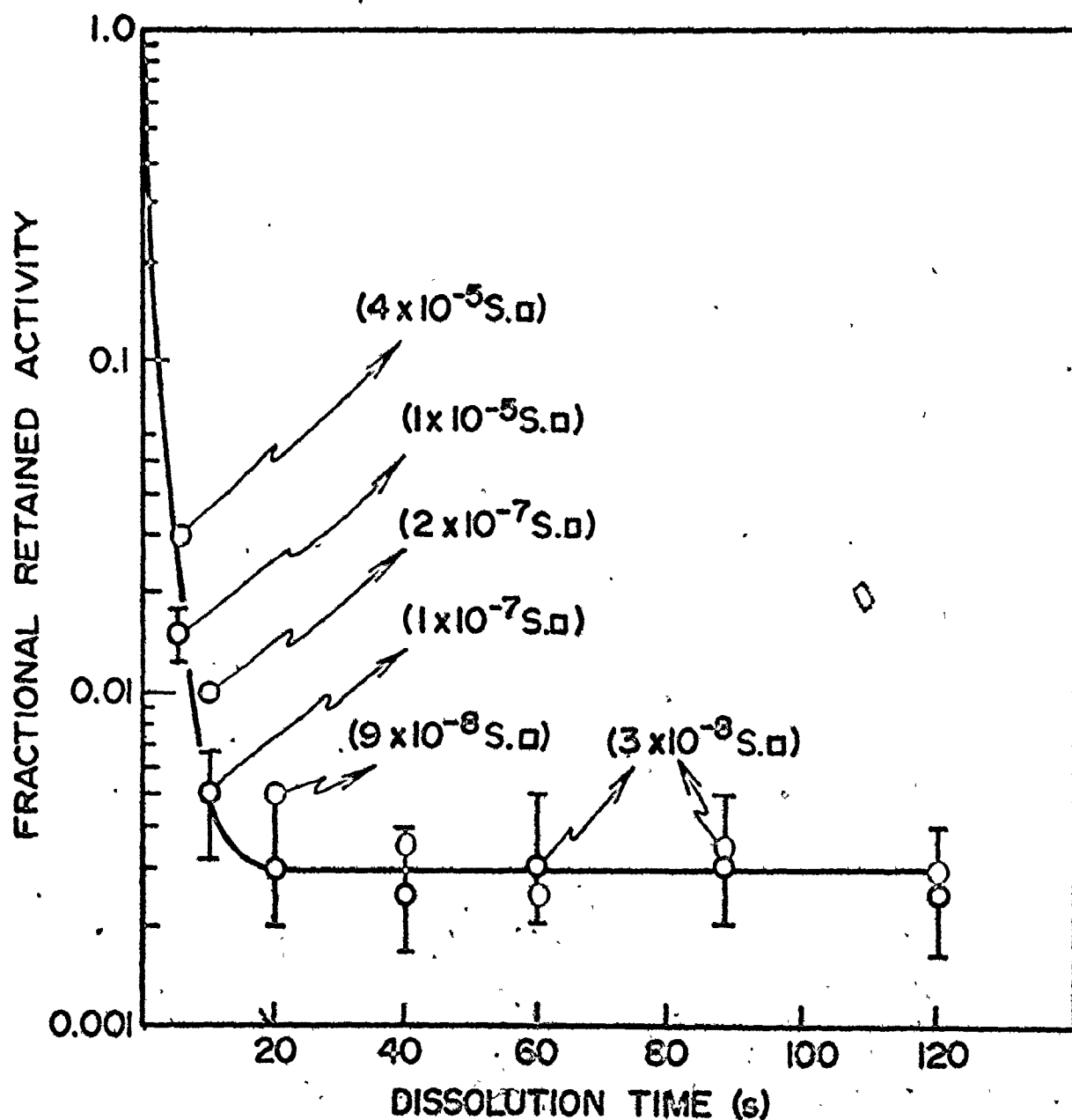


Fig. 6-4 Dissolution of altered layers formed on  $\text{Nb}_2\text{O}_5$  pellets bombarded with 35 keV  $\text{Kr}^+$  (o) and 35 keV  $\text{O}^+$  (o) to doses of about  $2 \times 10^{17}$  ions/ $\text{cm}^2$  and labelled with 35 keV  $^{85}\text{Kr}$  at a dose of  $10^{15}$  ions/ $\text{cm}^2$ . Also shown are sheet conductivities as a function of time of exposure to the solvent:

#### 6.4 IMPLICATIONS OF THICKNESS OF NbO LAYER

After a determination of the thickness of the conducting layer we are now in a position to compare the changes in conductivity induced by ion bombardment in more natural units i.e. S/m.

Bulk conductivity of unbombarded  $\text{Nb}_2\text{O}_5$  pellet =  $2.0 \times 10^{-5}$  S/m.

Conductivity of bombarded  $\text{Nb}_2\text{O}_5$  pellet

$$= \frac{1.0 \times 10^{-4}}{23 \times 10^{-9}}$$

$$= 4.3 \times 10^3 \text{ S/m .}$$

Factor increase in conductivity due to bombardment =  $2 \times 10^8$ .

Conductivity of bombarded pellet subsequently heated in vacuum at  $700^\circ\text{C}$

$$= \frac{6 \times 10^{-2}}{23 \times 10^{-9}}$$

$$= 2.6 \times 10^6 \text{ S/m}$$

Factor increase in conductivity due to both bombardment and annealing

$$= 1.3 \times 10^{11}.$$

Although it is generally accepted that NbO exhibits metallic conductivity there are very few published results (93,94,95). The values range from 1 S/m (94) to  $5 \times 10^6$  S/m (95). We would point out also that the conductivity of a metal like copper is about  $6 \times 10^7$  S/m (100). The bombardment induced conductivity found with  $\text{Nb}_2\text{O}_5$  is thus similar to what is expected for NbO

is able to what

is found for normal metals. We would emphasize however that absolute comparisons of the conductivity results is somewhat hampered due to the unknown role played by the purity and by the sample preparation conditions.

### 6.5 SUMMARY AND CONCLUSIONS

A technique based on the changes in the chemical reactivity of the altered layer as compared to the substrate is used to estimate the thickness of the altered layer on bombarded  $\text{Nb}_2\text{O}_5$ . It consists of bombarding with an appropriate dose of  $\text{Kr}^+$  or  $\text{O}_2^+$ , injecting a tracer dose of radioactive  $^{85}\text{Kr}$ , removing the altered surface layer chemically and noting the residual  $^{85}\text{Kr}$  activity. The residual activity is then re-expressed as a depth using an integral ion distribution curve.

The thickness of the altered layer on  $\text{Nb}_2\text{O}_5$  varies from 18 nm at very low doses ( $5 \times 10^{13}$  ions/cm<sup>2</sup>) to 23 nm at high doses ( $1 \times 10^{17}$  ions/cm<sup>2</sup>). The conductivity of the altered layer formed at high doses is about  $4.3 \times 10^3$  S/m, an increase in conductivity by a factor of  $2 \times 10^8$ . Specimens which are both bombarded and annealed in vacuum show a high dose conductivity of  $2.6 \times 10^6$  S/m, corresponding to an increase by a factor of  $1.3 \times 10^{11}$ .

Such changes in a basic physical property are regarded as amongst the largest that have been observed with any system.

## CHAPTER 7

### DISCUSSION OF EXPERIMENTAL RESULTS

#### 7.1 INTRODUCTION

In this chapter attention is focused on mechanisms to explain the experimental results. The experimental results as outlined in chapters 4, 5 and 6 can be summarized as follows.

- 1) Bombardment of  $\text{Nb}_2\text{O}_5$  with 35 keV  $\text{Kr}^+$  or  $\text{O}_2^+$  ions at high doses leads to the formation of an altered surface layer with the structure of  $\text{NbO}$ .
- 2) Oxygen ion bombardment exhibits a threshold energy to cause reduction.
- 3) The thickness of the altered layer at high doses is about 23 nm, equivalent to about twice the mean projected range for 35 keV  $\text{Kr}^+$  ions incident on  $\text{NbO}$ .
- 4) The thickness of the  $\text{NbO}$  layer as reflected in the conductivity is independent of current density in the low current region ( $< 10 \mu\text{A}/\text{cm}^2$ ).

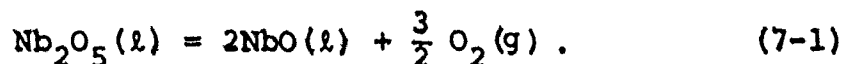
In what follows we will consider the following.

- 1) Mechanisms for oxygen loss due to ion bombardment.
- 2) Role of an oxygen ion beam in causing reduction.
- 3) Role of diffusion in forming the altered layer with special regard to the thickness of the layer.

## 7.2 MECHANISMS FOR OXYGEN LOSS

### 7.2.1 Vaporization model

An ion impacting on a solid surface will cause not only displacements but also a briefly lived temperature increase. The latter, called a thermal spike, is sufficient to enhance activated processes of small spatial extent such as vaporization (32,101). It was argued elsewhere (32) that the condition for vaporization to occur is that the vapor pressure exceeds 0.5 to 5.0 MPa at roughly 2700°C. In the present context the relevant vaporization process is the following:



Since the vapor pressure at 2700°C is only 40.5 Pa (102) we conclude that thermal spike induced vaporization of  $\text{Nb}_2\text{O}_5$  is quite incapable of leading to the formation of NbO.  $\text{Nb}_2\text{O}_5$  thus resembles  $\text{TiO}_2$ , where vaporization was also excluded as being at the origin of the evolution to  $\text{Ti}_2\text{O}_3$ , but not  $\text{MoO}_3$  and  $\text{V}_2\text{O}_5$  where the oxygen partial pressures are sufficient to contribute to the formation of  $\text{MoO}_2$  and  $\text{V}_2\text{O}_3$  (32).

### 7.2.2 Internal displacement model

The other main effect of an impacting ion is the creation of a distribution of displaced atoms. In the present context we will distinguish between those displacements which result in a net loss of material (sputtering) and those which lead to a rearrangement.

al rearrangement of oxygen, with resultant formation



of nuclei of a lower oxide, will occur firstly if the displacement energy for oxygen is sufficiently low. Nothing is known about the displacement energies for this system but there is another condition for rearrangement. This is that the energy transfer process favors oxygen to a greater extent than required by the atom fraction of oxygen. A similar concept is contained in the expression deduced by Andersen and Sigmund (54) for  $N_i$ , the number of displaced atoms in a binary compound (see also Section 2.9)

$$N_i = \frac{E x_i K_i}{E_{d_i}}, \quad (7-2)$$

where  $E$  is the incident ion energy,  $x_i$  is the atom fraction,  $K_i$  is the displacement efficiency and  $E_{d_i}$  is the displacement energy. The significant parameter is  $K_i$ , which is not necessarily 0.5 as often assumed. As discussed in chapter 2, section 2.9, the displacement efficiency for the system Nb-O was evaluated by Andersen and Sigmund (55) and the displacement of oxygen was found to be preferred for stoichiometries exceeding  $\text{NbO}_2$ .

Unfortunately the model has two important limitations:

- 1) Heavy emphasis is placed on subtle differences in the numerical constants  $K_i$ . Moreover  $K_i$  has to be evaluated for each system and has yet to be obtained exactly for any system.
- 2) The effect of the displacement energy  $E_{d_i}$  is probably significant and hence should have been taken into account in predicting the stoichiometry changes. Nevertheless  $E_{d_i}$  is known for very few oxides, namely  $\text{Al}_2\text{O}_3$  (103) and  $\text{SiO}_2$  (104).

In the work the experimental results of chapter 5,

section 5.3, can be used as direct evidence for the inapplicability of the model based on the internal rearrangement of oxygen. Oxygen loss due to rearrangement will be to some extent reversed by vacuum heating. Some reversal occurs, for example, when LiF containing precipitated Li and  $F_2$  is heated (105). Referring to the results of chapter 5, section 5.3, we find that annealing bombarded  $Nb_2O_5$  at  $700^\circ C$  in vacuum left it black, highly conductive and having a persistent diffraction pattern of NbO. Based primarily on the experimental results, the internal rearrangement model may be concluded to be disfavoured as a mechanism for oxygen loss.

### 7.2.3 Preferential sputtering model

Preferential sputtering of oxygen from an oxide with resultant formation of a lower oxide can be envisaged to take place for at least four reasons.

- (a) According to Sigmund's theory (section 2.8) the sputtering yield  $S$  is related to surface binding energy  $E_b$ :

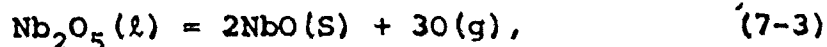
$$S \propto 1/E_b$$

Jackson (106) has shown that  $E_b$  which applies to an in surface atom is somewhat greater than  $\Delta H_{\text{atomization}}$  which applies to a more loosely bound atom though we will in what follows make no distinction between  $E_b$  and  $\Delta H_{\text{atomization}}$ .

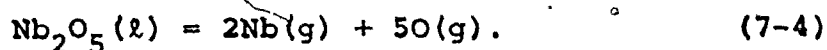
Preferential sputtering of oxygen from an oxide may be assumed to occur whenever the surface binding energy for partial oxygen removal (a process similar to partial atomization) is of an atom (a process

similar to the total atomization).

Table 7-1 shows the heats of atomization for processes involving either partial atomization, for example



or total atomization, for example



The starting materials are taken as liquids in view of the amorphization induced by low dose ion bombardment.

Table 7-1

Heats of atomization appropriate  
to the system Nb-O (Ref. 102)

Reaction	$\Delta H_a$ (eV/gas atom)
$\text{Nb}_2\text{O}_5(\ell) = 2\text{Nb}(\text{g}) + 5\text{O}(\text{g})$	6.7
$\text{Nb}_2\text{O}_5(\ell) = 2\text{NbO}_2(\ell) + \text{O}(\text{g})$	5.9
$\text{Nb}_2\text{O}_5(\ell) = 2\text{NbO}(\text{s}) + 3\text{O}(\text{g})$	5.9
$\text{Nb}_2\text{O}_5(\ell) = 2\text{Nb}(\text{s}) + 5\text{O}(\text{g})$	6.3

It can be seen from Table 7-1 that the surface binding energies, taken as being equivalent to the heats of atomization per gas atom, have a minimum for  $\text{NbO}_2$  and  $\text{NbO}$ . This suggests that preferential sputtering may be responsible for oxygen loss from bombarded  $\text{Nb}_2\text{O}_5$ . Sputtering is regarded as confined to the surface and it is proposed that preferential sputtering combined with diffusion might result in an altered layer extending into the target.

- (b) Preferential sputtering of oxygen can occur secondly due to the peculiarities of the structure of the oxide surface. For example, Fiermans and Vennik (107) have pointed out that the (010) surface of  $\text{V}_2\text{O}_5$  exposes oxygen ions only, the metal ions being screened.

This oxygen is readily removed by electron bombardment but is in part replaced by oxygen diffusing from beneath the surface such that a surface layer with stoichiometry  $V_6O_{13}$  results and the oxygen ions remain exposed. This effect could in principle occur to an even greater extent with an ion beam, resulting in the surface layer being  $V_2O_3$ , the observed result (28). We prefer not to pursue the model here. The main problem is that an ion beam amorphizes not only  $V_2O_5$  but also  $Nb_2O_5$  and it is difficult to know if the amorphous phase retains the necessary structural peculiarities.

- (c) A third mechanism for preferential oxygen removal, closely related to (b), follows from work by Van Landuyt and Amelinckx (108). We again suppose oxygen to be readily sputtered from an oxide surface by virtue of being exposed. Rather than oxygen then migrating from the interior towards the surface, the exposed metal ions move as interstitials in the contrary sense. This leads to ever deepening/hair-pin shaped shear planes as observed with  $TiO_2$  (108) and causes the surface layer to persist in having oxygen ions exposed. Again amorphization presents problems which make the model difficult to develop.
- (d) A fourth mechanism for preferential oxygen removal follows from other work by Fiermans and Vennik (109). They had evidence for the formation of CO and  $CO_2$  at a  $V_2O_5$  surface owing to the combined effect of contaminating carbon and the incident electron beams. Carbon contamination is well known also with ion beams.

We would tend to exclude an effect due to carbon on the grounds that similar results were obtained both for  $\text{Kr}^+$  and  $\text{O}_2^+$  ion bombardments. This leaves mechanisms (a) to (c), amongst which a valid distinction cannot at present be made. For example, all mechanisms (a) to (c), involve diffusion and would show a similar temperature dependence.

### 7.3 SPUTTERING MODEL APPLIED TO AN OXYGEN BEAM

The main difference between an oxygen and Kr beam is, as pointed out by Meyer et al. (110), that oxygen leads to a steady-state oxygen concentration in excess of that otherwise present. The depth distribution of ions and damage in a solid target changes at high doses as the target surface recedes due to sputtering. The problem has been discussed previously by Meyer et al. (110), Carter et al. (111) and Biersack (112). It has been shown by Biersack (112) that a unique high dose distribution exists which is simply the integral of the initial distribution.

We take the differential oxygen distribution in  $\text{Nb}_2\text{O}_5$  as Gaussian, which is justified in view of the amorphization:

$$C^{\text{diff}}(x)dx = \frac{dx}{(2\pi\mu_2)^{1/2}} \exp\left[-\frac{(x-\langle x \rangle)^2}{2\mu_2}\right], \quad (7-5)$$

where  $\langle x \rangle$  is the mean projected ion range and  $\mu_2$  is the mean square projected ion straggling. Sputtering of the surface causes the differential profile to move inwards into the target with a velocity  $v$  given by

$$v = \frac{BS}{N} \text{ cm/s}, \quad (7-6)$$

where  $B$  is the ion current in ions/ $\text{cm}^2\text{s}$ ,  $N$  is the number density

of the target, and  $S$  is the sputtering coefficient. Assuming dose independent range and sputtering parameters, the total differential concentration for  $Bt$  ions/cm<sup>2</sup> becomes:

$$\begin{aligned}
 C^{diff}(x,t)dx &= B \int_0^t dt C^{diff}\{x + (BtS/N)\}dx \\
 &= \frac{Ndx}{2S} \left[ \operatorname{erfc}\left(\frac{x-\langle x \rangle}{(2\mu_2)^{1/2}}\right) \right. \\
 &\quad \left. - \operatorname{erfc}\left(\frac{x+(BtS/N)-\langle x \rangle}{(2\mu_2)^{1/2}}\right) \right]. \quad (7-7)
 \end{aligned}$$

This oxygen distribution is regarded as being superimposed not on the initial stoichiometry of  $Nb_2O_5$ , but rather on that which is developed by Kr bombardment, namely  $NbO$ . If the latter stoichiometry for metal  $M$  is written in general as  $MO_a$ , then the volume associated with each  $M$  atom is

$$\lambda^3 = (1+a)/N, \quad (7-8)$$

where  $\lambda$  is the average cation spacing. The additional oxygen,  $\Delta a$ , per  $M$  atom arising due to bombardment with  $O_2^+$  follows by combining equations (7-7) and (7-8) and multiplying by 2:

$$\begin{aligned}
 \Delta a &= \left(\frac{1+a}{S}\right) \left[ \operatorname{erfc}\left(\frac{x-\langle x \rangle}{(2\mu_2)^{1/2}}\right) \right. \\
 &\quad \left. - \operatorname{erfc}\left(\frac{x+(BtS/N)-\langle x \rangle}{(2\mu_2)^{1/2}}\right) \right]. \quad (7-9)
 \end{aligned}$$

We note that the critical value of  $\Delta a$  for  $Nb_2O_5$  is 1.5 in the sense that for  $\Delta a < 1.5$  the specimen will be deficient in oxygen. This defines a critical sputtering yield provided an esti-

mate of the depth of the altered layer is available. The critical sputtering yield can be related to a critical bombardment energy provided the variation of sputtering yield with energy is known. The information sought can be obtained from suitable experiments as indicated below.

The thickness of the altered layer as obtained from 5 keV oxygen ion bombardment of  $\text{Nb}_2\text{O}_5$  pellets was determined using the dissolution technique as outlined in chapter 6. This was carried out by bombarding with 10 keV  $^{85}\text{Kr}$  (radioactive) at a dose of  $2 \times 10^{13}$  ions/cm<sup>2</sup> and measuring the fractional retained activity at the discontinuity in the dissolution curve. The etchant used was the so called P-etch as described in chapter 6 and the results are shown in Fig. 7-1. From the integral concentration profile for 10 keV Kr ions incident on  $\text{Nb}_2\text{O}_5$  (Fig. 7.2), the thickness of the altered layer was estimated to be 5.5 nm. This can be compared with the range parameters for 5 keV oxygen ions incident on  $\text{Nb}_2\text{O}_5$  namely  $\langle x \rangle = 4.7$  nm (Appendix II).

The variation of sputtering yield with incident ion energy was obtained by bombarding  $\text{Nb}_2\text{O}_5$  pellets with  $\text{Kr}^+$  and  $\text{O}_2^+$  ions of various energies at a constant dose of  $2 \times 10^{17}$  ions/cm<sup>2</sup> and determining the weight loss. If the oxide thickness removed by sputtering is  $X$  then the sputtering yield  $S$  can be obtained from the equation

$$X = \frac{BtS}{N}$$

For  $X$  in  $\mu\text{g}/\text{cm}^2$  and  $Bt$  in  $\mu\text{A-min}/\text{cm}^2$  this rearranges to

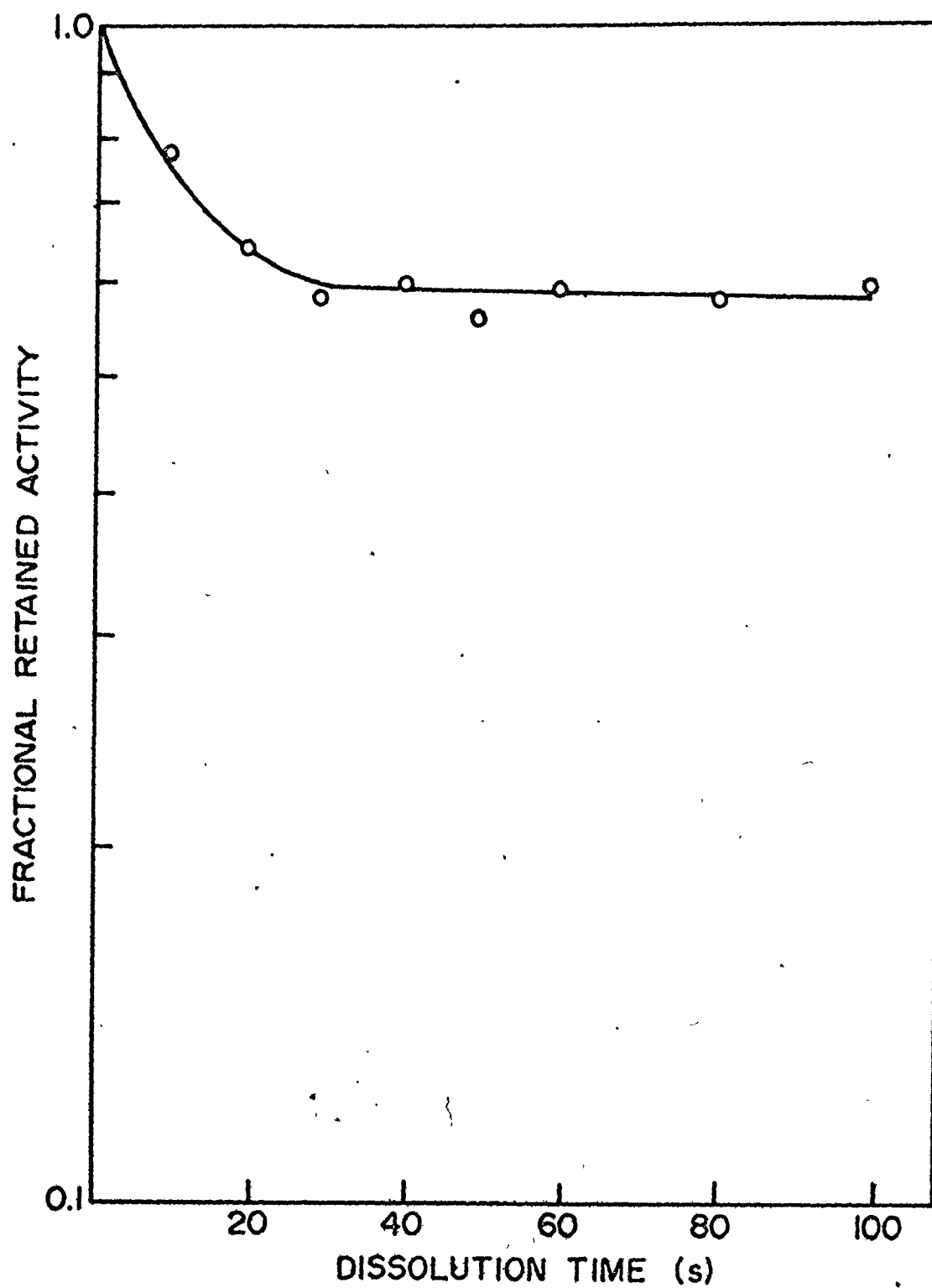
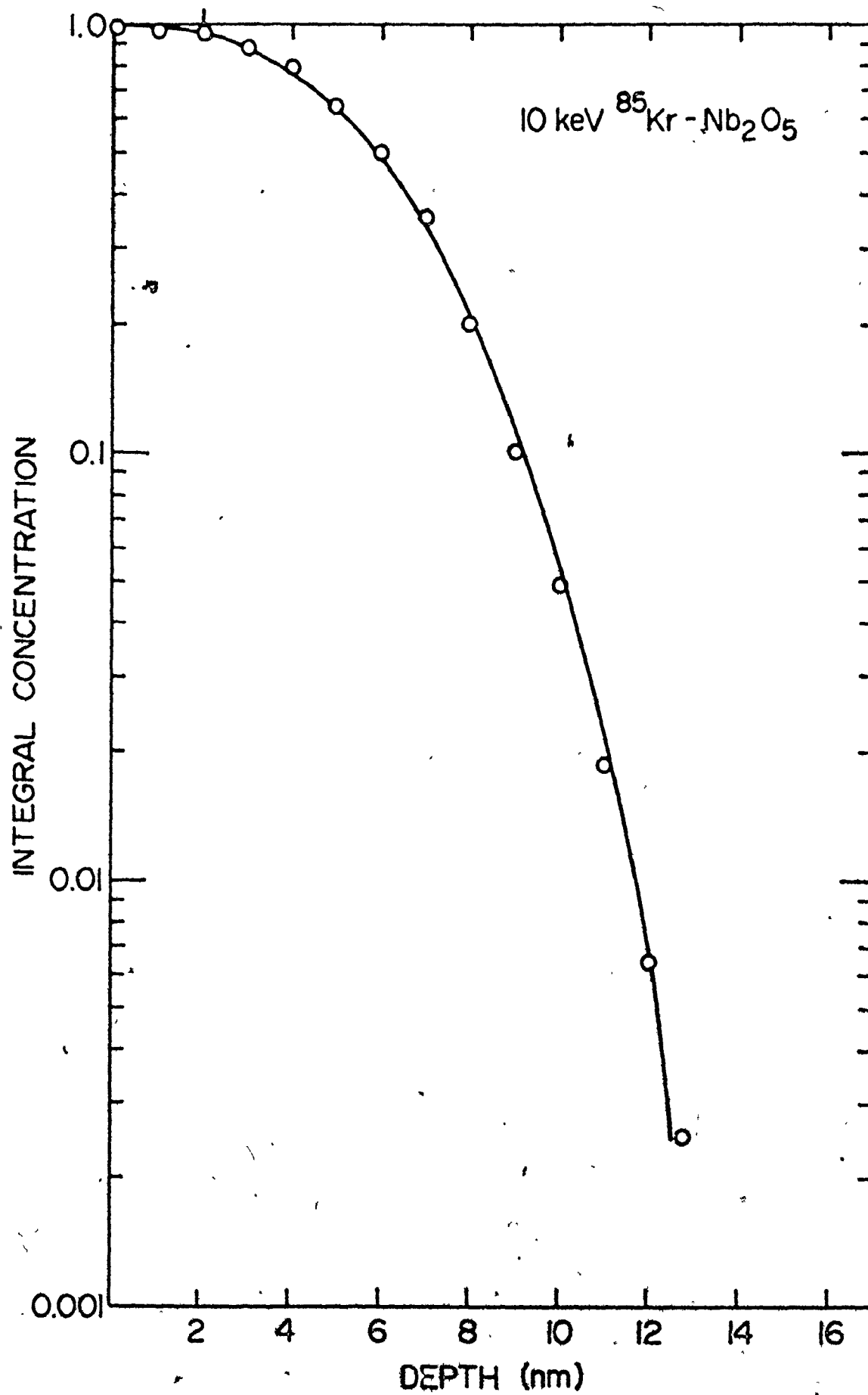


Fig. 7.1 Dissolution curve for 5 keV  $O_2^+$  ion bombarded  $Nb_2O_5$  pellets, subsequently labelled with 10 keV  $^{85}Kr$ .





where  $\bar{M}$  is the mean atomic mass of the target and  $S$  is the sputtering yield in atoms/ion. The results are shown in Figure 7-3.

By solving equation (7-9) with  $\Delta a = 1.5$  various critical sputtering yields can be obtained for various values of  $x$ . Then, using Fig. 7-3, the critical sputtering yields can be related to critical bombardment energies with results as summarized in Table 7-2. The critical energies in Table 7-2 are actually the lower of the two values corresponding to each value of  $S$ . The higher values will lie well above 50 keV and therefore do not interest us here. The experimental results presented above indicate that  $x = \langle x \rangle$  and hence the critical bombardment energy using an oxygen beam to cause reduction is 7 keV. This agrees with the observed threshold energy for conductivity changes (chapter 5, section 5.2) of 5 keV.

Table 7-2

Oxygen ion bombardment of  $Nb_2O_5$ -critical bombardment energies to cause reduction

$x/\langle x \rangle$	Critical S Atoms/Ion	Critical E keV.
0	2.7	20
0.5	2.4	15
1.0	1.3	7
1.2	0.8	3.5 *
1.5	0.28	1.3 *
2.0	0.02	$\sim 0$ *

\* Interpolated from Fig. 7-3

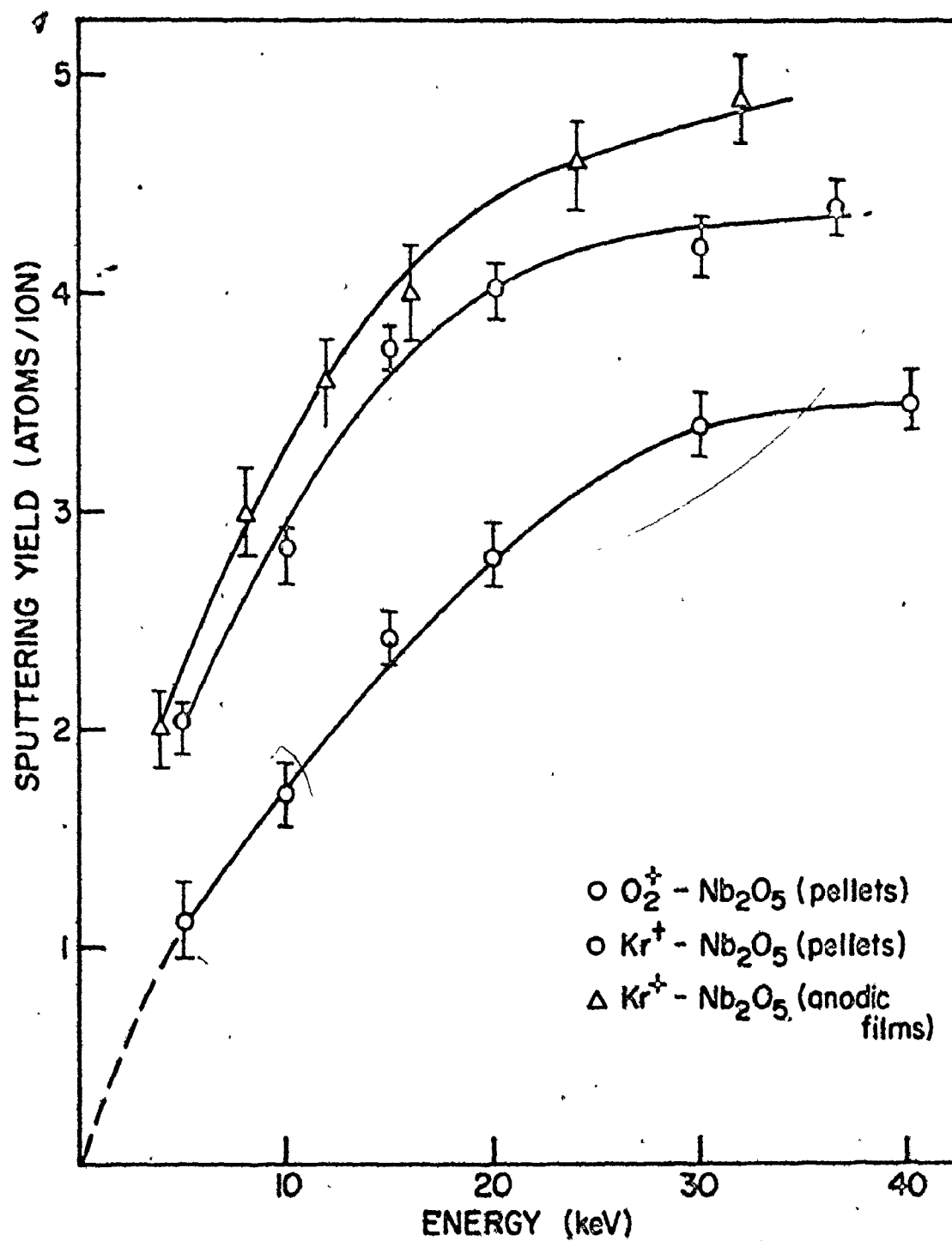


Fig. 7-3 Effect of ion energy on sputtering yield

## 7.4 PREFERENTIAL SPUTTERING COMBINED WITH DIFFUSION

### 7.4.1 Diffusion model

Preferential sputtering may be taken as setting up a diffusion geometry involving a continuous plane source at  $x = 0$ . The boundary condition at  $x = 0$  for the differential free concentration,  $C(x,t)$ , is therefore

$$C(0,t) = C_0 \text{ atoms/cm}^3, \quad (7-11)$$

where  $C_0$  could be called the surface stoichiometry. The continuous plane source probably consists of an uniformly reduced surface of the type detected in work using surface probes such as photoelectron spectroscopy. Thus, bombarded  $\text{CuO}$ ,  $\text{Fe}_2\text{O}_3$ ,  $\text{MoO}_3$ ,  $\text{NiO}$ ,  $\text{PbO}_2$ ,  $\text{PdO}$ , and  $\text{WO}_3$  had surfaces consisting respectively of  $\text{Cu}$ ,  $\text{Fe}$ ,  $\text{MoO}_2$ ,  $\text{Ni}$ ,  $\text{Pb}$ ,  $\text{Pd}$  and  $\text{W}$  (30,113,114). The uniformly reduced surface may be assumed to act as a source either of anion vacancies (as envisaged for the electron beam reduction of  $\text{V}_2\text{O}_5$  (115)), or of cation interstitials (as proposed for the development of shear planes in thermally reduced  $\text{TiO}_2$  (108)). We would emphasize that we regard surface changes as detected with surface probes to be distinct from the bulk layers observed in the present work.

We will suppose the diffusing entities to move randomly in a medium whose surface is receding at a velocity  $v$  given by

$$v = \frac{BS}{N} \text{ cm/s},$$

where  $B$  is the bombarding current in  $\text{ions/cm}^2\text{s}$ , and which contains nucleation sites characterized by trapping length  $L$ .

The form taken by the diffusion equation is based on similar problems of heat conduction in a solid moving with velocity  $v$  (116) and the diffusion of gas in solids as modified by traps (117-119). This leads to

$$\frac{\partial C}{\partial t} = D \frac{\partial^2 C}{\partial x^2} + v \frac{\partial C}{\partial x} - \frac{DC}{L^2} \quad (7-12)$$

where  $L^2$  is given by  $(1-f)\lambda^2/6f$ ,  $\lambda$  being the mean atomic spacing and  $f$  being the atomic fraction of atom size nucleation sites (120)

The Laplace transform reduces a partial differential equation to an ordinary differential equation. Using the Laplace transform defined by

$$\mathcal{L}\{F(t)\} = \int_0^{\infty} e^{-Pt} F(t) dt$$

and

$$\mathcal{L}(C) = \bar{C},$$

equation (7-12) can be rearranged as

$$p\bar{C} = D \frac{\partial^2 \bar{C}}{\partial x^2} + v \frac{\partial \bar{C}}{\partial x} - \frac{D\bar{C}}{L^2}$$

or

$$\frac{\partial^2 \bar{C}}{\partial x^2} + \frac{v}{D} \frac{\partial \bar{C}}{\partial x} - \left(\frac{1}{L^2} + \frac{p}{D}\right) \bar{C} = 0 \quad (7-13)$$

The solution to equation (7-13) is given by

$$\bar{C}(x, p) = A_1 \exp(-h_1 x) + A_2 \exp(-h_2 x), \quad (7-14)$$

where  $A_1$  and  $A_2$  are constants and  $h_1$  and  $h_2$  are given by

$$h_1 = \frac{v}{2D} + \left(\frac{v^2}{4D^2} + \frac{1}{L^2} + \frac{p}{D}\right)^{1/2}$$

$$h_2 = \frac{v}{2D} - \left(\frac{v^2}{4D^2} + \frac{1}{L^2} + \frac{p}{D}\right)^{1/2}$$

To simplify equation (7-14) one has to consider the boundary conditions. These can be stated as follows:

- (1)  $\bar{C} = 0$  at  $x = \infty$
- (2)  $\bar{C} = \frac{C_0}{p}$  at  $x = 0$ .

Applying these conditions, equation (7-14) reduces to

$$\bar{C}(x, p) = \left(\frac{C_0}{p}\right) \exp(-h_1 x). \quad (7-15)$$

As a result of the trapping at the nucleation sites, there develops a differential trapped concentration,  $m(x, t)$ , which in the case of transition metal compound such as  $Nb_2O_5$  consists of a phase of lower stoichiometry:

$$\frac{\partial m}{\partial t} = \frac{DC}{L^2} + v \frac{\partial m}{\partial x}. \quad (7-16)$$

Taking the Laplace transform of equation (7-16), substituting equation (7-15), and rearranging, results in

$$v \frac{\partial \bar{m}}{\partial x} - p\bar{m} + \frac{DC_0}{L^2 p} \exp(-h_1 x) = 0, \quad (7-17)$$

where  $\bar{m}$  is defined by

$$\bar{m} = \mathcal{L}(m).$$

Letting  $\bar{m} = A \exp(-h_1 x)$  be a trial solution and substituting it in equation (7-17) we have

$$\bar{m}[-h_1 v - p + \frac{DC_0}{L^2 p A}] = 0 \dots$$

Since  $\bar{m}$  cannot be zero, it follows that  $-h_1 v - p + \frac{DC_0}{L^2 p A} = 0$  and that

$$A = \left(\frac{DC_0}{L^2 p}\right) \left(\frac{1}{h_1 v + p}\right).$$

The solution for  $\bar{m}$  is therefore

$$\bar{m}(x,p) = \left(\frac{DC_0}{L^2 p}\right) \left(\frac{1}{h_1 v + p}\right) \exp(-h_1 x). \quad (7-18)$$

We now suppose that the diffusion is sufficiently rapid, perhaps by virtue of being enhanced by the bombarding current, that equation (7-12) is now in steady state and equation (7-18) is modified to

$$\bar{m}(x,p) = \frac{DC_0}{(L^2 p)} \left(\frac{1}{h_3 v + p}\right) \exp(-h_3 x), \quad (7-19)$$

where  $h_3$  is given by

$$h_3 = \frac{v}{2D} + \left(\frac{v^2}{4D^2} + \frac{1}{L^2}\right)^{1/2}.$$

Next we consider two limiting cases such that

$$\frac{v}{D} \ll \frac{1}{L}$$

and

$$\frac{v}{D} \gg \frac{1}{L}.$$

Case 1. Let  $\frac{v}{D} \ll \frac{1}{L}$ .

Then  $h_3 = 1/L$  and equation (7-19) can be written as

$$\bar{m}(x,p) = \frac{DC_0}{L^2 p} \left(\frac{1}{v/L + p}\right) \exp\left(-\frac{x}{L}\right). \quad (7-20)$$

The solution of equation (7-20) expressed in integral form is

$$m^{int}(x,t) = \left(\frac{DC_0}{v}\right) \left(1 - \exp\left[-\frac{vt}{L}\right]\right) \left(\exp\left[-\frac{x}{L}\right]\right) \text{ atoms/cm}^2 \quad (7-21)$$

Equation (7-21) leads to the following conclusions:

- (1) The final mean thickness,  $R_a$ , of an altered layer that is reached is given by

$$R_a = L \text{ cm}.$$

(2) A half dose for stoichiometric change,  $Bt_{1/2}$ , can be calculated from the condition

$$m^{\text{int}}(x, t_{1/2}) = \frac{1}{2} m^{\text{int}}(x, \infty).$$

The half dose  $Bt_{1/2}$  is then given by

$$Bt_{1/2} = 0.693 \text{ NL/S ions/cm}^2 \quad (7-22)$$

$$= 0.693 \text{ NR}_a/\text{S ions/cm}^2. \quad (7-23)$$

Case 2. Let  $\frac{v}{D} \gg \frac{1}{L}$ .

Then  $h_3 = \frac{v}{D}$  and equation (7-19) can be written as

$$\bar{m}(x, p) = \frac{DC_0}{pL^2} \left( \frac{1}{p+v^2/D} \right) \exp\left(-\frac{xv}{D}\right). \quad (7-24)$$

The solution of equation (7-24) expressed in integral form is

$$m^{\text{int}}(x, t) = \frac{D^3 C_0}{3L^2} [1 - \exp(-\frac{v^2 t}{D})] \exp(-\frac{xv}{D}). \quad (7-25)$$

Equation (7-25) leads to the following conclusions:

(1) The final mean thickness,  $R_a$ , of an altered layer that is formed is given by

$$R_a = \frac{D}{v} \text{ cm}.$$

(2) A half dose for stoichiometric change,  $Bt_{1/2}$ , can be calculated as before from the condition

$$m^{\text{int}}(x, t_{1/2}) = \frac{1}{2} m^{\text{int}}(x, \infty).$$

The half dose  $Bt_{1/2}$  is then given by

$$Bt_{1/2} = 0.693 \left(\frac{N}{S}\right) \left(\frac{D}{v}\right) \text{ ions/cm}^2 \quad (7-26)$$



#### 7.4.2 Thickness of altered layer

An estimate of the thickness of the altered layer based on the diffusion model can be made if the half dose for stoichiometric change is known. Taking the half dose for stoichiometric change to correspond with the half dose for conductivity change, the results of section 5.1 yield

$$Bt_{1/2} = 4 \times 10^{16} \text{ ions/cm}^2 \text{ for 35 keV Kr}^+.$$

Substituting in equations (7-23) or (7-27) the values for the half dose as  $4 \times 10^{16} \text{ ions/cm}^2$ , for the atomic density of  $\text{Nb}_2\text{O}_5$  as  $7.5 \times 10^{22} \text{ atoms/cm}^3$ , and for the sputtering yield for 35 keV  $\text{Kr}^+$  incident on  $\text{Nb}_2\text{O}_5$  as 4.4 atoms/ion (Figure 7-3), the altered layer thickness can be calculated as

$$R_a = 34 \text{ nm.}$$

Hence the thickness of the altered layer (34 nm) as deduced from this model is in reasonable agreement with the thickness of the altered layer as deduced from the dissolution experiments (23 nm).

#### 7.5 SUMMARY

In this chapter, the mechanism for oxygen loss due to ion bombardment, the possibility of an oxygen beam causing reduction and the role of diffusion in forming an altered layer were considered. Oxygen loss from bombarded  $\text{Nb}_2\text{O}_5$  was considered to have three alternative origins based on a vaporization model, an internal displacement model and a preferential sputtering model. The results serve to show that the oxygen loss is due to preferential sputtering.

A modified sputtering model defines a critical sputtering

yield to cause reduction when an oxygen beam is used. A critical sputtering yield can be related to a critical bombardment energy using the variation of sputtering yield with energy (Figure 7-3). Based on this argument the critical bombardment energy that should be observed when using an oxygen beam is 7 keV, in agreement with the observed threshold energy of 5 keV.

The thickness of the altered layer can be deduced independently from a diffusion model which combines preferential sputtering of oxygen at the surface and diffusion of the relevant point defects. The thickness (34 nm) deduced from such a model is comparable with that determined from dissolution experiments (23 nm).

## CHAPTER 8

### APPLICATIONS

In this chapter we will consider various applications of the techniques and results of ion bombardment of oxides, especially as regards the bombardment of  $\text{Nb}_2\text{O}_5$ .

#### 8.1 CHANGES IN AND CONTROL OF CONDUCTIVITY

It has been demonstrated in the present work that ion bombardment of  $\text{Nb}_2\text{O}_5$  leads to drastic changes in electrical conductivity similar to effects found with  $\text{MoO}_3$ ,  $\text{V}_2\text{O}_5$  and  $\text{TiO}_2$  (24). These results suggest that there may be a severe limitation on the use of certain oxides in a radiation environment, particularly if the oxides are being used as insulators. On the other hand the changes in conductivity might lead to the fabrication of thin film resistors or alternatively thin film conduction paths.

#### 8.2 PREPARATION OF LOWER VALENCE OXIDES

Ion bombardment of transition metal oxides at high doses leads to the formation of altered surfaces having the stoichiometries of lower valence oxides. Transition metal oxides can be insulators, semiconductors, metals or undergo semiconductor-metal transitions. For example, the semiconductor-metal transition in  $\text{VO}_2$  is now well known (121,122) and potential device applications have spurred recent work on the

preparation and properties of sputtered thin films of  $\text{VO}_2$  (123,124). The results of the present study provide an alternate technique for the preparation of lower valence oxides, namely the ion bombardment of higher oxides.

### 8.3 REDUCTION OF OXIDES - MICROWAVE DISCHARGE

Studies undertaken by McTaggart (125,126) indicate that several oxides can be reduced by using atomic hydrogen produced in a microwave discharge at 2450 MHz. With  $\text{ZrO}_2$  a surface layer was formed which was black or golden and had a resistivity of about 10 m $\Omega$ .m. Similarly  $\text{HfO}_2$  and  $\text{TiO}_2$  became black and conducting. As an extension of these studies it has been proposed elsewhere that minerals containing Nb could be reduced in a hydrogen glow discharge (127). It should be pointed out that it is not the intent to suggest ion bombardment (as distinct from the use of a glow discharge) as a technique for the reduction of ores. Nevertheless the information provided by an ion bombardment study, for example that  $\text{Nb}_2\text{O}_5$  reduces to NbO to a significant depth, serves as a guide to choosing systems in a research program on reduction. We would, for example, propose that  $\text{Nb}_2\text{O}_5$  would be more effectively reduced than  $\text{ZrO}_2$ , because of the greater depth of alteration in the former case.

#### 8.4 MINERALS ON THE MOON AND IN THE EARTH'S INTERIOR

The formation of lower valence oxides has been observed from a completely different standpoint in studies on the structure of minerals on the moon and in the earth's interior. In the earth's interior, at a depth of 400 km, the pressure is about 16 GPa and the temperature is about 2000°C. By an approximate simulation of the earth's interior (pressure of 25 GPa and temperature of 400°C) it was found by Burns (128) that the lower oxidation states,  $Ti^{3+}$  and  $Cr^{2+}$ , are more stable than under normal conditions.

Studies on the structure of lunar armalcolites (from Apollo 17 soils) have been reported by Smyth (129). Armalcolite has an approximate composition of  $(Mg_{0.5}, Fe_{0.5}) Ti_2O_5$ . Two types of armalcolite, "ortho" and "para", were identified. The differences in their chemical composition were explained on the basis of charge balance, requiring approximately 12% of the Ti to be present as  $Ti^{3+}$ . This was attributed at that time to extremely reducing conditions during crystallization of the natural lunar armalcolite. However, later work (130) suggests a pressure effect due either to the minerals having formed at a great depth or else having been subjected to meteoritic impact.

Long duration solar wind bombardment of the lunar surface was simulated at a much accelerated scale with hydrogen ion beams by Wehner et al. (131). The results were similar to those of experiments using hydrogen glow discharges (section

8.3), namely that oxide surfaces become enriched with metal atoms.

We would suggest that the present work may have a close relationship with the above three examples. Thus reduction as a pressure effect due to great depths, reduction due to meteoritic impact as well as reduction due to a beam of hydrogen ions are to some extent similar to heavy ion impact. An ion bombardment study such as this provides a guide to anticipating which cations will reduce.

#### 8.5 DATING OF MINERALS

Certain minerals with uranium impurities can be accurately dated by a procedure which involves cleaving to expose an interior surface, etching the surface and counting the number of fission tracks as revealed by etching. One then counts the number of additional tracks as revealed by both neutron irradiation and etching. The age,  $A$ , of the mineral, follows from the ratio of track densities,

$$\frac{(\text{Initial track density})}{(\text{Final track density})}$$

$$= [\exp(\lambda_D A) - 1] \text{ constants/neutron dose}$$

where  $\lambda_D$ , equal to  $1.54 \times 10^{-10} \text{ a}^{-1}$ , is the decay constant of uranium.

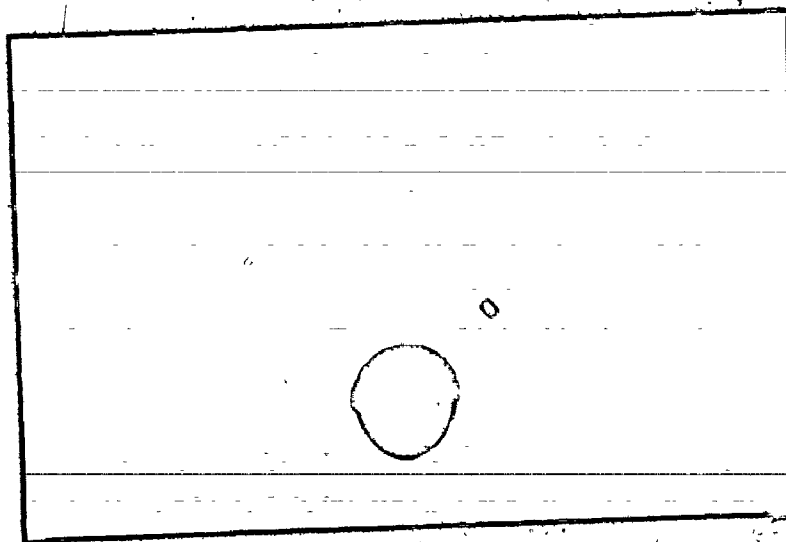
The underlying principle in this method is that fission fragments sometimes cause trails of radiation damage which in crystalline systems have a structure similar to an amorphous or metamict phase. Such phases have an enhanced chemical reactivity and provided a correct etchant can be found, can be dissolved

at a much greater rate than the substrate and thus be made visible to optical microscopy.

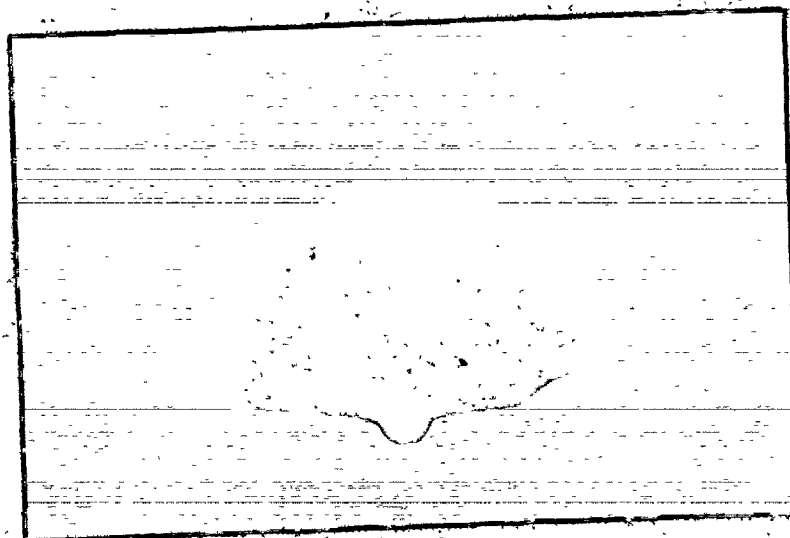
The results of the present study provide an alternative approach in which

- 1) the radiation damage is induced by ion bombardment,
- 2) the existence of amorphization is sought by electron diffraction,
- 3) the suitability of an etchant is demonstrated using dissolution curves.

Such an approach should be particularly useful in the field of fission track dating in that the emphasis is placed not on the explicit observation of tracks (which is rather difficult) but on deciding whether a mineral or group of minerals is likely to be useful for geological dating. Detailed studies using a large number of minerals to test this approach and thus, suggest new minerals for dating, have been undertaken by the writer, Naguib and Kelly (132). In particular the mineral columbite,  $(\text{FeO}, \text{MnO})(\text{Nb}_2\text{O}_5, \text{Ta}_2\text{O}_5)$  serves as an example closely related to  $\text{Nb}_2\text{O}_5$ . The amorphizability of columbite was established with reflection electron diffraction, (Fig. 8-1), and gas release measurements (132). Suitable etchants were sought by using the same etchants as for bombarded  $\text{Nb}_2\text{O}_5$  (Chapter 6). It was found that the  $\text{HF-HNO}_3$  mixture consisting of 15  $\text{cm}^3$  HF, 10  $\text{cm}^3$   $\text{HNO}_3$  and 50  $\text{cm}^3$   $\text{H}_2\text{O}$  was in fact quite effective with columbite (Figure 8-2). Based on these results, columbite has been proposed as a possible source of tracks.



(a)



(b)

Figure 8-1. Reflection electron diffraction patterns of Columbite: (a) before bombardment, (b) after bombardment with  $9 \times 10^{15}$  ions/cm<sup>2</sup> of 35 keV Ar<sup>8+</sup>.



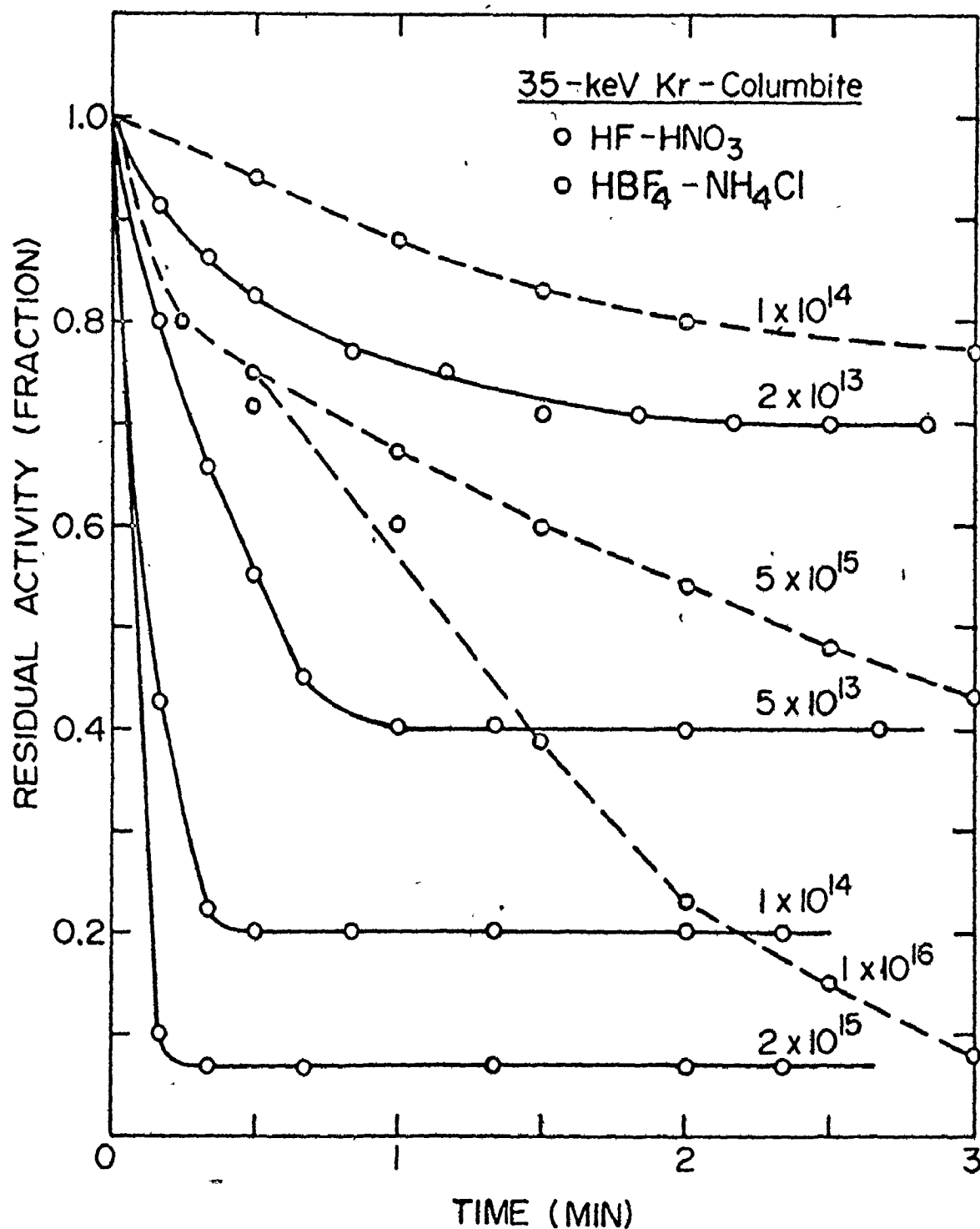


Fig. 8-2 Residual activity vs time of exposure, for columbite which has been bombarded with 35 keV <sup>85</sup>Kr to doses as indicated (in units of ions/cm<sup>2</sup>) and then exposed to an HF-HNO<sub>3</sub> mixture or HBF<sub>4</sub>-NH<sub>4</sub>Cl mixture

## 8.6 PREFERENTIAL SPUTTERING EFFECTS IN SURFACE ANALYSIS

Preferential sputtering in compounds and alloys poses a fundamental limitation to the quantitative use of Auger electron or photoelectron spectroscopy for obtaining composition profiles as the surface is gradually removed by ion bombardment. Similarly, the common procedure of cleaning samples by inert gas ion bombardment may result in changes in composition of the surface. Since Auger or photoelectrons originate from the outer surface layers (about 2 nm), the resulting spectra will not represent the original composition of the sample if the surface has been altered by ion bombardment.

Kim et al. (30, 114) have used the technique of X-ray photoelectron spectroscopy (XPS or ESCA) to monitor alterations of metal-oxygen surfaces following exposure to ion bombardment. The results shown in Figure 8-3 indicate that Ar ion bombardment of  $\text{MoO}_3$  causes changes in chemical composition due to a reduction either to a lower oxide or to the metal. After exposure to  $\text{Ar}^+$  ion bombardment  $\text{PdO}$  was reduced to Pd and the thickness of the altered surface layer was estimated from measurements of the intensity of photoelectrons. At 200 eV, the limiting value for reduction is near 1 nm, at 600 eV the layer is nearly 2 nm thick, while at 1000 eV the layer is thicker than can be measured with ESCA ( $\sim 2$  nm).

Reduction of oxides by Ar ion bombardment can seriously restrict surface compositional analysis. Alternatively the use of  $\text{O}_2^+$  ion bombardment can prevent this reduction provided

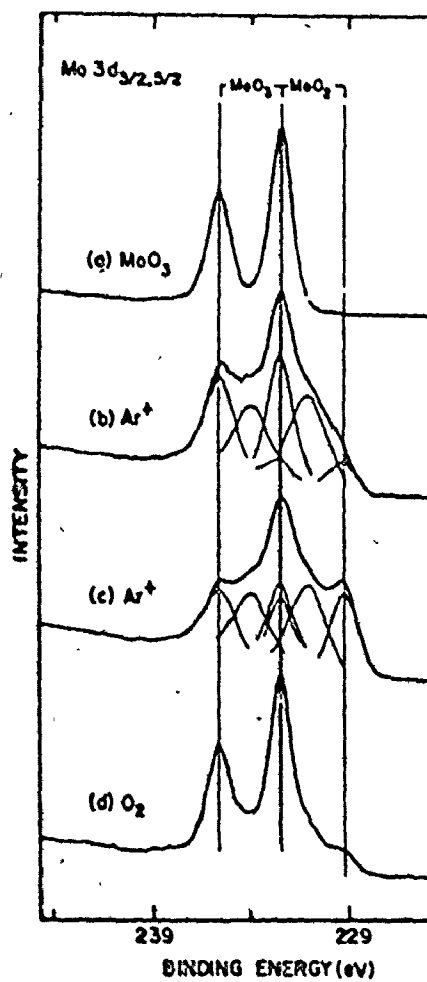


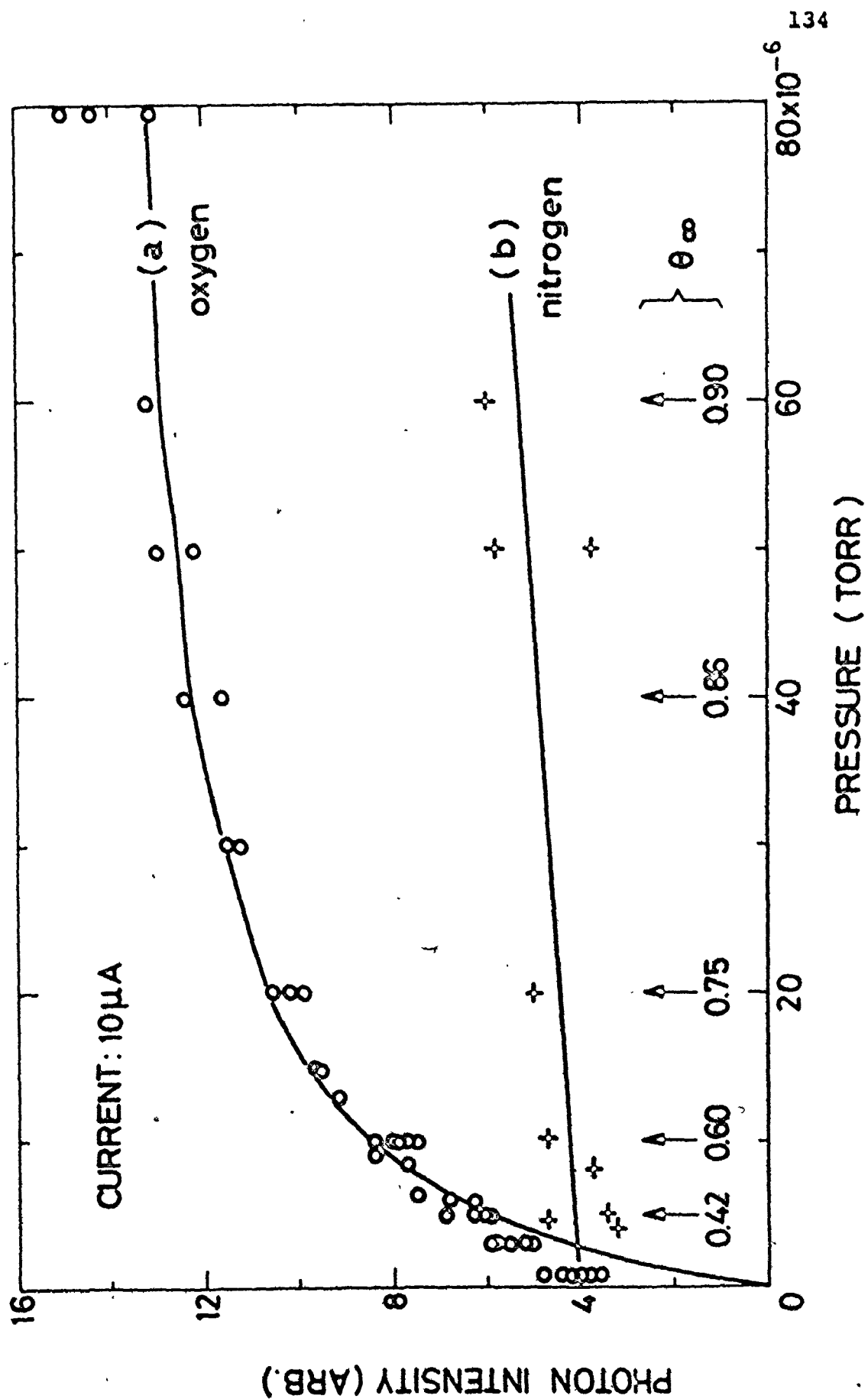
Fig. 8-3 XPS spectra of MO 3d<sub>3/2,5/2</sub> levels of MoO<sub>3</sub> exposed to Ar<sup>+</sup> ions and O<sub>2</sub>. Taken from reference 30

the ion energy is less than about 1 keV (i.e. less than the threshold energy for reduction with oxygen ion bombardment as outlined in this thesis, section 5.2).

Preferential sputtering effects are inherent in the technique itself when secondary ion mass spectrometry (SIMS) is used for surface characterization. The sample is bombarded with energetic heavy ions and the sputtered secondary ions are mass analyzed to give an indication of the surface composition. SIMS appears to be a straightforward technique for in-depth concentration profiling, since both the depth probing and signal generation are performed by just one process, namely the bombardment by primary ions. However when multi component samples are sputtered, the components with higher sputtering yields are sputtered preferentially leading to an enrichment on the surface of the components with the lower sputtering yields.

The bombardment of solids with energetic ions also leads to the emission of photons in the visible range. The intensity of the observed spectral lines depends strongly on the surface conditions. The photon yields are established to be influenced in the case of metal targets by the target gaining oxygen and in the case of oxide targets by the target losing oxygen (133). An example concerning the dependence of the photon yield from Al on the oxygen pressure is shown in figure 8-4.

Fig. 8-4 Photon yield at 308.2-309.3 nm  
from Al due to the impact of 10 keV  
Ne as a function of rest gas pressure  
for a fixed current of 10  $\mu\text{A}$  (80  
 $\mu\text{A}/\text{cm}^2$ ). Curve (a): oxygen.  
Curve (b): nitrogen. The steady-  
state oxygen coverage,  $\theta_{\infty}$ , is indi-  
cated in the lower part of the figure.  
Taken from reference 134.



## 8.7 PREFERENTIAL SPUTTERING OF CERMET FILMS

Preferential sputtering can also be beneficial as indicated by studies on the ion bombardment of MgO/Au cermet films (134). Under Ar ion bombardment the surface Au content was found to decrease with time by up to a factor of 20. The cermet films composed of a high yield insulator and a metal (e.g. MgO/Au) offer the possibility of obtaining excellent secondary electron yields. The presence of metal microcrystallites permits the removal of surface charge by tunneling and other modes of conduction to the metallic substrate, so that the films do not suffer from the severe surface charging problems inherent with thick insulating films. For low energy incident electrons the secondary electron emission yield is primarily determined by the MgO rich surface layer. Therefore, preferential sputtering gives rise to larger yields than would be obtained if the surface had the bulk composition, but without causing a significant increase in surface charging.

## 8.8 ION BOMBARDMENT EFFECTS WITH Ta<sub>2</sub>O<sub>5</sub>

### 8.8.1 Introduction

Since niobium and tantalum belong to Group V in the Periodic chart of the elements and Nb<sub>2</sub>O<sub>5</sub> and Ta<sub>2</sub>O<sub>5</sub> exhibit similar properties it is interesting to study the general trends of the ion impact effects with Ta<sub>2</sub>O<sub>5</sub>. It was anticipated that a major effect might lie in the instability of lower valence states of Ta.

Sintered pellets of  $\text{Ta}_2\text{O}_5$  were prepared similarly to the  $\text{Nb}_2\text{O}_5$  pellets described in chapter 3, section 3.1.2. Anodic oxide films of  $\text{Ta}_2\text{O}_5$  were formed in an aqueous solution of 0.2% KF at a preset current density of  $4 \text{ mA/cm}^2$  and a preset potential of 40 V. The oxide thickness (X) formed at a voltage V is given by (135):

$$X = 1.32 V \quad \mu\text{g/cm}^2.$$

Typical film thickness was about 66 nm, assuming the density of  $\text{Ta}_2\text{O}_5$  to be  $8.04 \text{ g/cm}^3$  (57). The experimental procedures and techniques are the same as outlined in chapter 3.

#### 8.8.2 Experimental Results - Conductivity Changes

$\text{Ta}_2\text{O}_5$  pellets were bombarded with 35 keV  $\text{O}_2^+$  and  $\text{Kr}^+$  ions to various doses ranging from  $10^{15}$  to  $10^{17}$  ions/ $\text{cm}^2$ . The sheet conductivities were measured in each case with a four point probe and results are shown in figure 8-5. It is evident that ion bombardment of  $\text{Ta}_2\text{O}_5$  results in a very small increase in sheet conductivity whereas similar bombardments with  $\text{Nb}_2\text{O}_5$  led to an extremely large increase in sheet conductivity.

#### 8.8.3 Experimental Results - Structural Changes

Bombarded pellets of  $\text{Ta}_2\text{O}_5$  were examined in the reflection mode of the electron microscope but were found to exhibit charging effects. An external bias voltage of 1 kV was insufficient to suppress the charging effects. These results provide indirect evidence of the insulating nature of the bombarded  $\text{Ta}_2\text{O}_5$  pellets.



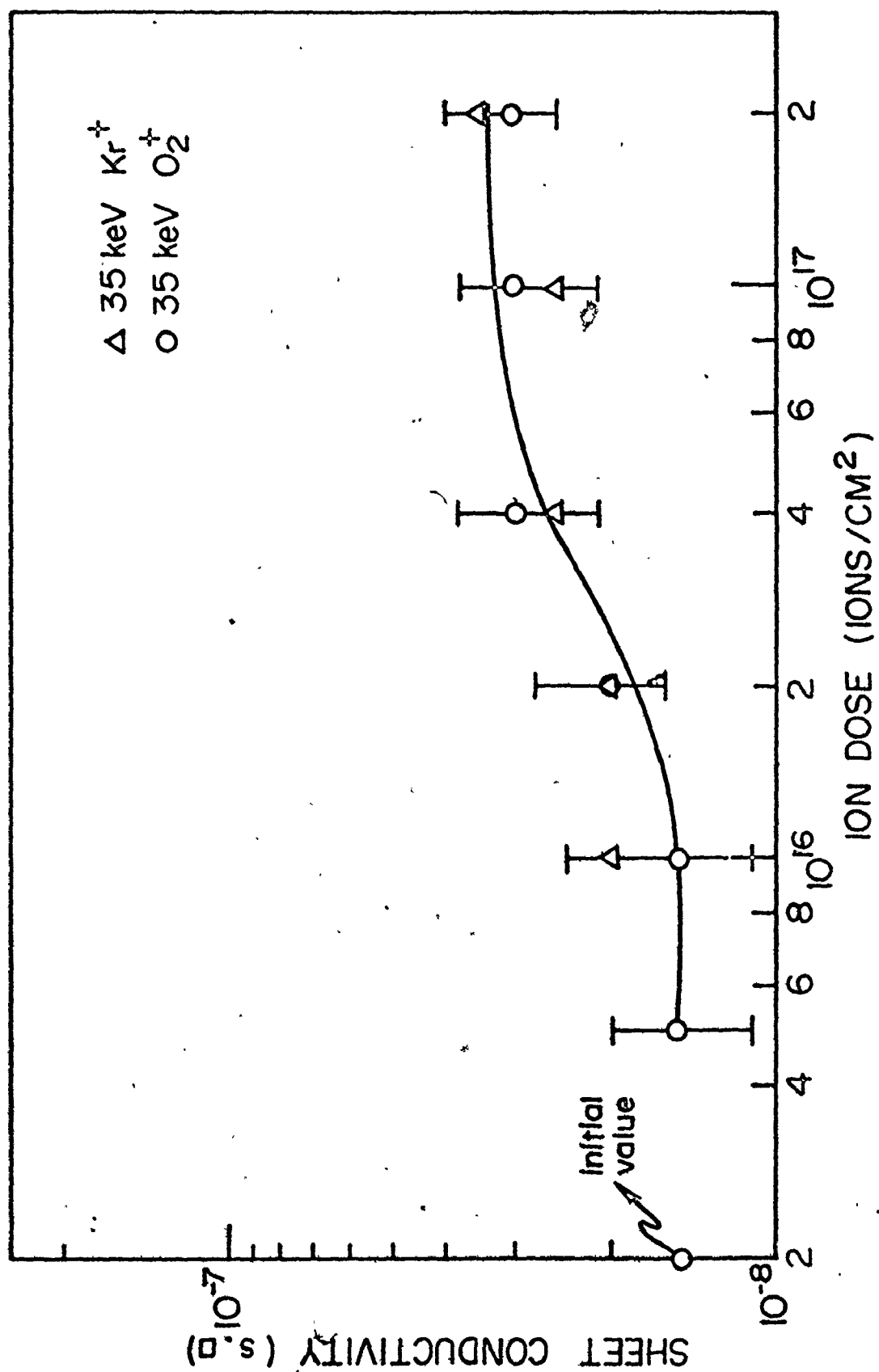


Fig. 8-5 Effect of ion dose on the sheet conductivity of  $\text{Ta}_2\text{O}_5$  pellets bombarded with 35 keV  $\text{Kr}^+$  ( $\Delta$ ) and  $\text{O}_2^+$  ( $\circ$ ) ions

Thin films of  $Ta_2O_5$  were bombarded with 35 keV  $O_2^+$  ions to various doses ranging from  $10^{15}$  to  $10^{17}$  ions/cm<sup>2</sup> and examined in the transmission mode of the electron microscope. The basic result, as shown in Figure 8-6, is that the diffraction pattern of the as prepared anodic  $Ta_2O_5$  film still persists at high dose bombardment. The effects of ion bombardment of  $Ta_2O_5$ , as outlined here are significantly different from those of  $Nb_2O_5$  wherein high dose ion bombardment results in an altered surface identified as NbO.

#### 8.8.4 Conclusions

In spite of  $Nb_2O_5$  and  $Ta_2O_5$  exhibiting similar properties, their response to ion impact is significantly different. The lack of formation of lower oxides of Ta due to ion bombardment of  $Ta_2O_5$  can be compared with attempts to prepare lower oxides of Ta by chemical reduction. Although a number of tantalum oxides are described in the early literature (136), more recent investigators (137 to 144) have failed to confirm their existence. The literature on suboxides of tantalum was critically reviewed by Niebuhr (141). As stated by Niebuhr, on evaporating  $Ta_2O_5$  or degassing tantalum metal, TaO and  $TaO_2$  molecules are found in the vapour. It has been pointed out by Kofstad (144) that  $Ta_2O_5$  is the only stable solid oxide of tantalum. The oxides TaO and  $TaO_2$  are not stable in the solid state but only as gases as shown by Inghram et al. (137) in a mass spectrometric study of mixtures of Ta and  $Ta_2O_5$  at temperatures

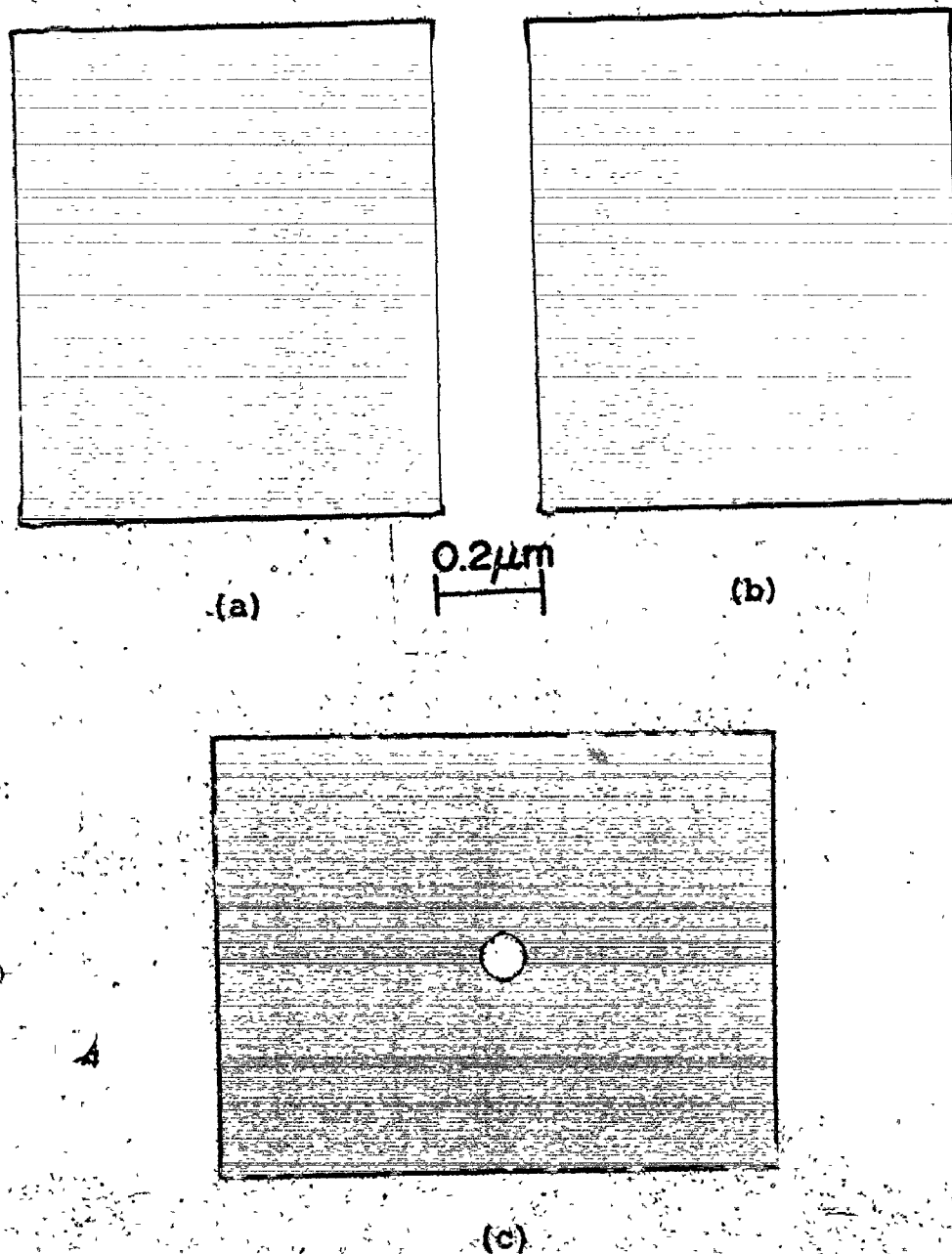


Figure 3-5. Transmission electron microscopy of anodic  $Ta_2O_5$  films: (a) bright field view of prepared films, (b) bright field view of films which have been bombarded with 35 keV  $O_2^+$  to a dose of  $1 \times 10^{17}$  ions/cm<sup>2</sup>, (c) diffraction pattern corresponding to (a) and (b).

ranging from 1750°C to 2050°C. Kudrak and Sienko (142) have reported the preparation of single crystals of  $\text{Ta}_2\text{O}_{4.73}$  by vacuum fusion of  $\text{Ta}_2\text{O}_5$  in Ta at about 1900°C. Electrical conductivity studies disclosed metallic behaviour with a conductivity of  $2.5 \times 10^3$  S/m.

## CHAPTER 9

### SUMMARY

1. The structural changes induced in  $\text{Nb}_2\text{O}_5$  by ion bombardment have been studied using electron microscopy. It has been shown that 35 keV  $\text{O}_2^+$  bombardment leads initially to an altered layer which is amorphous at low doses (up to  $5 \times 10^{15}$  ions/cm<sup>2</sup>) and finally has the stoichiometry NbO at high doses (greater than  $5 \times 10^{16}$  ions/cm<sup>2</sup>). This has been confirmed in thin films using the transmission mode and in sintered pellets using the reflection mode.
2. The present study using thin films of  $\text{Nb}_2\text{O}_5$  indicates for the first time that the oxygen loss due to ion bombardment occurs by virtue of the formation of crystalline regions of NbO having diameters of 5 to 15 nm. The altered regions thus have dimensions similar to the amorphous regions found with Si and Ge and the crystalline regions of  $\text{ZrO}_2$ .
3. These results with  $\text{Nb}_2\text{O}_5$  are evidently not due to beam heating of thin films as the basic feature (the formation of NbO) occurs also with pellets with effectively semi-infinite thickness.
4. The impact of both  $\text{Kr}^+$  and  $\text{O}_2^+$  ions at 35 keV and  $2 \times 10^{17}$  ions/cm<sup>2</sup> leads to an increase in the sheet conductivity by a factor of  $5 \times 10^3$ .
5. Bombarded pellets showed no change in conductivity when stored

in air at room temperature. On heating in air the conductivity is stable up to 400°C but with further heating decreases to the initial unbombarded value. On heating bombarded pellets in vacuum ( $\sim 1.3 \times 10^{-4}$  Pa) the conductivity increases by a factor of 600.

6. The conductivity is independent of current for 2 to 10  $\mu\text{A}/\text{cm}^2$  but increases by a factor of 20 for higher currents.
7. The variation of conductivity with energy suggests that a saturation effect will occur with increasing energy. The saturation could not, however, be observed explicitly.
8. Oxygen bombardment shows well defined threshold effects at about 5 keV whereas Kr bombardment reveals sheet conductivity changes at energies as low as 2 keV.
9. A technique based on changes in the chemical reactivity of the altered layer as compared to the substrate, is used to estimate the thickness of the altered layer on bombarded  $\text{Nb}_2\text{O}_5$ . A suitable solvent, which dissolves the altered layer at a much faster rate than the substrate, was found to have a composition of 15  $\text{cm}^3$  hydrofluoric acid (48%), 10  $\text{cm}^3$  nitric acid (70%), and 50  $\text{cm}^3$  water. The thickness of the altered layer on  $\text{Nb}_2\text{O}_5$  was concluded to vary from 18 nm at very low doses ( $5 \times 10^3$  ions/ $\text{cm}^2$ ) to 23 nm at high doses ( $1 \times 10^{17}$  ions/ $\text{cm}^2$ ).
10. The bulk conductivity of an altered layer formed at  $1 \times 10^{17}$  ions/ $\text{cm}^2$  is about  $4.3 \times 10^3$  S/m, an increase by a factor of  $2 \times 10^8$ . Note, by contrast, that the sheet conductivity increases by a smaller amount (#4).

11. Oxygen loss from bombarded  $\text{Nb}_2\text{O}_5$  was considered to have three alternative origins based on a vaporization model, an internal displacement model, and a preferential sputtering model. The experimental results serve to show that the oxygen loss is due to preferential sputtering.
12. A modified sputtering model explains the energy threshold effect observed when an oxygen beam is used.
13. The thickness of the altered layer can be deduced from a diffusion model which combines preferential sputtering of oxygen at the surface and diffusion of the relevant point defects. The thickness (34 nm) deduced from such a model is comparable with that determined from dissolution experiments (23 nm).
14. Several applications of the techniques and results presented here have been considered. They include, among others, dating of minerals, limitations of surface analytical techniques, and preliminary results for  $\text{Ta}_2\text{O}_5$ .

## APPENDIX I

RANGE PARAMETERS FOR 35 keV  $^{85}\text{Kr}$  IONS INCIDENT ON NbO

## I.1 MEAN RANGE

The method to be used for deducing the mean range involves the basic assumption that the stopping cross sections due to different atoms in a compound are all proportional to the same power of the incident ion energy.

Consider a compound  $C = A_x B_y$  and let  $M_A$ ,  $M_B$  and  $M_C$  be the masses of the constituent atoms A, B and of the compound C, respectively, and  $R_A$ ,  $R_B$  and  $R_C$  be the corresponding ranges. A simple formula has been used by Domeij et al. (145) to deduce range parameters in  $\text{WO}_3$  and  $\text{Al}_2\text{O}_3$  and the results were found to be in agreement with experimental measurements. The formula can be briefly derived as follows.

The total range R is given by

$$R = \int_E^0 \frac{dE}{(dE/dR)} \quad (\text{I-1})$$

Since the stopping cross sections are assumed to be proportional to the same power of the incident ion energy we have

$$\left(\frac{dE}{dR}\right)_A = K_A E^n \quad (\text{I-2})$$

$$\left(\frac{dE}{dR}\right)_B = K_B E^n \quad (\text{I-3})$$

Taking the energy to be shared stoichiometrically we have

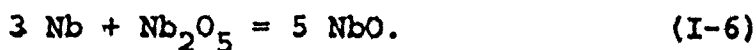


$$M_C \left( \frac{dE}{dR} \right)_C = x M_A \left( \frac{dE}{dR} \right)_A + y M_B \left( \frac{dE}{dR} \right)_B \quad (I-4)$$

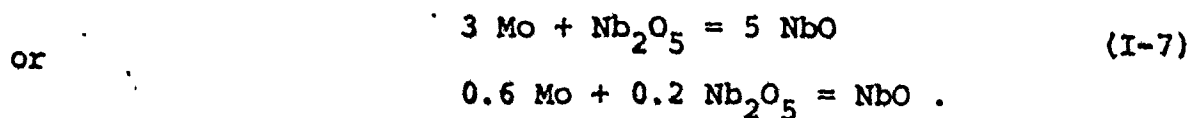
where  $(dE/dR)_C$  etc. are in units of  $\text{keV cm}^2/\mu\text{g}$ . The range  $R_C$  is then given by

$$\begin{aligned} R_C &= \int_E^0 \frac{dE}{(dE/dR)_C} \\ &= \int_E^0 \frac{dE}{\left( \frac{x M_A}{M_C} K_A E^n + \frac{y M_B}{M_C} K_B E^n \right)} \\ &= \left( \frac{1}{\frac{x M_A}{M_C R_A} + \frac{y M_B}{M_C R_B}} \right) \\ &= \frac{M_C R_A R_B}{(x M_A R_B + y M_B R_A)} \quad (I-5) \end{aligned}$$

The method outlined above can be applied to the compound NbO when it is taken to be formed from Nb and  $\text{Nb}_2\text{O}_5$ , namely



Since the range parameters for 35 keV Kr ions incident on Mo and  $\text{Nb}_2\text{O}_5$  are accurately known (99) and since further the atomic weights of Mo and Nb are nearly the same, an alternative to equation (I-6) is



The relevant range parameters for 35 keV Kr ions to be used in conjunction with equations (I-5) and (I-7) are as follows:

$$R_{\text{Mo}} = 9.25 \mu\text{g/cm}^2$$

$$R_{\text{Nb}_2\text{O}_5} = 7.25 \text{ } \mu\text{g}/\text{cm}^2 .$$

The range of 35 keV Kr ions incident on NbO is then given by

$$\begin{aligned} R_{\text{NbO}} &= 7.96 \text{ } \mu\text{g}/\text{cm}^2 \\ &= 11 \text{ nm} . \end{aligned}$$

## I.2 STANDARD DEVIATION IN RANGE

The average square fluctuation in the total range  $(\Delta R)^2$  based on LSS theory is given by

$$(\Delta R)^2 = \frac{1}{N^2} \int_0^E \frac{\Omega^2(E) dE}{S_n^3(E)} \quad (\text{I-8})$$

where

$$\begin{aligned} \Omega^2(E) &= \int_0^{T_m} T^2 d\sigma \\ S_n(E) &= \int_0^{T_m} T d\sigma . \end{aligned}$$

$T_m$  is the maximum energy transfer occurring in a head-on collision and is given by

$$T_m = \gamma E \quad (\text{I-9})$$

where

$$\gamma = \frac{4M_1M_2}{(M_1+M_2)^2} .$$

Also,  $d\sigma$  is the power law scattering cross section given by

$$d\sigma = CE^{-m} T^{-1-m} dT .$$

In order to facilitate the calculation of  $\Delta R$ , it can be expressed in terms of the total range  $R$ . The range  $R$  as given by equation (I-1) can be written as

$$R = \frac{1}{N} \int_0^E \frac{dE}{S_n(E)} \quad (I-10)$$

$$= \frac{1}{N} \int_0^E \frac{dE}{\int_0^E T_m T d\sigma}$$

It can be shown that

$$R^2 = \frac{1}{N^2 C^2} \frac{(1-m)^2}{4m^2} \frac{E^{4m}}{\gamma^{2-2m}} \quad (I-11)$$

From equations (I-8) and (I-9) it follows that

$$(\Delta R)^2 = \frac{(1-m)^3}{4m(2-m)} \frac{E^{4m}}{\gamma^{2m-1}} \quad (I-12)$$

Hence

$$\frac{(\Delta R)^2}{(R)^2} = \frac{\gamma(1-m)m}{(2-m)} \quad (I-13)$$

By using the parameters  $\gamma = 0.95$  and  $m = \frac{1}{2}$ , appropriate to 35 keV Kr ions incident on NbO, the result is

$$\frac{(\Delta R)^2}{(R)^2} = 0.16$$

or

$$\Delta R = 0.40 R \quad (I-14)$$

Thus, the standard deviation in range  $\Delta R$  for 35 keV Kr ions incident on NbO will be taken as 4.4 nm.

## APPENDIX II

RANGE PARAMETERS FOR keV  $O_2^+$  IONS INCIDENT ON  $Nb_2O_5$ 

A table of the range distribution parameters for keV  $O_2^+$  ions incident on  $Nb_2O_5$  is presented below. The results were supplied by Dr. K. B. Winterbon (AECL, Chalk River, Canada). The table as given correctly takes into account the result that if the  $O_2^+$  ion has an energy  $E_1$  then the particle undergoing the stopping process is  $O^+$  with an energy  $E_1/2$ .

Table II-1

Range parameters for  $O_2^+$  ions incident on  $Nb_2O_5$

Energy of $O_2^+$ keV	$\langle x \rangle$ $\mu g/cm^2$	$\langle x \rangle$ nm	$\frac{\langle \Delta x^2 \rangle}{\langle x \rangle^2}$	$\Delta x$ nm
5	2.227	4.7	0.5194	3.4
10	3.982	8.4	0.4898	5.9
20	7.518	15.8	0.4488	10.7
35	13.100	27.6	0.4061	17.4
40	15.040	31.8	0.3945	20.0

## REFERENCES

1. D. P. Smith, Surface Sci. 25, 171 (1971).
2. H. H. Brongersma, J. Vac. Sci. Tech. 11, 231 (1974).
3. C. Snoek, W. F. Van der Weg and P. K. Rol, Physica 30, 341 (1964).
4. I. Terzic and B. Perovic, Surface Sci. 21, 86 (1970).
5. C. Kerkdijk and E. W. Thomas, Physica 63, 577 (1973).
6. F. W. Saris, Proc. Int. Conf. "Physics of Electron and Atomic Collisions". Ed. T. R. Govers and F. J. de Heer (North-Holland Co.) P. 181 (1972).
7. R. H. Silsbee, J. Appl. Phys. 28, 1246 (1957).
8. L. I. Maissel and R. Glang "Handbook of Thin Film Technology" (McGraw-Hill Co., New York 1970).
9. K. L. Chopra, "Thin Film Phenomena" (McGraw-Hill Co. New York, 1969).
10. M. Kaminsky, "Atomic and Ionic Impact Phenomena on Metal Surfaces", (Academic Press, New York 1965).
11. J. J. Trillat, J. de Chimie Physique 53, 570 (1956).
12. R.L. Cunningham, P. Haymann, C. LeComte, W. J. Moore and J. J. Trillat, J. Appl. Phys. 31, 839 (1960).
13. A.D.G. Stewart and M.W. Thompson, J. Mater. Sci. 4, 56 (1969).
14. I. H. Wilson and M. W. Kidd, *ibid.* 6, 1372 (1971).
15. P. Sigmund, *ibid.* 8, 1545 (1973).
16. K. B. Winterbon, P. Sigmund and J. B. Sanders, Mat. Fys. Medd. Dan. Vid. Selsk. 37, no. 14 (1970).
17. J. R. Parsons, Phil. Mag. 12, 1159 (1965).

18. D. J. Mazey, R. S. Nelson and R. S. Barnes, *ibid.* 17, 1145 (1968).
19. D.J. Mazey and R. S. Nelson, *Rad. Effects.* 1, 229 (1969).
20. E. Gillam, *J. Phys. Chem. Solids* 11, 55 (1959).
21. W. T. Ogar, N. T. Olson and H. P. Smith, *J. Appl. Phys.* 40, 4997 (1969).
22. G. S. Anderson, *J. Appl. Phys.* 40, 2884 (1969).
23. S. D. Dahlgren and E. D. McClanahan, *ibid.* 43, 1514 (1972).
24. R. Kelly, N. Q. Lam, D. K. Murti, H. M. Naguib and T. E. Parker, "Physics of Ionized Gases", Ed. M. V. Kurepa, p. 349 (1972).
25. J. J. Trillat, N. Terao and L. Tertian, *Compt. Rend. Acad. Sci. Paris*, 242, 1294 (1956).
26. T. Suzuki, *Z. Naturforsch.* 12a, 497 (1957).
27. E. Kuczma and R. Kelly, to be published (1975).
28. H. M. Naguib and R. Kelly, *J. Phys. Chem. Solids* 33, 1751 (1972).
29. A. Preisinger, T. Tortschanoff, F. Viehbock and W. Weismann, *Japan J. Appl. Phys. Suppl.* 2, Part 2, 791 (1974).
30. K. S. Kim, W. E. Baitinger, J. E. Amy and N. Winograd, *J. Electron. Spectrosc.* 5, 351 (1974).
31. L. T. Chadderton and I. M. Torrens, *Proc. Roy. Soc. A* 294, 80 (1966).
31. (a) L. T. Chadderton, Private Communication (1974).
32. T. E. Parker and R. Kelly, "Ion Implanatation in Semiconductors and Other Materials", Ed. B. L. Crowder (Plenum Press,

50. P. K. Rol, J. M. Fluit and J. Kistemaker, *Physica* 26, 1009 (1960).
51. P. Sigmund, *Phys. Rev.* 184, 383 (1969).
52. P. Sigmund, *Appl. Phys. Lett.* 14, 114 (1969).
53. M. T. Robinson, *Phil. Mag.* 12, 741 (1965).
54. N. Andersen and P. Sigmund, *Mat. Fys. Medd. Dan. Vid. Selsk.* 39, No. 3 (1974).
55. N. Andersen and P. Sigmund, Private Communication (1974).
56. R. E. Pawel and J. J. Campbell, *J. Electrochem. Soc.* 111, 1230 (1964).
57. A. J. Schrijner and A. Middelhoek, *ibid.* 111, 1167 (1964).
58. L. B. Valdes, *Proc. I.R.E.* 42, 420 (1954).
59. F. M. Smits, *Bell System Tech. Jour.* 37, 711 (1958).
60. E. H. Greener and W. M. Hirthe, *J. Electrochem. Soc.* 109, 600 (1962).
61. R. F. Janninck and D. H. Whitmore, *J. Chem. Phys.* 37, 2750 (1962).
62. P. Kofstad, *J. Phys. Chem. Solids* 23, 1571 (1962).
63. I. Reid, M.Sc. Thesis, McMaster University (1971).
64. A. Uhlar, *Bell System Tech. Jour.* 34, 105 (1955).
65. P. B. Hirsch, A. Howie, R. B. Nicholson, D. W. Pashley and M. J. Whelan, "Electron Microscopy of Thin Crystals" (Butterworths, London, 1965).
66. R. D. Heidenreich, "Fundamentals of Transmission Electron Microscopy" (John Wiley & Sons, New York, 1964).
67. L. E. Murr, "Electron optical applications in Materials

68. G. Thomas, "Transmission Electron Microscopy of Metals"  
(John Wiley & Sons, New York, 1962).
69. E. Bauer, "Techniques of metals research", Ed. R. F. Bunshah,  
Vol. II, Part 2, p. 501 (John Wiley & Sons, New York, 1969).
70. A. W. Agar, Brit. J. Appl. Phys. 11, 185 (1960).
71. W. Cochrane, Proc. Roy. Soc. 48, 723 (1936).
72. R. Phillips, Brit. J. Appl. Phys. 11, 504 (1960).
73. R. S. Nelson and D. J. Mazey, Can. J. Phys. 46, 689 (1968).
74. B. G. Bagley, H. S. Chen and D. Turnbull, Mat. Res. Bull.  
3, 159 (1968).
75. D.E. Polk, J. Non-cryst. Sol. 5, 365 (1971).
76. P. K. Leung and J. G. Wright, Phil. Mag. 30, 995 (1974).
77. J. F. Graczyk and S. C. Moss, Rev. Sci. Instr. 40, 424 (1969).
78. S. Moss and J. F. Graczyk, Phys. Rev. Lett. 23, 1167 (1969).
79. P. Chaudhari, J. F. Graczyk and S. R. Herd, Phys. Stat.  
Solidi (b) 51, 801 (1972).
80. D. A. Vermilyea, Acta Met. 1, 282 (1953).
81. L. Young, "Anodic Oxide Films" (Academic Press, New York, 1961).
82. J. Harvey and H. Wilman, Acta Cryst. 14, 1278 (1961).
83. L. D. Calvert and P.H.G. Draper, Can. J. Chem. 40, 1943  
(1962).
84. J. Spyridelis, P. Delavignette and S. Amelinckx, Mat. Res.  
Bull. 2, 113 (1967).
85. D. G. Brandon, J. Zahavi, A. Aladjem and J. Yahalom, J. Vac.  
Sci. Tech. 6, 783 (1969).



86. D. M. Lakhiani and L. L. Shreir, *Nature* 188, 49 (1960).
87. N. Q. Lam and R. Kelly, *Can. J. Phys.* 48, 137 (1970).
88. H. M. Naguib and R. Kelly, *J. Nucl. Mater.* 35, 293 (1970).
89. E.H. Greener, D.H. Whitmore and M. E. Fine, *J. Chem. Phys.* 34, 1017 (1960).
90. W. K. Chen and R. A. Swalin, *J. Phys. Chem. Solids* 27, 57 (1966).
91. T. E. Parker and R. Kelly, *ibid.* 36, 377 (1975).
92. J.B. Griffiths, *Nature* 188, 43 (1960).
93. W. Meissner, H. Franz and H. Westerhoff, *Ann. Phys.* 17, 593 (1933).
94. J. A. Roberson and R. A. Rapp, *J. Phys. Chem. Solids* 30, 1119 (1969).
95. C. N. R. Rao and G. V. Subba Rao, *Phys. Stat. Solidi (a)*, 1, 622 (1970).
96. C. Jech, *ibid.* 21, 481 (1967).
97. N. Q. Lam and R. Kelly, *Can. J. Phys.* 50, 1887 (1972).
98. W. A. Pliskin and R. P. Gnall, *J. Electrochem. Soc.* 111, 872 (1964).
99. H. Schjøtt, Personal Communication to Dr. R. Kelly.
100. Handbook of Chemistry and Physics, 52nd Edition, E72 (The Chemical Rubber Co., Cleveland, Ohio, 1971).
101. R. S. Nelson, *Phil. Mag.* 11, 291 (1965).
102. O. Kubaschewski, E. L. Evans and C. B. Alcock, "Metallurgical Thermochemistry", 4th Edition (Pergamon, Oxford, 1967).

103. G. W. Arnold and W. D. Compton, Phys. Rev. Lett. 4, 66 (1960).
104. S. Lungu, Phys. Stat. Solidi 23, 147 (1967).
105. D. B. Carroll and H. K. Birnbaum, J. Appl. Phys. 36, 2658 (1965).
106. D. P. Jackson, Rad. Effects 18, 185 (1973).
107. L. Fiermans and J. Vennik, Surface Sci. 9, 187 (1968).
108. J. Van Landuyt and S. Amelinckx, J. Sol. State Chem. 6, 222 (1973).
109. L. Fiermans and J. Vennik, Surface Sci. 24, 541 (1971).
110. M. Meyer, P. Haymann and J. J. Trillat, Compt. Rend. Acad. Sci. Paris, 261, 4353 (1965).
111. G. Carter, J. S. Colligon and H. J. Leck, Proc. Phys. Soc. 79, 299 (1962).
112. J. P. Biersack, Rad. Effects. 19, 249 (1973).
113. L. I. Yin, S. Ghose and I. Adler, Appl. Spectros. 26, 355 (1972).
114. K. S. Kim and N. Winograd, Surface Sci. 43, 625 (1974).
115. M. N. Colpaert, P. Clauws, L. Fiermans and J. Vennik, *ibid.* 36, 513 (1973).
116. H. S. Carslaw and J. C. Jaeger, "Conduction of heat in solids", (Oxford University Press, 1959).
117. D. G. Hurst, Chalk River (Canada) Report CRRP-1124 (1962).
118. H. Gaus, Z. Naturforsch. 20a, 1298 (1965).
119. R. Kelly and L. Q. Nghi, Rad. Effects 6, 247 (1970).
120. R. Kelly and H. J. Matzke, J. Nucl. Mater. 20, 171 (1966).

122. D. Adler, Rad. Effects 4, 123 (1970).
123. E.N. Fuls, D.H. Hensler and A. R. Ross, Appl. Phys. Lett. 10, 199 (1967).
124. C.C.Y. Kwan, C.H. Griffiths and H.K. Eastwood, *ibid*, 20, 93 (1972).
125. F. K. McTaggart, Nature 191, 1192 (1961).
126. F. K. McTaggart, *ibid*. 199, 339 (1963).
127. M. R. Wertheimer, Ecole Polytechnique (Private Communication).
128. R. Burns, M.I.T. (Private Communication).
129. J. R. Smyth, Earth and Planet. Sci. Lett. 24, 262 (1974).
130. C. M. Sung, R. M. Abu-Eid and R. Burns, Geochimica et Cosmochimica Acta, Suppl. 5, 1, 717 (1974).
131. G. K. Wehner, C. E. Ken Knight and D. Rosenberg, Planet. Space Sci. 11, 1257 (1963).
132. H. M. Naguib, D. K. Murti and R. Kelly, J. Mater. Sci. (In Press).
133. R. Kelly and C. B. Kerkdijk, Surface Sci. 46, 537 (1974).
134. V. E. Henrich and J.C.C. Fan, *ibid*. 42, 139 (1974).
135. R. E. Pawel, Rev. Sci. Instr. 35, 1066 (1964).
136. N. Schonberg, Acta. Chem. Scand. 8, 240 (1954).
137. M.G. Inghram, W. A. Chupka and J. Berkowitz, J. Chem. Phys. 27, 569 (1957).
138. R.J. Wasilewski, Trans. Met. Soc. A.I.M.E. 221, 647 (1961).
139. N. Norman, P. Kofstad and O. J. Krudtaa, J. Less-Common Metals 4, 124 (1962).

140. G. Brauer, H. Muller and G. Kuhner, *ibid.* 4, 533 (1962).
141. J. Niebuhr, *ibid.* 10, 312 (1966).
142. D. R. Kudrak and M. J. Sienko, *Inorg. Chem.* 6, 880 (1967).
143. N. Terao, Japan. *J. Appl. Phys.* 6, 21 (1967).
144. P. Kofstad, "Non stoichiometry, diffusion, and electrical conductivity in binary metal oxides". (John Wiley & Sons, New York, 1972).
145. B. Domeij, F. Brown, J. A. Davies and M. McCargo, *Can. J. Phys.* 42, 1624 (1964).